



저작자표시-비영리-변경금지 2.0 대한민국

이용자는 아래의 조건을 따르는 경우에 한하여 자유롭게

- 이 저작물을 복제, 배포, 전송, 전시, 공연 및 방송할 수 있습니다.

다음과 같은 조건을 따라야 합니다:



저작자표시. 귀하는 원저작자를 표시하여야 합니다.



비영리. 귀하는 이 저작물을 영리 목적으로 이용할 수 없습니다.



변경금지. 귀하는 이 저작물을 개작, 변형 또는 가공할 수 없습니다.

- 귀하는, 이 저작물의 재이용이나 배포의 경우, 이 저작물에 적용된 이용허락조건을 명확하게 나타내어야 합니다.
- 저작권자로부터 별도의 허가를 받으면 이러한 조건들은 적용되지 않습니다.

저작권법에 따른 이용자의 권리는 위의 내용에 의하여 영향을 받지 않습니다.

이것은 [이용허락규약\(Legal Code\)](#)을 이해하기 쉽게 요약한 것입니다.

[Disclaimer](#)

이학박사 학위논문

# Cosmological Applications of Filamentary Structures in the Universe

우주에 있는 필라멘트 구조물의 우주론적 응용

2018년 8월

서울대학교 대학원  
물리·천문학부 천문학전공  
심준섭



# ABSTRACT

The formation and evolution of filamentary structures involve the actions of the dark sector and gravitational law. At the same time, a filament is an important environment through which gas and matter accrete and subhalos infall onto its member galaxies (halos). In this thesis, we present studies on filamentary structures in two contexts, one for filament as a probe to constrain cosmological models and the other for studying the effects of filaments on its halos and galaxies. In Part 1, we presented how the shapes of filaments change depending on cosmological models. We identified large-scale filaments from dark matter halos of cosmological simulations of various cosmological models including  $\Lambda$ CDM, a branch of dynamic dark energy, and a branch of modified gravity. It is found that filaments in the  $\Lambda$ CDM universe are straighter than those in the other models. We also found that the discriminations of the alternative models from  $\Lambda$ CDM and between themselves are possible with the straightness evolution of filaments. By finding the dependence of filament straightness on underlying cosmology, we suggest the straightness of filaments as a complimentary cosmological test. In Part 2, we studied the roles of filaments in the galaxy (halo) formation and evolution. First, we examined the dependence of substructure abundance of clusters on filament straightness. Clusters in straighter filaments are found to have fewer substructures even when the contribution of the mass and formation time of halo, and the number of clusters in filament are minimized. On the other hand, we also studied the correlation between void galaxy luminosity and straightness of void filament. It was found that void galaxies are brighter in straighter void filaments. Based on these findings, we conclude that filaments influence on their galaxies (halos) by controlling subhalo infall and mass accretion onto galaxies (halos). Physical interpretations of our results, as well as their cosmological implications are presented.

**Keywords:** cosmology: theory – large-scale structure of Universe

***Student Number:*** 2011-23285



# Contents

**Abstract**

**List of Figures** **v**

**List of Tables** **ix**

**1 Overview** **1**

1.1 Cosmic Web Phenomenon in the Universe . . . . . 1

1.1.1 Formation of Cosmic Web . . . . . 3

1.1.2 Components of Cosmic Web . . . . . 4

1.2 Identifying Filamentary Structures . . . . . 8

1.2.1 Filament Finding Algorithms . . . . . 9

1.2.2 Minimal Spanning Tree Method . . . . . 10

1.3 Filaments and Cosmology . . . . . 11

1.4 Filaments and Galaxy (Halo) Formation and Evolution . . . . . 15

1.4.1 Filaments and Substructure Abundance of Cluster Halos . . . . . 15

1.4.2 Filaments and Luminosity of Void Galaxies . . . . . 17

1.5 In this Thesis . . . . . 19

**2 Dark Sector Coupling Bends the Superclusters** **29**

2.1 Introduction . . . . . 29

2.2 Numerical Data and Analysis . . . . . 32

2.2.1 A Brief Summary of the CODECS . . . . . 32

2.2.2	Identifying the Supercluster Spines . . . . .	33
2.3	Supercluster Straightness as a Probe of cDE . . . . .	35
2.4	Summary and Discussion . . . . .	39
<b>3</b>	<b>Massive Gravity Wrapped in the Cosmic Web</b>	<b>57</b>
3.1	Introduction . . . . .	57
3.2	Data and Algorithm . . . . .	59
3.3	Effect of f(R) Gravity on the Supercluster Straightness . . . . .	61
3.4	Discussion and Conclusion . . . . .	63
<b>4</b>	<b>Breaking the Cosmic Degeneracy with the Cosmic Web</b>	<b>79</b>
4.1	Introduction . . . . .	79
4.2	Constructing the Supercluster Samples . . . . .	82
4.3	Simultaneous Effect of MG and $\nu$ on the Supercluster Straightness . . . . .	83
4.4	Discussion and Conclusion . . . . .	85
<b>5</b>	<b>Dependence of the Substructure Abundance on the Orientation Coherence of the Halo Tidal Field</b>	<b>97</b>
5.1	Introduction . . . . .	97
5.2	Identifying the Filaments of Cluster Halos . . . . .	100
5.3	Substructure Abundance of the Cluster Halos in the Filaments . . . . .	103
5.4	Summary and Discussion . . . . .	106
<b>6</b>	<b>An Observational Detection of the Bridge Effect of Void Filaments</b>	<b>133</b>
6.1	Introduction . . . . .	133
6.2	Identifying the Mini-Filaments from the Sloan Voids . . . . .	135
6.3	Correlations between the Galaxy Luminosity and the Specific Sizes of Void Filaments . . . . .	138
6.4	Summary and Discussion . . . . .	142
<b>7</b>	<b>Concluding Remark</b>	<b>159</b>

요 약	163
Acknowledgement	164
감사의 글	165



# List of Figures

2.1	Number densities of the selected cluster halos (top panel) and the superclusters identified as the FoF groups of the selected cluster halos with linkage parameter of 1/3 (bottom panel) per unit volume at $z = 0$ for five different cosmological models from the CODECS. . . . .	42
2.2	Illustration of the pruning process of a supercluster with 18 nodes identified in the CODECS group catalog at $z = 0$ in the two dimensional plane. All the branches composed of two or less nodes are regarded as not a part of the main stem and thus cut down by the pruning process.	43
2.3	Node number distributions of the supercluster spines for five different models at $z = 0$ . . . . .	44
2.4	Mean specific masses of the supercluster spines at $z = 0$ vs. the cosmological models. . . . .	45
2.5	Size (dashed line) of a supercluster spine in the two dimensional projected plane. . . . .	46
2.6	Projected images of three randomly chosen supercluster spines having same number of nodes but different specific sizes from the $\Lambda$ CDM case at $z = 0$ . . . . .	47
2.7	Mean specific sizes of the supercluster spines for the five models at $z = 0$ .	48
2.8	Redshift evolution of the mean specific sizes of the supercluster spines for the five models. . . . .	49

3.1	Mass functions of the cluster and the supercluster halos at $z = 0$ for three different gravity models in the top and bottom panels, respectively.	66
3.2	Pruning of a supercluster to determine its main stems (spine).	67
3.3	Number distribution of the superclusters as a function of node at $z = 0$ for three different models.	68
3.4	Specific size distributions of the superclusters at $z = 0$ for three different models.	69
3.5	Evolution of the mean specific sizes of the superclusters with the scale factor $a$ for three different models.	70
4.1	Mass functions of the cluster halos and the superclusters for five different models at $z = 0$ in the top and the bottom panel, respectively.	88
4.2	Mean specific sizes of the supercluster spines for five different models at $z = 0$ . The errors represent one standard deviation in the measurement of the mean value.	89
4.3	Evolution of the mean specific sizes of the supercluster spines for five different models.	90
4.4	Cumulative specific size distributions of filaments in DR12 (red open circle), 135 HR4 mocks (gray line), and the mean of mocks (blue line) with the errors calculated as the standard deviation in the mocks. The cumulative specific size distribution of DR12 filaments is consistent to those of HR4.	91
4.5	Number distribution of mean specific sizes of 135 HR4 mock surveys in gray bars. The mean of mock distribution is indicated in blue dashed lines, while that of DR12 is in red dashed line. The mean specific size of DR12 filaments deviates from that of the mock distribution by $1.3\sigma$ .	92
5.1	Configurations of the cluster halos in the filaments for two different cases of the specific sizes.	110
5.2	Number counts of the filaments as a function of the node numbers.	111

5.3	Number counts of the cluster halos contained in the filaments as a function of their masses for five samples before and after the mass-synchronization process in the top and bottom panels, respectively. The specific sizes are in unit of $h^{-1}\text{Mpc}$ . . . . .	112
5.4	Mean substructure abundance of the cluster halos versus the specific sizes of their host filaments. . . . .	113
5.5	Same as Figure 5.4 but for the case that only those clusters whose host filaments have a fixed node number of $N_{\text{node}} = 4$ . . . . .	114
5.6	Same as Figure 5.5 but for the case of $N_{\text{node}} = 5$ . . . . .	115
5.7	Number distribution of the cluster halos as a function of their formation epochs. . . . .	116
5.8	Mean formation epochs of the cluster halos vs. the specific sizes of their host filaments. . . . .	117
5.9	Same as Figure 5.4 but for the case of only those clusters with formation epochs in the narrow range of $0.1 \leq z_{\text{form}} < 0.2$ . . . . .	118
5.10	Same as Figure 5.9 but for the case of $0.2 \leq z_{\text{form}} < 0.3$ . . . . .	119
5.11	Same as Figure 5.9 but for the case of $0.3 \leq z_{\text{form}} < 0.4$ . . . . .	120
5.12	Same as Figure 5.9 but for the case of $0.4 \leq z_{\text{form}} < 0.5$ . . . . .	121
5.13	Same as Figure 5.9 but for the case of $0.5 \leq z_{\text{form}} < 0.6$ . . . . .	122
5.14	Same as Figure 5.9 but for the case of $0.6 \leq z_{\text{form}} < 0.7$ . . . . .	123
5.15	Same as Figure 5.9 but for the case of $0.7 \leq z_{\text{form}} < 0.8$ . . . . .	124
5.16	Same as Figure 5.9 but for the case of $0.8 \leq z_{\text{form}} < 0.9$ . . . . .	125
5.17	Same as Figure 5.4 but for the case of $0.5 \leq z_{\text{form}} < 0.6$ and $N_{\text{node}} = 4$ . . . . .	126
5.18	Cumulative number counts of the substructures in the cluster halos as a function of their rescaled radial distances, $r/r_{\text{vir}}$ for the case that the host filaments have the top 10% largest (blue lines) and the bottom 10% smallest specific sizes (red lines), respectively. . . . .	127

6.1	Size distribution of the void mini-filaments for six different cases of the pruning level $p$ . Here, a void filament represents the primary structure of a MST from which the minor twigs having less than $p$ nodes are removed and its size $S$ is define as its spatial extent. It is clear that the convergence of $dN/d\log S$ in the large $S$ -section appears at $p \geq 5$ . . . .	146
6.2	Number distribution of the sizes of void filaments in interval $[\log S, \log S + d\log S]$ for four various minimum number of galaxies in a void $N_{g,min}$ applied for the giant void selection. . . . .	147
6.3	Number counts of the void filaments having four or more nodes from the Sloan void catalog by Pan et al. (2012) as a function of the node number, $N_{node}$ . . . . .	148
6.4	Specific sizes of the 3172 void filament $\tilde{S} \equiv S/N_{node}$ (size per node) versus the mean absolute $r$ -band magnitude of its member galaxies $ \bar{M}_r $ from our sample. . . . .	149
6.5	A total of 148 void filaments with four or more member galaxies at $0 \leq z \leq 0.02$ from the Sloan void catalog of Pan et al. (2012) in the $\tilde{S} -  \bar{M}_r $ plane. . . . .	150
6.6	Same as Figure 6.5 but for three different bins of the number of node $N_{node}$ . . . . .	151
6.7	Posterior probability density distribution of the real correlation coefficient $\rho$ provided that the Pearson product moment correlation coefficient $r$ has the resulting value from our sample at $0 \leq z \leq 0.02$ for three different cases of $N_{node}$ (solid line). In each panel the dashed line corresponds to the case of a mild correlation ( $\rho = 0.5$ ). . . . .	152
6.8	Same as Figure 6.6 but replacing the specific size $\tilde{S}$ by the linearity $R_L$ to represent the degree of the straightness of the void filaments. . . . .	153
6.9	Specific sizes $\tilde{S}$ of 148 void filaments versus their linearities $R_L$ . . . . .	154

# List of Tables

2.1	Numbers of those supercluster spines with three or more nodes and the fraction occupied by those spines from which the most massive clusters are pruned away. . . . .	50
3.1	Numbers of those supercluster spines with three or more nodes and their mean specific mass for the three models. . . . .	71
6.1	Richness ( $N_{\text{node}}$ ), mean redshift ( $\bar{z}$ ), number of the void filaments ( $N_{\text{fil}}$ ) and Pearson product moment correlation coefficients ( $r$ ). . . . .	155



# Chapter 1

## Overview<sup>1</sup>

The emergence of large-scale structures and their evolution have drawn full attention from both of the theoretical and observational sides. This is not simply because the large-scale structures are ‘large’, but because of their potential to ‘enlarge’ our volume of the understanding of the Universe. Thanks to observational efforts on mapping the distribution of galaxies through large and deep galaxy redshift surveys, and to progress in establishing and simulating the structure formation paradigm, studying the physics and statistics of the large-scale structures of the Universe, more in detail with significantly larger number of samples has become feasible. To enjoy this cosmic renaissance, we dedicate ourselves to filaments, visually the most ubiquitous of the large-scale structures of the Universe. To help the readers understand the theme of this thesis, we provide a brief background in this Chapter.

### 1.1 Cosmic Web Phenomenon in the Universe

It is expected that the matter distribution is statistically homogeneous and isotropic at large enough scale (one of topics in cosmology, on how large the scale has to be, if the scale exists over which the Universe becomes homogeneous and isotropic), rooting on the

---

<sup>1</sup>Previous versions of Sections 1.3 and 1.4 of this chapter were published in the following three papers: Shim & Lee (2013, ApJ, 777, 74); Shim et al. (2014, ApJ, 784, 84); Shim et al. (2015, ApJ, 815, 107). Thus, the copyright belongs to the American Astronomical Society

first principle of physical cosmology, namely the “Cosmological Principle”. Regardless of the efforts dedicated to testify the authenticity of this cosmological assumption at very large scale (Hogg et al. 2005; Yadav et al. 2005; Caldwell & Stebbins 2008; Sylos Labini & Baryshev 2010; Park et al. 2017), what astronomers have obviously confirmed through a large body of observational and numerical studies is that the galaxies (biased tracer of matter) are not uniformly or randomly distributed in space, but apparently are aggregated and evacuated in characteristic ways (Geller & Huchra 1989; Colless et al. 2001; Gott et al. 2005; Springel et al. 2006; Kim et al. 2015; Hwang et al. 2016).

One of the most frequently quoted illustration of this phenomenon was reported by Springel et al. (2006). They compared the galaxy distribution of Millenium simulation with those of the contemporary galaxy redshift surveys, “Two Degree Field Galaxy Redshift Survey” (2dFGRS) (Colless et al. 2001), “Sloan Digital Sky Survey” (SDSS) (Tegmark et al. 2004), and CfA survey (Geller & Huchra 1989). Springel et al. (2006) showed that the observed galaxies amalgamate into the larger structures rather than being evenly distributed. There also existed the regions of low galaxy density surrounded by the structures composed of the galaxies. Similarly in the simulated universe, the configuration of the galaxy distribution resembled the observed ones.

From the three-dimensional version of galaxy distribution map, one can learn more in detail that the overall configuration of the galaxy (matter) distribution in the Universe exhibits an extremely complicated geometry composed of the large-scale structures of four different morphologies, voids, filaments, sheets, and knots. The most prominent and eye-catching feature in the matter distribution is a number of elongated branchy structures, filaments, which are intricately interconnected. The complicated pattern of these large-scale structures as a whole is called the “cosmic web” (Bond et al. 1996) and best manifests the features of the matter distribution as well as the structure formation process.

### 1.1.1 Formation of Cosmic Web

The emergence of the cosmic web can be described by the two main pillars of the current paradigm of the structure formation scenario. One pillar is the primordial density fluctuation and the other is the anisotropic nature of gravitational collapse. In the seminal work of Bond et al. (1996), the authors reported that the blueprint of the present-day cosmic web was encoded in the primordial density field (although it is weak in the early Universe) by learning that filamentary configuration began to emerge far in the past of the history of the Universe. Rare high density peaks in the initial density field, which later evolve into galaxy clusters, were vertices that define the web pattern of the large-scale filaments which bridge the neighboring clusters (Bond et al. 1996).

Courtesy of this natural borne inhomogeneities in the density field, the perturbations were able to grow to form cosmic structures by the gravitational interaction (Peebles 1980). If it were not for the primordial fluctuation (inhomogeneity), the gravitational attraction of a region would have been effectively cancelled out by the surrounding matter distribution. The outcome of gravitational influence on the density perturbation can be summarized with the saying “The rich get richer, while the poor get poorer”. Regions with the excess matter will drag more strongly the matter from the neighboring patches, while the regions with lower density will effectively lose their matter to the surroundings. This process is called “gravitational instability” and illustrates how the cosmic structures are formed and evolved from the density fluctuations of the primordial universe.

One important aspect of the formation of large-scale structures of the cosmic web is that, it apparently manifests filamentary or flattened structures. It is an outcome of anisotropic deformation of the matter under the action of the tidal forces originating from the inhomogeneous initial matter distribution. Because of the inhomogeneities, which were also the main physical driver of the gravitational instability, there always exist anisotropies in the process of the gravitational collapse, due to the gradient of the gravitational force field. In other words, it is the tidal force field that play a crucial role in forming and shaping the cosmic web structures (Bond et al. 1996; Colberg et

al. 1999; Hahn et al. 2007; Platen et al. 2008).

A representative seminal and theoretical approach to describe how the initial perturbations of density become highly anisotropic structures was conducted in 1970 by ‘Zel’dovich’. In the work of Zel’dovich (1970), the growth of the perturbation is treated in the language of linear Lagrangian model, which turns out to be a very simple mathematical framework, but is capable of revealing the important feature(s) of the perturbation growth. By defining deformation tensor and solving for its eigenvalues, it is inevitably predicted that the collapse of matter first initiates in a preferential direction. This demonstration is at the heart of “Zel’dovich approximation” (named after in honor of ‘Zel’dovich’) which betrays the simplified assumption of spherical symmetry of the gravitational collapse.

According to Zel’dovich approximation, the formation of anisotropic structures follows sequential stages, starting from one-dimensional contraction of matter to form the planar structure like sheet or wall, and continues to collapse along the second axis to form the elongated structure like filament, and then finally along the last axis to form the fully collapsed structure like knot or cluster (Shandarin & Zeldovich 1989; Bond & Myers 1996; Sheth et al. 2001; Desjacques 2008; Shandarin & Sunyaev 2009). The final morphology of the structure formed from the density perturbation is determined by the eigenvalues of the deformation tensor. For instance, the number of the eigenvalues above certain threshold for knot, filament, sheet, and void corresponds to 3, 2, 1, and 0, respectively. (The conventional value adopted for the threshold was zero (Zel’dovich 1970; Hahn et al. 2007). However, recent studies suggest different values that are considered to better reproduce the visual impression of the cosmic web structures (Forero-Romero et al. 2009; Libeskind et al. 2012, 2013).)

### 1.1.2 Components of Cosmic Web

The cosmic web can be divided into the four different components, voids, sheets, filaments, and knots, according to their morphological features. Although the subtleties in defining each of the structures may vary from method to method, the most visually

prominent features defining the components of the cosmic web are quite well captured and accepted. For example, the void is a structure which occupies an empty space that is devoid of galaxies, and the filament is an elongated structure and so on. Since these large-scale structures reflect many important clues on the various subjects such as the initial condition of the Universe, the nature of dark sector, gravitational law at cosmological scale, environmental effect on structure formation, and so on, each of the web components vigorously have been studied in multiple directions. Therefore, it is worthwhile to provide a very brief introduction for the characteristics and the applications of each of the web elements, which will be presented in the following subsections.

#### 1.1.2.1 Knot

Knots, often interchangeably called as clusters, are relatively compact large-scale structures of the Universe. The knot is a structure that is collapsed in all three directions having ellipsoidal shape. It is the largest object gravitationally bound, and is located at the densest part of large-scale filaments. It contains approximately 30% of the total amount of matter in the Universe, while the fraction of volume occupying is only  $\sim 0.4\%$ , which is extremely minute (Aragón-Calvo et al. 2010).

As is known from the structure formation theory, the cluster forms at the high density peak of the initial density perturbation. Hence, the statistical properties of the clusters are connected to those of the primordial fluctuations. The statistics such as the mass function, the correlation function, and the power spectrum have been utilized in this context. For example, Bahcall & Cen (1992) (see also Rosati et al. (2002); Bahcall et al. (2003)) estimated  $\sigma_8$ , the normalization of the power spectrum, with the cluster mass function. Constraints on the shape and the amplitude of power spectrum of the underlying matter were also placed, by studying the statistical properties of clustering based on X-ray clusters (Eke et al. 1996; Borgani & Guzzo 2001; Moscardini et al. 2001).

### 1.1.2.2 Sheet

Sheets (walls) are the large-scale structures of planar shape, that are collapsed in one direction. Due to their low mass fraction, wall structures are relatively inconspicuous compared to the other cosmic web components (Aragón-Calvo et al. 2010; Cautun et al. 2014). However, the most largest structures observed may be the walls, possibly together with filaments. The earliest example of the flattened structure nearby, may be the well-established supergalactic plane (de Vaucouleurs 1953), which now is considered to be a part of the nearby filament and sheet (Lahav et al. 2000). It is now well known that wall-like great structures reveal themselves in the observed distribution of the galaxies. Particularly striking examples are the CfA Great Wall (Geller & Huchra 1989), followed by the larger Sloan Great Wall (Gott et al. 2005), and again followed by the even larger BOSS Great Wall (Lietzen et al. 2016).

To test the statistical properties of the initial perturbations, the existence of the extremely large structures has been investigated. For instance, Sheth & Diaferio (2011) estimated probability with excursion set theory that the largest-scale structure observed form from the Gaussian random density field, and claimed that the existence of the Sloan Great Wall is hard to reconcile with the assumed density field. Similar context, but contradictory conclusion was made by Park et al. (2012) and Hwang et al. (2016), with help of cosmological N-body simulations. In these numerical works, the authors reported that the observed structures of such physical size, for example, the CfA Great Wall or the Sloan Great Wall, are safely guaranteed to form under the concordance  $\Lambda$ CDM cosmology with the Gaussian random fluctuations, and explained that the scheme for galaxy assignment and large-scale structure identification may bother fair comparison between the simulated and observed large-scale structures leading to the different interpretation (Park et al. 2012).

### 1.1.2.3 Filament

Filaments, visually the most ubiquitous of large-scale structures of the Universe, are often characterized as the structures that are collapsed along two axes resulting in

elongated morphologies. Filaments are known to contain more than half of the observed galaxies (or mass, in simulations) (Aragón-Calvo et al. 2010; Cautun et al. 2014; Tempel et al. 2014; Eardley et al. 2015), therefore the filaments are used for structure formation and testing cosmological models.

Particularly, there is a growing demand for revealing the environmental influence of the large-scale structures on the formation and evolution of galaxies. Recently, Guo et al. (2015) showed that the luminosity functions of satellites are significantly different, depending on whether or not their primary galaxies reside in filaments. Also a large body of studies regarding the spin axis alignment of galaxies to the filaments have been conducted and showed that the spin axis of spiral galaxy is parallel to its host filament (Jones et al. 2010; Tempel & Libeskind 2013; Tempel et al. 2013; Pahwa et al. 2016). Several studies based on observational data found that filaments play a role in enhancing the star formation activities (Fadda et al. 2008; Biviano et al. 2011; Darvish et al. 2014).

On the other hand, the filamentary structures have been also utilized in a different nuance, to constrain cosmological models by examining the characteristics of the filaments reflecting the anisotropic nature of the gravitational clustering (West et al. 1991; Basilakos et al. 2001; Kolokotronis et al. 2002; Wray et al. 2006). For example, Basilakos et al. (2001); Kolokotronis et al. (2002) showed that the  $\Lambda$ CDM universe with its parameters set to ( $\Omega_\Lambda = 1 - \Omega_m = 0.7$ ) deviates the least from the observed shape distribution of filamentary structures, where  $\Omega_\Lambda$ ,  $\Omega_m$  stand for the density parameters of the cosmological constant and matter, respectively.

#### 1.1.2.4 Void

Voids are the underdense regions surrounded by elongated filaments, sheet-like walls, and dense compact knots. As its name suggests, voids contain small amount of matter in the Universe (Cautun et al. 2014; Nuza et al. 2014). Although voids contain only small portion of matter, their physical sizes typically range from  $20h^{-1}Mpc$  to  $50h^{-1}Mpc$  occupying the major share of the volume of the Universe (Cautun et al. 2014)

Void, due to its extreme low density, is expected to show clear environmental dependences of galaxy properties. Thanks to this advantage, the environmental effect of low density on the properties of galaxies, including stellar mass (Beygu et al. 2017), color and luminosity function (Tavasoli et al. 2015), star formation (Rojas et al. 2004, 2005; Ricciardelli et al. 2014), and gas content (Kreckel et al. 2011), have been studied. It is reported that void galaxies are bluer in color with more active star formation than their overdense counterparts.

In cosmological context, the abundance, morphology, and dynamics of voids are utilized to constrain cosmological models, since they reflect the nature of dark energy and gravitational law. For example, Park & Lee (2007) and Park & Lee (2009) suggested that the elliptical shapes of voids may provide powerful constraints on the key cosmological parameters including the dark energy equation of state (see also Lavaux & Wandelt (2010)). Pisani et al. (2015) showed that the number of voids sensitively depends on the nature of dark energy based on the analytical framework of Sheth & van de Weygaert (2004). On the other hand, the models of modified gravity have been tested with voids, because screening mechanism is expected to be deactivated in these low density regions, and to reveal their cosmological features (refer to Zivick et al. (2015); Falck et al. (2018); Mota (2018)). In another direction, the statistical properties of the primordial fluctuation were studied with void (Kamionkowski et al. 2009), because of the merit of voids in preserving the initial conditions owing to their rarified nature (Kim & Park 1998).

## 1.2 Identifying Filamentary Structures

As shown in the previous sections, the cosmic web has now become an irreplaceable laboratory for diverse astronomical studies, and has been fully exploited to dig out the information concerning the initial density perturbation, structure formation, nature of dark sector, and gravitational law. Of course, systematic ways for defining and characterizing the cosmic web have also been receiving tremendous attention, and a lot of efforts have been dedicated to this mission.

Unlike the identification of virialized halos, a common framework classifying the large-scale structures has not yet been established. Developing an unique identification scheme is a difficult task, in a sense that no absolute definition exists in describing different large-scale structures. This is partly due to the complexity and asymmetry in its geometry of these individual structure. In addition, the intrinsic multi-scale nature and broad density range of the web elements also render the construction of the unique classification and quantification ever more challenging.

Instead, various identification methods have been applied to both observation and simulation data to best fulfill their own goals in mind. In consequence, the resulting classification of respective method does not assume a priori match to the others, and has its own advantages suited for its primary goals. Hence, it is meaningless to ask which is the most superb one, but it will be better to skim the characteristic features of some popular methods (see Libeskind et al. (2018) for detailed comparison between various methods) for appropriate application and analysis.

### 1.2.1 Filament Finding Algorithms

Various methods can crudely be categorized into two classes, geometric and dynamic approaches. The latter approach was devised in an analogy to the Zel'dovich approximation and focused on dynamical status of structures. Since the formation and evolution of the cosmic large-scale structures are originated by the tidal forces (Bond et al. 1996), Hessian of the gravitational potential, the tidal tensor, was used to identify and classify the structures of the cosmic web. Similar to the work of Zel'dovich (1970), the number of eigenvalues of the tidal tensor above  $\lambda_{th}$  determines the classification, where  $\lambda_{th}$  stands for the threshold value. For example, the web structures were determined with  $\lambda_{th} = 0$  by evaluating the tidal tensor from non-linear (Hahn et al. 2007) and linear potential (Lee & Lee 2008). To give a better match to the visual impression, the resemblance between visual inspection and the classification based on this scheme was studied as a function of the threshold  $\lambda_{th}$ . It was found that some positive value gives a nice agreement (Forero-Romero et al. 2009). Later, the concept of dynamics of

the structure formation to define large-scale structures was extended to velocity field. Hoffman et al. (2012) identified the web structures by evaluating eigenvalues of the velocity shear tensor, and found that this velocity-based method resolves better than the tidal-based ones.

The other group of the cosmic web finding algorithms weighs on the geometry of matter distribution. These approaches define each component of the cosmic web by utilizing characteristics of its geometry from the point distributions. The most intuitive application of this idea is a graph theory based analysis called “Minimal Spanning Tree” which defines filamentary structures through identifying their intrinsic connected pattern by linking point sources, for example galaxies or clusters (Barrow et al. 1985; Graham et al. 1995; Colberg 2007). Slightly different point process based approach, the Bisous model, which yields the confidence estimate of each detected structure via Bayesian framework also appeared in Stoica et al. (2005, 2010); Tempel et al. (2016). Another attempt in this second kind to assess the cosmic web was carried out by examining the connectivity and topology of the matter distribution involved. Colombi et al. (2000) was the first to implement the Morse theory (Morse 1934) for the cosmological use. This approach was extended by Novikov et al. (2006) and Sousbie et al. (2008) respectively in 2D and 3D, by establishing the skeleton analysis, which treats the set of critical points of density fields to delineate the cosmic structures.

### 1.2.2 Minimal Spanning Tree Method

In this subsection, I will elaborate more on the MST algorithm, because all the analyses presented in the thesis are based on the Minimal Spanning Tree (hereafter, MST) technique to extract elongated filamentary structures from both observation and simulation data.

As briefly mentioned above, the MST method is a way of connecting points based on the graph theory. The first application of the MST method for a cosmological analysis was done by Barrow et al. (1985) to study galaxy clustering. Later, the MST was adopted by others to study geometric properties of large-scale structures (Krzewina &

Saslaw 1996; Doroshkevich et al. 2001; Colberg 2007; Park & Lee 2009). To understand what is extracted from a point (node) distribution, it is worth learning the definition of the MST. The key elements to describe the concept of a MST are path and circuit. A path is nothing but a sequence of straight lines joining two nodes, and a circuit is a path that is closed (i.e. that has loop). If a path without any circuit, defined as tree, includes all nodes, it is called spanning tree. Finally, one that minimizes the sum of the edge lengths is identified as “Minimal Spanning Tree”, among a number of different spanning trees from the point distribution of interest. The MST is an uniquely connected pattern unless there exist identical edge lengths (Barrow et al. 1985; Colberg 2007).

As listed in the previous section, there are many tactics to describe the cosmic web structures. Partly due to the absence of the definite boundary (at least vague) among the web components, each identification scheme has its own strength. For the case of the MST, an analysis of structures is done with points, halos of clusters for the majority of the works in this thesis. Since the MST method can be applied directly to bound objects unlike most of the dynamical methods, no additional smoothing is necessary. For the fair comparison between the large-scale structures in observation and simulation, the compatibility of the method becomes critical. Fortunately, the MST does not require information that is unobservable or hard to measure in observation, for example velocities of dark matter halos, which are necessary for some other approaches by construction (Falck et al. 2012; Hoffman et al. 2012). The merit of the MST algorithm is that it can identify the filaments directly from the distributions of point-like objects. However, this very merit indicates that the method would fail to capture dynamical properties of the filaments, which was a motivation for the dynamics-based classifications (Hahn et al. 2007; Forero-Romero et al. 2009; Hoffman et al. 2012).

### 1.3 Filaments and Cosmology

The deepest and the most profound question in modern cosmology is what caused the universe to accelerate at the present epoch. Although the Planck mission team recently confirmed the stunning agreements between the predictions of the standard

$\Lambda$ CDM (cosmological constant  $\Lambda$ +cold dark matter) model and the CMB temperature power spectrum measured with unprecedentedly high precision (Planck collaboration XV 2013; Planck Collaboration XVI 2013), the notorious fine tuning problem of  $\Lambda$  still haunts the cosmologists to vigorously look for alternative models.

There have been two main directions in developing viable alternatives. One direction is to replace  $\Lambda$  with some dynamic dark energy with negative pressure that could induce the current acceleration of the universe without requiring fine tuned conditions (see Amendola & Tsujikawa 2010, for a comprehensive review). Among various dynamic dark energy scenarios, the coupled dark energy (cDE) model where a scalar field dark energy interacts with dark matter (Wetterich 1995; Mangano et al. 2003; Amendola 2000, 2004; Macciò et al. 2004; Pettorino & Baccigalupi 2008; Baldi et al. 2010; Wintergerst & Pettorino 2010) has been found quite promising because of its capacity of alleviating several reported tensions between the  $\Lambda$ CDM model and the observations (e.g., Baldi et al. 2011; Baldi 2012a; Lee & Baldi 2012; Salvatelli & Marchini 2013). This capacity of the cDE models to alleviate the tensions posed by the observational anomalies is mainly owing to the presence of an additional long-range fifth force induced by the dark sector coupling (the interaction between dark energy and nonbaryonic dark matter). See Amendola & Tsujikawa (2010) for a comprehensive review of the cDE models.

The other main direction is to modify the general relativity (GR) on the large scale, which makes the concept of anti-gravitational dark energy unnecessary to explain the observed distance-luminosity relation of Type Ia supernovae (see Clifton et al. 2012, for a comprehensive review). The tremendous success of GR on the local scale, however, leaves only very little room for possible deviation of true gravity from GR. The  $f(R)$  gravity is one of those few modified gravity models which has so far survived severe cosmological tests (Reyes et al. 2010; Wojtak et al. 2011). In this model,  $f(R)$  represents an arbitrary function of the Ricci scalar  $R$  that is substituted for  $R$  in the Einstein-Hilbert action, and the derivative,  $df/dR$ , induces a fifth force on the large scale, the strength of which is quantified by its absolute magnitude at the present epoch,

$f_{R0} \equiv |df/dR|_0$  (Sotiriou & Faraoni 2010; de Felice & Tsujikawa 2010). An essential feature of the  $f(R)$  gravity is the presence of the chameleon mechanism that blocks deviation of gravity from the GR in dense environment: The denser the environment is, the weaker the fifth force is (Khoury & Weltman 2004; Li & Barrow 2007).

Conventionally, the gravitational clustering of the large-scale structure (LSS) and its evolution have been used for constraining the key cosmological parameters of the  $\Lambda$ CDM cosmology (e.g., Addison et al. 2013; Di Dio et al. 2014, and references therein). For example, the basic statistics such as the two point-correlation function of the density field, the mass function of galaxy clusters and the matter-to-halo bias are frequently employed to quantify the strength of the clustering of LSS and to put tight constraints on the matter density parameter ( $\Omega_m$ ), the amplitude of the linear power spectrum ( $\sigma_8$ ) and the dark energy equation of state ( $w$ ). The basic statistics of LSS have played a vital role in establishing the concordance  $\Lambda$ CDM (cosmological constant  $\Lambda$  and cold dark matter) cosmology.

The LSS statistics were also utilized for testing the viability of the alternative cosmologies such as the warm dark matter (WDM), coupled dark energy (cDE), and modified theories of gravity (MG) (e.g., Sutter & Ricker 2008; Song & Koyama 2009; Stril et al. 2010; Smith & Markovic 2011; Lombriser et al. 2012; Abebe et al. 2013; Moresco et al. 2013). However, some cautionary remarks have been recently raised on the rosy prospects for the basic statistics of LSS as a powerful discriminator of the alternative cosmologies. For instance, the abundance of galaxy clusters and the strength of their gravitational clusterings, which have been widely used as one of the most powerful probes of the background cosmology (for a review, see Allen et al. 2011), are unlikely to be efficient discriminators of modified gravity, since the galaxy clusters are usually located in the highly dense supercluster environments where the chameleon effect should be very strong. Furthermore, what Baldi et al. (2014) noted in the studies based on the N-body analysis was that the  $f(R) + \nu$  and the  $\Lambda$ CDM models yielded essentially the same basic statistics of LSS. The effect of free streaming of massive neutrinos (Lesgourgues & Pastor 2006) effectively cancels out that of the fifth force of

the  $f(R)$  gravity on the large scale structure.

On the other hand, it was shown by Bean et al. (2008) that the cDE models whose strength of dark sector coupling is tightly constrained by the recent observations are very hard to distinguish from the  $\Lambda$ CDM cosmology. Wei et al. (2013) theoretically proved that the WDM, cDE and MG models are hard to be differentiated from one another just by tracing the expansion and growth history with the LSS observations. These are indications of the fundamental limitation of the basic statistics of LSS as a test of alternative cosmologies, concluding that a novel statistics independent of the standard observables is necessary.

The spatial clustering of galaxy clusters that collectively generates the cosmic web phenomenon (Bond et al. 1996) has been regarded as one of the most powerful indicators of underlying cosmology. As the dark sector coupling and gravity would affect not only the strength of the large-scale clustering but also its degree of anisotropy, the cosmic web must take on a different pattern in different cosmology. The anisotropic clustering of clusters is well manifested by the elongated filamentary shapes of the rich superclusters which correspond to the densest section of the cosmic web. In the literatures which studied the superclusters and their morphological properties, the shapes of the superclusters were measured by various different algorithms such as percolation, ellipsoid-fitting, friends-of-friends, Minkowski functional and etc. (e.g., Dekel et al. 1984; West 1989; Plionis et al. 1992; Jaaniste et al. 1998; Basilakos et al. 2001; Basilakos 2003; Basilakos et al. 2006; Einasto et al. 2007; Wray et al. 2006; Einasto et al. 2011). The general consensus of those previous works was that no matter what algorithm was used, the richer superclusters appear to have more filamentary shapes. Recently, Einasto et al. (2011) noted that the shape of a richest supercluster located in the highly overdense region is best described as a “multi-branch” filament consisting of the main stem and several branches.

Assuming that the degree of the straightness of the supercluster main stems would depend strongly on the dynamics of dark energy and gravity, it is expected that in cDE and  $f(R)$  gravity models the main stems of rich superclusters would be less straight,

having shorter spatial extents compared with the  $\Lambda$ CDM case, due to the effect of the fifth force. The fifth force generated by the coupling between dark matter and dark energy in cDE models will play a role in making the gravitational clustering of galaxy clusters less isotropic, which is best manifested by the straightness of the superclusters that correspond to the most prominent filamentary structures of the cosmic web. It is also intriguing to ask if the long-range fifth force generated by the scalaron in the  $f(R)$  gravity model also affects on the supercluster straightness. The essential work to undertake here is to investigate quantitatively how sensitively the degree of the supercluster straightness changes by the presence of  $f(R)$  gravity and to examine whether or not it would be powerful enough to distinguish  $f(R)$  not only from GR but also from cDE.

## 1.4 Filaments and Galaxy (Halo) Formation and Evolution

As a number of previous studies listed in previous section have revealed that filamentary structures are deeply involved in the process of formation and evolution of galaxies (halos), it is of crucial importance to examine the correlation between galaxy (halo) properties and characteristics of the host filaments. Influence on the properties of galaxies (halos) by filaments will be studied in two filament environments, for example, large-scale filaments with clusters and small-scale filaments with galaxies in voids.

### 1.4.1 Filaments and Substructure Abundance of Cluster Halos

The substructure of dark matter halos has been the subject of many literatures in which analytical and/or numerical methods were employed to investigate such intriguing topics as the mass and spatial distributions of substructures, the dependence of substructure abundance on the large-scale density and tidal fields as well as on the host halo mass, the effects of tidal stripping and dynamical friction on the survival rates of substructures and so on (e.g., Tormen et al. 1998; Sheth 2003; Lee 2004; De Lucia et al. 2004; Natarajan & Springel 2004; Oguri & Lee 2004; van den Bosch et

al. 2005; Hahn et al. 2009; Hester & Tasitsiomi 2010; Gao et al. 2011; Tillson et al. 2011; Wang et al. 2011; Croft et al. 2012; Wu et al. 2013; Xie & Gao 2015; Jiang & van den Bosch 2017; Borzyszkowski et al. 2017; Garaldi et al. 2017). Owing to those previous endeavors, a coarse roadmap is now established to explain the presence and properties of the substructures of dark matter halos in the standard  $\Lambda$ CDM ( $\Lambda$  + Cold Dark Matter) universe.

The presence of substructures in a bound halo is a natural consequence of hierarchical merging process. Once a substructure forms, it is prone to severe mass-loss due to various dynamical effects such as tidal stripping, close encounter, and dynamical friction inside its host halo (e.g., Tormen et al. 1998; Taylor & Babul 2004). The longer a substructure is exposed to those dynamical effects, the harder it can survive. Thus, at fixed mass a halo that forms earlier tends to contain less number of substructures (or equivalently, less mass fraction) (e.g., see Jiang & van den Bosch 2017). Among various factors that affect the formation epoch of a halo, the most principal one has been found the strength of the external tidal forces exerted by the neighbor halos, which tend to interrupt the infall of satellites and the accretion of matter particles onto the halo: The galactic halos of fixed mass in the stronger tidal fields form on average earlier and in consequence possess less substructures (Wang et al. 2011).

It is not only the tidal strength but also the the configurations of the tidal fields in the surrounding that play a crucial role in the obstruction of the satellite infall and mass accretion into the halos (Hahn et al. 2009; Shi et al. 2015; Borzyszkowski et al. 2017). Two recent numerical studies based on the high-resolution simulations (Borzyszkowski et al. 2017; Garaldi et al. 2017) found a significant difference in the substructure abundance between the galactic halos located in two different tidal environments. One is inside a thick "prominent" filament while the other is at the junction of multiple thin "secondary" filaments. For the former case, the satellite infall and matter accretion into a galactic halo is encumbered since the satellites and matter particles develop tangential velocities perpendicular to the direction of the elongated axis of the filament, while for the latter case the satellites and matter particles can acquire radial motions falling

onto the halos (Borzyszkowski et al. 2017). The galactic halos located in the bulky straight filaments tend to form early before the complete formation of the filaments, which leads to smaller number of substructures than their counterparts at the present epoch (Garaldi et al. 2017).

As the main purpose of the previous works that have established the above roadmap was to physically explain the assembly bias on the galactic scale as well as a paucity of satellites around the Milky Way (Gao & White 2007), their focus was primarily put on the galactic halos and their substructures (Hahn et al. 2009; Mao et al. 2015). Although it is expected that the formation of the substructures of the cluster halos would be similarly affected by the tidal fields, the link between the substructure abundances of the cluster halos and the external tidal field may not be the formation epochs unlike for the case of the galactic halos. It was indeed numerically found that the formation epochs of the cluster halos were nearly independent of the strength of the external tidal forces and that the formation epochs (or equivalently the concentration parameters) of cluster halos at fixed mass did not play the most decisive role in shaping the substructure abundance (Gao et al. 2011). Besides, on the cluster scale it is difficult to make a quantitative distinction between the thick primary and the thin secondary filaments unlike on the galactic scale, and thus the results of Borzyszkowski et al. (2017) and Garaldi et al. (2017) cannot be readily extended to the cluster scale. Thus, it is necessary to take a different approach to address the issue of the tidal effect, which will be represented in terms of the specific sizes of the filaments, on the substructure abundance of the cluster halos.

#### **1.4.2 Filaments and Luminosity of Void Galaxies**

Despite its extreme low-density, a void exhibits a dilute miniature of the cosmic web that interconnects the void galaxies (e.g., Sahni et al. 1994; Gottlöber et al. 2003; Kreckel et al. 2011; Aragon-Calvo & Szalay 2013; Alpaslan et al. 2014). The anisotropic spatial correlation of the tidal shear field is believed to be mainly responsible for the formation of the mini-web in a void just as it is for the cosmic web in the whole universe (van

de Weygaert & van Kampen 1993; Bond et al. 1996). As the tidal shear field develops nonlinear correlations during the evolutionary process, the mini-web in a void region should become more and more filamentary.

An intriguing issue is what effect the filamentary mini-web has on the evolution of the void galaxies and how strong it is. This can be addressed by looking for correlations between the intrinsic properties of the void galaxies and the characteristics of the void filaments. In fact, the voids should be an optimal ground for the investigation of the effect of the filamentary web on the galaxy evolution (e.g., see Kreckel et al. 2011). First of all, since the void filaments are much less intricate than their wall counterparts, it is less difficult to identify and characterize them. Furthermore, since the densities of the voids are all constrained to extremely low values, the effect of the environmental density on the properties of the void galaxies can be controlled and thus it should be easier to single out the dependence of the galaxy properties on the filamentary web for the case of the void galaxies.

The mini-filaments that pass through a void are expected to bridge the void galaxies with the surrounding denser regions. Hence, the gas and dark matter from the surroundings can be transported into the void regions along the mini-filaments, which would enhance the growth of the void galaxies (Park & Lee 2009b; Kreckel et al. 2011). The recent observation of Beygu et al. (2013) which reported a detection of real-time star-forming activities in the void galaxies embedded in the filamentary channels full of HI cold gases is in line with this picture that the void galaxies can rapidly grow through the filamentary connection with the surroundings.

The bridge effect of void filaments was first noted and quantitatively investigated in the numerical work of Park & Lee (2009b) using the Millennium Run semi-analytic galaxy catalog (Springel et al. 2005). What they found was that the intrinsic properties of the void galaxies such as the total mass, luminosity and blackhole mass are strongly correlated with the degree of the straightness of the host filaments. Park & Lee (2009b) suggested that the presence of this correlation should be attributed to the dependence of the efficacy of gas transportation on the geometrical shapes of the void filaments:

the more straight void filaments should more efficiently carry gas and matter onto the void galaxies.

If the presence of the bridge effect of void filaments is observationally confirmed, it will provide an important clue to the mechanism through which the void galaxies become gas richer, bluer colored, and have higher specific star formation rates than their wall counterparts (e.g., Rojas et al. 2004; Kreckel et al. 2011; Beygu et al. 2013; Ricciardelli et al. 2014).

## 1.5 In this Thesis

The studies of the large-scale structures have recently been benefited from the cosmic renaissance, in a sense that the widest and deepest ever galaxy redshift surveys have already been operating (or are about to operate) and releasing (will release) tremendous amount of observational data, for example, SDSS (Albaret et al. 2017), DES (DES Collaboration et al. 2017), Euclid (Laureijs et al. 2011), and so on.

At the same time, the accelerated advancement in computing power and skills are achieved. These revolutions allow us to study the statistics and physics of the large-scale structures in the Universe, more in detail with significantly larger number of samples, in order to give better constraints on cosmological models and/or to study the structure formation and evolution (including the galaxy formation and evolution). Jumping on this large-scale structure bandwagon, I present cosmological applications of filaments in the thesis, which are the most ubiquitous structures that containing more than half of the matter in the Universe, and that demonstrating the anisotropic collapse of matter under the tidal influence.

Cosmological applications of filamentary structures have been made in two different directions. The first direction is to examine the cosmological dependence of large-scale filamentary structures, while the other is to study the role of filaments in the formation and evolution of dark matter halos and galaxies. In Part 1, superclusters, as clusters of galaxy clusters, in various cosmological models are analyzed. In Chapter 2, the degree of straightness of the superclusters in the concordance  $\Lambda$ CDM is compared to that

of coupled dark energy, a model which relaxes the conventional assumption of non-interaction in the dark sector. Similar analysis on the large-scale filaments in  $\Lambda$ CDM and  $f(R)$  gravity model, one of modified theory of gravity, is presented in Chapter 3. In Chapter 4, the effect of  $f(R)$  gravity plus massive neutrinos on the shapes of superclusters are discussed. In Part 2, the properties of the member halos (galaxies) in different types of host filaments are studied. The substructure abundance and its radial profile of the massive halos in large-scale filaments of different configurations are treated in Chapter 5, while in Chapter 6 the correlation between the straightness of filaments in void and their member galaxy luminosity is investigated.

# Bibliography

- Albareti, F. D., Allende Prieto, C., Almeida, A., et al. 2017, *ApJS*, 233, 25
- Aragón-Calvo, M. A., van de Weygaert, R., & Jones, B. J. T. 2010, *MNRAS*, 408, 2163
- Arbabi-Bidgoli, S., & Müller, V. 2002, *MNRAS*, 332, 205
- Bagchi, J., Sankhyayan, S., Sarkar, P., et al. 2017, *ApJ*, 844, 25
- Bahcall, N. A., & Cen, R. 1992, *ApJ*, 398, L81
- Bahcall, N. A., Dong, F., Bode, P., et al. 2003, *ApJ*, 585, 182
- Barrow, J. D., Bhavsar, S. P., & Sonoda, D. H. 1985, *MNRAS*, 216, 17
- Basilakos, S., Plionis, M., & Rowan-Robinson, M. 2001, *MNRAS*, 323, 47
- Beygu, B., Peletier, R. F., van der Hulst, J. M., et al. 2017, *MNRAS*, 464, 666
- Biviano, A., Fadda, D., Durret, F., Edwards, L. O. V., & Marleau, F. 2011, *A&A*, 532, A77
- Bond, J. R., Kofman, L., & Pogosyan, D. 1996, *Nature*, 380, 603
- Bond, J. R., & Myers, S. T. 1996, *ApJS*, 103, 1
- Bonjean, V., Aghanim, N., Salomé, P., Douspis, M., & Beelen, A. 2018, *A&A*, 609, A49
- Borgani, S., & Guzzo, L. 2001, *Nature*, 409, 39
- Caldwell, R. R., & Stebbins, A. 2008, *Physical Review Letters*, 100, 191302

- Cautun, M., van de Weygaert, R., Jones, B. J. T., & Frenk, C. S. 2014, MNRAS, 441, 2923
- Colberg, J. M., White, S. D. M., Jenkins, A., & Pearce, F. R. 1999, MNRAS, 308, 593
- Colberg, J. M. 2007, MNRAS, 375, 337
- Colombi, S., Pogosyan, D., & Souradeep, T. 2000, Physical Review Letters, 85, 5515
- Colless, M., Dalton, G., Maddox, S., et al. 2001, MNRAS, 328, 1039
- Coppin, K. E. K., Geach, J. E., Webb, T. M. A., et al. 2012, ApJ, 749, L43
- Darvish, B., Sobral, D., Mobasher, B., et al. 2014, ApJ, 796, 51
- Dawson, K. S., Kneib, J.-P., Percival, W. J., et al. 2016, AJ, 151, 44
- DES Collaboration, Abbott, T. M. C., Abdalla, F. B., et al. 2017, arXiv:1711.00403
- Desjacques, V. 2008, MNRAS, 388, 638
- Doroshkevich, A. G., Tucker, D. L., Fong, R., Turchaninov, V., & Lin, H. 2001, MNRAS, 322, 369
- de Lapparent, V., Geller, M. J., & Huchra, J. P. 1986, ApJ, 302, L1
- de Vaucouleurs, G. 1953, AJ, 58, 30
- Dietrich, J. P., Werner, N., Clowe, D., et al. 2012, Nature, 487, 202
- Dubinski, J., da Costa, L. N., Goldwirth, D. S., Lecar, M., & Piran, T. 1993, ApJ, 410, 458
- Eardley, E., Peacock, J. A., McNaught-Roberts, T., et al. 2015, MNRAS, 448, 3665
- Ebeling, H., Barrett, E., & Donovan, D. 2004, ApJ, 609, L49
- Einasto, M., Gramann, M., Saar, E., et al. 2015, A&A, 580, A69
- Eke, V. R., Cole, S., Frenk, C. S., & Navarro, J. F. 1996, MNRAS, 281, 703

- El-Ad, H., & Piran, T. 2000, MNRAS, 313, 553
- Fadda, D., Biviano, A., Marleau, F. R., et al. 2008, ApJ, 672, L9
- Falck, B., Koyama, K., Zhao, G.-B., & Cautun, M. 2018, MNRAS, 475, 3262
- Falck, B. L., Neyrinck, M. C., & Szalay, A. S. 2012, ApJ, 754, 126
- Fixsen, D. J. 2009, ApJ, 707, 916
- Fixsen, D. J., Cheng, E. S., Gales, J. M., et al. 1996, ApJ, 473, 576
- Forero-Romero, J. E., Hoffman, Y., Gottlöber, S., Klypin, A., & Yepes, G. 2009, MNRAS, 396, 1815
- Geller, M. J., & Huchra, J. P. 1989, Science, 246, 897
- Gott, J. R., III, Jurić, M., Schlegel, D., et al. 2005, ApJ, 624, 463
- Graham, M. J., Clowes, R. G., & Campusano, L. E. 1995, MNRAS, 275, 790
- Guo, Q., Tempel, E., & Libeskind, N. I. 2015, ApJ, 800, 112
- Hahn, O., Porciani, C., Carollo, C. M., & Dekel, A. 2007, MNRAS, 375, 489
- Hoffman, Y., Metuki, O., Yepes, G., et al. 2012, MNRAS, 425, 2049
- Hogg, D. W., Eisenstein, D. J., Blanton, M. R., et al. 2005, ApJ, 624, 54
- Hoyle, F., & Vogeley, M. S. 2002, ApJ, 566, 641
- Huchra, J. P., Macri, L. M., Masters, K. L., et al. 2012, ApJS, 199, 26
- Hwang, H. S., Geller, M. J., Park, C., et al. 2016, ApJ, 818, 173
- Jauzac, M., Jullo, E., Kneib, J.-P., et al. 2012, MNRAS, 426, 3369
- Jones, B. J. T., van de Weygaert, R. & Aragón-Calvo, M. A. 2010, MNRAS, 408, 897
- Kamionkowski, M., Verde, L., & Jimenez, R. 2009, Journal of Cosmology and Astroparticle Physics, 1, 010

- Kim, J., Park, C., L'Huillier, B., & Hong, S. E. 2015, *Journal of Korean Astronomical Society*, 48, 213
- Kim, M., & Park, C. 1998, *Journal of Korean Astronomical Society*, 31, 109
- Kim, S., Rey, S.-C., Bureau, M., et al. 2016, *ApJ*, 833, 207
- Kirshner, R. P., Oemler, A., Jr., Schechter, P. L., & Shectman, S. A. 1981, *ApJ*, 248, L57
- Kirshner, R. P., Oemler, A., Jr., Schechter, P. L., & Shectman, S. A. 1987, *ApJ*, 314, 493
- Kolokotronis, V., Basilakos, S., & Plionis, M. 2002, *MNRAS*, 331, 1020
- Krzewina, L. G., & Saslaw, W. C. 1996, *MNRAS*, 278, 869
- Kreckel, K., Platen, E., Aragón-Calvo, M. A., et al. 2011, *AJ*, 141, 4
- Kuutma, T., Tamm, A., & Tempel, E. 2017, *A&A*, 600, L6
- Lahav, O., Santiago, B. X., Webster, A. M., et al. 2000, *MNRAS*, 312, 166
- Laureijs, R., Amiaux, J., Arduini, S., et al. 2011, arXiv:1110.3193
- Lavaux, G., & Wandelt, B. D. 2010, *MNRAS*, 403, 1392
- Lee, J., & Lee, B. 2008, *ApJ*, 688, 78
- Lee, J., Kim, S., & Rey, S.-C. 2015, *ApJ*, 807, 122
- Lee, J., & Park, D. 2009, *ApJ*, 696, L10
- Libeskind, N. I., Hoffman, Y., Knebe, A., et al. 2012, *MNRAS*, 421, L137
- Libeskind, N. I., Hoffman, Y., Forero-Romero, J., et al. 2013, *MNRAS*, 428, 2489
- Libeskind, N. I., van de Weygaert, R., Cautun, M., et al. 2018, *MNRAS*, 473, 1195
- Lietzen, H., Tempel, E., Liivamägi, L. J., et al. 2016, *A&A*, 588, L4

- Matsuda, Y., Yamada, T., Hayashino, T., et al. 2005, *ApJ*, 634, L125
- Morse M., 1934, *Am. Math. Soc. Colloquium Publ.*, 18, 1
- Moscardini, L., Matarrese, S., & Mo, H. J. 2001, *MNRAS*, 327, 422
- Mota, D. F. 2018, *International Journal of Modern Physics D*, 27, 1830003
- Neyrinck, M. C. 2008, *MNRAS*, 386, 2101
- Novikov, D., Colombi, S., & Doré, O. 2006, *MNRAS*, 366, 1201
- Nuza, S. E., Kitaura, F.-S., Heß, S., Libeskind, N. I., & Müller, V. 2014, *MNRAS*, 445, 988
- Pahwa, I., Libeskind, N. I., Tempel, E., et al. 2016, *MNRAS*, 457, 695
- Pan, D. C., Vogeley, M. S., Hoyle, F., Choi, Y.-Y., & Park, C. 2012, *MNRAS*, 421, 926
- Park, C., Choi, Y.-Y., Kim, J., et al. 2012, *ApJ*, 759, L7
- Park, C.-G., Hyun, H., Noh, H., & Hwang, J.-c. 2017, *MNRAS*, 469, 1924
- Park, D., & Lee, J. 2007, *Physical Review Letters*, 98, 081301
- Park, D., & Lee, J. 2009, *MNRAS*, 397, 2163
- Peebles, P. J. E. 1980, *Research supported by the National Science Foundation*. Princeton, N.J., Princeton University Press, 1980. 435 p.
- Pisani, A., Sutter, P. M., Hamaus, N., et al. 2015, *Phys. Rev. D*, 92, 083531
- Planck Collaboration, Ade, P. A. R., Aghanim, N., et al. 2016, *A&A*, 594, A13
- Platen, E., van de Weygaert, R., & Jones, B. J. T. 2008, *MNRAS*, 387, 128
- Plionis, M., & Basilakos, S. 2002, *MNRAS*, 330, 399
- Ricciardelli, E., Cava, A., Varela, J., & Quilis, V. 2014, *MNRAS*, 445, 4045

- Rojas, R. R., Vogeley, M. S., Hoyle, F., & Brinkmann, J. 2004, *ApJ*, 617, 50
- Rojas, R. R., Vogeley, M. S., Hoyle, F., & Brinkmann, J. 2005, *ApJ*, 624, 571
- Rosati, P., Borgani, S., & Norman, C. 2002, *ARA&A*, 40, 539
- Shandarin, S., Feldman, H. A., Heitmann, K., & Habib, S. 2006, *MNRAS*, 367, 1629
- Shandarin, S. F. & Sunyaev, R. A. 2009, *A&A*, 500, 19
- Shandarin, S. F., & Zeldovich, Y. B. 1989, *Reviews of Modern Physics*, 61, 185
- Sheth, R. K., & Diaferio, A. 2011, *MNRAS*, 417, 2938
- Sheth, R. K., Mo, H. J., & Tormen, G. 2001, *MNRAS*, 323, 1
- Sheth, R. K., & van de Weygaert, R. 2004, *MNRAS*, 350, 517
- Sousbie, T., Pichon, C., Colombi, S., Novikov, D., & Pogosyan, D. 2008, *MNRAS*, 383, 1655
- Springel, V., Frenk, C. S., & White, S. D. M. 2006, *Nature*, 440, 1137
- Stoica R. S., Gregori P., Mateu J., 2005, *Stoch. Process. Appl.*, 115,1860
- Stoica, R. S., Martínez, V. J., & Saar, E. 2010, *A&A*, 510, A38
- Sugawara, Y., Takizawa, M., Itahana, M., et al. 2017, *Publications of the Astronomical Society of Japan*, 69, 93
- Sutter, P. M., Lavaux, G., Wandelt, B. D., & Weinberg, D. H. 2012, *ApJ*, 761, 44
- Sylos Labini, F., & Baryshev, Y. V. 2010, *JCAP*, 6, 021
- Tavasoli, S., Rahmani, H., Khosroshahi, H. G., Vasei, K., & Lehnert, M. D. 2015, *ApJ*, 803, L13
- Tegmark, M., Blanton, M. R., Strauss, M. A., et al. 2004, *ApJ*, 606, 702
- Tempel, E., Kipper, R., Saar, E., et al. 2014, *A&A*, 572, A8

- Tempel, E. & Libeskind, N. I. 2013, *ApJ*, 775, L42
- Tempel, E., Stoica, R. S., Kipper, R., & Saar, E. 2016, *Astronomy and Computing*, 16, 17
- Tempel, E., Stoica, R. S. & Saar, E. 2013, *MNRAS*, 428, 1827
- Tittley, E. R., & Henriksen, M. 2001, *ApJ*, 563, 673
- Tully, R. B., Shaya, E. J., Karachentsev, I. D., et al. 2008, *ApJ*, 676, 184-205
- Werner, N., Finoguenov, A., Kaastra, J. S., et al. 2008, *A&A*, 482, L29
- West, M. J., Villumsen, J. V., & Dekel, A. 1991, *ApJ*, 369, 287
- Wray, J. J., Bahcall, N. A., Bode, P., Boettiger, C., & Hopkins, P. F. 2006, *ApJ*, 652, 907
- Yadav, J., Bharadwaj, S., Pandey, B., & Seshadri, T. R. 2005, *MNRAS*, 364, 601
- Zel'dovich, Y. B. 1970, *A&A*, 5, 84
- Zeldovich, I. B., Einasto, J., & Shandarin, S. F. 1982, *Nature*, 300, 407
- Zivick, P., Sutter, P. M., Wandelt, B. D., Li, B., & Lam, T. Y. 2015, *MNRAS*, 451, 4215



## Chapter 2

# Dark Sector Coupling Bends the Superclusters <sup>1</sup>

### 2.1 Introduction

The meticulous analysis of the CMB (Cosmic Microwave Background) temperature power spectrum done by the Planck mission team has casted both light and shadow on the status of the  $\Lambda$ CDM (cosmological constant  $\Lambda$  + cold dark matter) cosmology. While at high multipoles ( $l \geq 500$ ) the  $\Lambda$ CDM cosmology is found perfect in matching the observational data, at low multipoles ( $l \leq 100$ ) its poor-fits has been confirmed not as numerical flukes but likely to be real (Planck Collaboration et al. 2014a,b). Given that the low-multipole behavior of the CMB temperature spectrum reflects the most primordial feature of the universe, the Planck result along with the infamous long-standing problem associated with  $\Lambda$  may imply the incompleteness of the  $\Lambda$ CDM cosmology, encouraging the cosmologists to search more strenuously than ever for physical alternatives.

The coupled dark energy (cDE) models where dark energy is not the inert  $\Lambda$  but a dynamic scalar field coupled to nonbaryonic dark matter particles (Wetterich 1995;

---

<sup>1</sup>The content of this Chapter has been already published as the following journal paper: Shim & Lee (2013, ApJ, 777, 74) whose copyright is held by American Astronomical Society.

Mangano et al. 2003; Amendola 2000, 2004; Macciò et al. 2004; Pettorino & Baccigalupi 2008; Baldi et al. 2010; Wintergerst & Pettorino 2010) have recently attained probing attention because of their capacity for accommodating several observational mysteries that the  $\Lambda$ CDM cosmology could not resolve. For instance, according to Baldi (2012a), the high- $z$  massive clusters regarded as extremely rare events in the  $\Lambda$ CDM universe (e.g., see Jee et al. 2011, and references therein) are more probable to detect in the cDE models. Baldi et al. (2011) demonstrated that the cDE models can explain the observed higher degree of the misalignment between the spatial distributions of cluster galaxies and dark matter than naturally expected in the  $\Lambda$ CDM cosmology (Oguri et al. 2010; Lee 2010). In the work of Lee & Baldi (2012), the morphological properties of the observed bullet cluster (Clowe et al. 2004, 2006; Markevitch et al. 2002, 2004, 2005; Mastropietro & Burkert 2008) that had been found to be in a serious tension with the prediction of the  $\Lambda$ CDM cosmology (Farrar & Rosen 2007; Lee & Komatsu 2010; Thompson & Nagamine 2012; Akahori & Yoshikawa 2012) were much less anomalous in cDE models. Very recently, Salvatelli & Marchini (2013) claimed that the dispute on the value of the Hubble constant between the Planck experiment and the HST (Hubble Space Telescope) project can be ended if cDE is assumed to exist. This capacity of the cDE models to alleviate the tensions posed by the observational anomalies is mainly owing to the presence of an additional long-range fifth force induced by the dark sector coupling (the interaction between dark energy and nonbaryonic dark matter). See Amendola & Tsujikawa (2010) for a comprehensive review of the cDE models.

Since the tight constraints put on the strength of dark sector coupling by the recent observations have sustained as viable only those cDE models which are very hard to distinguish from the  $\Lambda$ CDM cosmology (e.g., Bean et al. 2008), it is necessary to develop as a powerful indicator of cDE as possible for the detection of the effect of cDE on the evolution of the universe. The spatial clustering of galaxy clusters that generates collectively the cosmic web phenomenon (Bond et al. 1996) has been regarded as one of the most powerful indicators of dynamic dark energy. As the dark sector coupling would affect not only the strength of the large-scale clustering but also its degree of

anisotropy, the cosmic web must take on different pattern in the presence of cDE.

The anisotropic clustering of clusters is well manifested by the elongated filamentary shapes of the rich superclusters which correspond to the densest section of the cosmic web. In the literatures which studied the superclusters and their morphological properties, the shapes of the superclusters were measured by various different algorithms such as percolation, ellipsoid-fitting, friends-of-friends, Minkowski functional and etc. (e.g., Dekel et al. 1984; West 1989; Plionis et al. 1992; Jaaniste et al. 1998; Basilakos et al. 2001; Basilakos 2003; Basilakos et al. 2006; Einasto et al. 2007; Wray et al. 2006; Einasto et al. 2011). The general consensus of those previous works was that no matter what algorithm was used, the richer superclusters appear to have more filamentary shapes. Recently, Einasto et al. (2011) noted that the shape of a richest supercluster located in the highly overdense region is best described as a “multi-branch” filament consisting of the main stem and several branches.

Assuming that the degree of the straightness of the supercluster main stems would depend strongly on the dynamics of dark energy, we speculate that in cDE models the main stems of rich superclusters would be less straight, having shorter spatial extents compared with the  $\Lambda$ CDM case, due to the effect of the fifth force. To quantitatively inspect this speculation, we utilize the data from the high-resolution N-body simulations ran for various cDE models as well as for the  $\Lambda$ CDM model. The upcoming chapters are organized as follows: In section 2, we briefly review the cDE scenarios and describe how the spatial extents of the superclusters found in the N-body data are determined. In section 3, we show how the degree of the supercluster straightness depends on the strength of dark sector coupling and how the difference in the supercluster straightness between the cDE and the  $\Lambda$ CDM cases changes with redshifts. In section 5, we summarize the key results and draw a final conclusion.

## 2.2 Numerical Data and Analysis

### 2.2.1 A Brief Summary of the CODECS

The CODECS stands for the COupled Dark Energy Cosmological Simulations performed by Baldi (2012b) for several different cDE models as well as for the standard  $\Lambda$ CDM model with  $1024^3$  CDM particles and the same number of baryon particles in a periodic box of linear size  $1 h^{-1}\text{Gpc}$ . The CODECS has the mass-resolution of  $m_c = 5.84 \times 10^{10} h^{-1} M_\odot$  and  $m_b = 1.17 \times 10^{10} h^{-1} M_\odot$  where  $m_c$  and  $m_b$  represent the mass of each CDM and baryon particle at the present epoch, respectively. As conventionally done, a bound dark halo was identified in the CODECS suite as a friends-of-friends (FoF) group in which the component particles are all within the linking length of  $0.2\bar{l}$  where  $\bar{l}$  is the mean particle separation (Davis et al. 1985). In the CODECS project the initial conditions of all models were set to be consistent with the WMAP7 values (Komatsu et al. 2011). For the cDE models the normalization amplitude of the density power spectrum,  $\sigma_8$ , has the same value as the  $\Lambda$ CDM case at the moment of the last-scattering, while the other key parameters have the WMAP7 values at  $z = 0$ . For a full description of the CODECS, see Baldi (2012b).

Among several target cDE models of the CODECS, the following four models are considered for our analysis: EXP002, EXP003, EXP008e3 and SUGRA003. In the first two models (EXP002 and EXP003) where the dynamics of a scalar field cDE,  $\phi$ , is governed by an exponential potential of  $U(\phi) \propto \exp(-\alpha\phi)$  with  $\alpha = 0.08$  (Lucchin & Matarrese 1985; Ratra & Peebles 1988; Wetterich 1988), the coupling parameter  $\beta$  that quantifies the strength of the dark sector coupling has a positive constant value of 0.1 and 0.15, respectively. In the third model (EXP008e3) where the cDE potential has the same exponential shape, the coupling strength is no longer a constant but depends exponentially on  $\phi$  as  $\beta = 0.4 \exp(3\phi)$ . In the fourth model (SUGRA003) where the cDE evolves according to the supergravity potential of  $U(\phi) \propto \phi^{-\alpha} \exp(\phi^2/2)$  (Brax & Martin 1999),  $\beta$  has a negative constant value of  $-0.15$  (Baldi 2012a). The amplitudes of the linear density power spectrum at  $z = 0$  have the values of  $\sigma_8 =$

0.875, 0.967, 0.895 and 0.806 at  $z = 0$  for the EXP002, EXP003, EXP008e3 and SUGRA003 models, respectively. For comparison, we also consider the  $\Lambda$ CDM model included in the CODECS project for which  $\sigma_8 = 0.809$ . For a detailed explanation of the cDE models considered in the CODECS, see Baldi (2012b).

### 2.2.2 Identifying the Supercluster Spines

From the dark halo catalogs from the CODECS at  $z = 0$ , we first select only those cluster halos whose masses  $M$  satisfy the condition of  $M \geq 10^{13} h^{-1} M_\odot$  for each model. Following the conventional scheme (e.g., Kasun & Evrard 2005; Lee 2006; Wray et al. 2006; Lee & Komatsu 2010), we identify the superclusters as the FoF groups of the closely located clusters among the selected ones within the linking length,  $l$ , equal to one third of the mean separation of the selected clusters,  $\bar{d}_c$ , as  $l = \bar{d}_c/3$ . Figure 2.1 plots the number densities of the selected clusters and the identified superclusters per unit volume for five cosmological models at  $z = 0$  in the top and bottom panels, respectively. As can be seen, the selected clusters of each model exhibit a different mass spectrum. This result indicates that the selected clusters of each model has a different mean separation  $\bar{d}_c$ , which has been in fact properly taken into account when the superclusters are identified as FoF groups of the linked clusters within the distance of  $l$ . Note that the massive clusters and superclusters are most abundant in the EXP003 model, while the SUGRA003 model displays almost the same mass distributions as the  $\Lambda$ CDM case.

Choosing only those rich superclusters which have three or more member clusters, we apply the minimal spanning tree (MST) technique to dig out their filamentary patterns for each cosmological model. It was Barrow et al. (1985) who for the first time used the MST algorithm to study systematically the local galaxy distribution. Afterwards, the MST algorithm has been refined and modified by several authors to investigate the geometrical properties of the large scale structure with it (e.g., Krzewina & Saslaw 1996; Doroshkevich et al. 2001; Colberg 2007; Park & Lee 2009).

It may be worth explaining here why we choose the MST algorithm for our anal-

ysis rather than more recently developed algorithms such as the Skeleton (Sousbie et al. 2008), the Multiscale Morphology Filter (Aragón-Calvo et al. 2010), the NEXUS (Cautun et al. 2013), and so forth, all of which are believed to be more accurate and efficient in tracing the cosmic web. The number one reason is that the application of those more recent and more elaborate algorithms require us to know the underlying dark matter distribution (or density/velocity fields) unlike the MST algorithm for which only the halo distributions are necessary. Given that the dark matter distribution from the CODECS is not publicly available, we had to find an algorithm based only on the halo distributions. Of course, it is still possible in principle to reconstruct the density/velocity fields from the CODECS halo catalogs and then to apply those more improved algorithms to the reconstructed density/velocity fields. But, our ultimate goal is not to model as accurately as possible the supercluster shapes but to see if and how the supercluster straightness depends on the background cosmology. Thus, we believe that the reconstruction of the density fields of all five models is beyond the scope of this paper. In fact, the MST which treats each member cluster as a point (node) without weighing it by its mass must be the most optimal (and the most practical) algorithm to achieve our goal since we would like to separate the cosmology dependence of the supercluster straightness from that of the supercluster mass which is anyway hard to estimate accurately in real observation.

After constructing the MST of each supercluster, we extract its main stem by pruning off its minor branches, under the assumption that the main stem of a supercluster MST corresponds to its most prominent filamentary part. Since we confine the MST reconstruction procedure to the member cluster distribution inside each supercluster, we only prune a supercluster MST without separating it into smaller filamentary parts (c.f., Barrow et al. 1985; Colberg 2007; Park & Lee 2009). Figure 2.2 illustrates in the two-dimensional projected space how the main stem of a supercluster MST is determined through pruning process at  $z = 0$  for the  $\Lambda$ CDM model, displaying how the minor branches are repeatedly cleared off from the main stem of a supercluster MST. As Colberg (2007) called the main stem of a MST out of the galaxy distribution as

the "backbone of the large-scale structure", hereafter we also call the main stem of a supercluster *the supercluster spine*. Figure 2.3 plots the number distribution of the member clusters of those rich supercluster spines consisting of three or more nodes for the five models at  $z = 0$ . As can be seen, the distributions of the node numbers ( $N_{\text{node}}$ ) of the supercluster spines for the five models are very similar to one another except for the numerical fluctuations in the large- $N_{\text{node}}$  section, even though each model has a different mass distribution (see Figure 2.1).

An acute reader might concern about a possibility that in case of a more or less spherically shaped supercluster the pruning process would remove its most massive member from the main stem. We have investigated how probable this case is for each model and found that the fraction of all supercluster MSTs occupied by those cases is less than 0.03 for every model, having very negligible effect on the final result. Table 2.1 lists the numbers of those rich superclusters whose spines consist of three or more nodes and the percentage of the supercluster spines from which the most massive member clusters are pruned away at  $z = 0$  for the five models. Figure 2.4 plots the mean specific mass,  $\langle \tilde{M}_{\text{spine}} \rangle \equiv \langle M_{\text{spine}}/N_{\text{node}} \rangle$ , of the rich supercluster spines vs. the cosmological model. As can be seen, the mean specific mass is the highest for the EXP003 case, indicating that the superclusters tend to have higher masses when the amplitude of the density power spectrum,  $\sigma_8$ , has a higher value.

### 2.3 Supercluster Straightness as a Probe of cDE

Using only those rich superclusters whose spines consist of three or more nodes, we determine their sizes,  $S$ . Although a detailed explanation about how to measure the size of a pruned MST is provided in Park & Lee (2009) (see also, Colberg 2007), we also briefly describe here the procedure to estimate the size of each supercluster spine to make this paper self-contained. Let the comoving Cartesian coordinates of all nodes belonging to a supercluster spine be in range of  $x_{\text{min}} \leq x \leq x_{\text{max}}$ ,  $y_{\text{min}} \leq y \leq y_{\text{max}}$ ,  $z_{\text{min}} \leq z \leq z_{\text{max}}$ , respectively. The size,  $S$ , of a supercluster spine is now estimated as  $S = [(x_{\text{max}} - x_{\text{min}})^2 + (y_{\text{max}} - y_{\text{min}})^2 + (z_{\text{max}} - z_{\text{min}})^2]^{1/2}$ , which quantifies

effectively how extended the supercluster spine is in the three dimensional space. Figure 2.5 illustrates how the size  $S$  of a supercluster spine is measured at  $z = 0$  for the  $\Lambda$ CDM case in the two-dimensional projected space.

Obviously the size of a supercluster spine increases with the number of nodes. When the number of nodes  $N_{\text{node}}$  is fixed, however, the more straight superclusters should have larger sizes. To quantify its degree of the straightness of a supercluster spine, we define the specific size  $\tilde{S}$  as the size per node,  $\tilde{S} \equiv S/N_{\text{node}}$ . Figure 2.6 shows the projected images of three randomly chosen supercluster spines with three different specific sizes at  $z = 0$  for the  $\Lambda$ CDM case. As can be seen, those supercluster spines with larger specific sizes look more straight, demonstrating that the specific size of a supercluster spine is an effective indicator of its straightness.

Now, we estimate the mean value of  $\tilde{S}$  averaged over those superclusters whose spines have  $N_{\text{node}} \geq 3$  for each cosmological model. Figure 2.7 plots the mean specific sizes,  $\langle \tilde{S} \rangle$ , versus the five cosmological models at  $z = 0$ . The errors  $\sigma_{\tilde{S}}$  are calculated as the one standard deviation in the measurement of the mean value  $\sigma_{\tilde{S}} = [(\langle \tilde{S}^2 \rangle - \langle \tilde{S} \rangle^2)/(N_{\text{spine}} - 1)]^{1/2}$ . As can be seen, in the cDE models the supercluster spines tend to have smaller specific sizes. In other words, the superclusters in models with cDE are less straight. The  $\Lambda$ CDM case exhibits the highest value of  $\tilde{S}$  while the lowest value is found for the SUGRA003 case. As can be seen, the difference in  $\tilde{S}$  between the  $\Lambda$ CDM and the SUGRA003 cases is the most significant (see also, Lee (2012)). There is a clear trend that the mean value of  $\tilde{S}$  decreases with increasing coupling strength for the cases that cDE has a constant coupling (EXP002 and EXP003) while the EXP008e3 case does not show a significant difference in  $\langle \tilde{S} \rangle$  from the  $\Lambda$ CDM case.

It is important to note that the cosmology dependence of  $\langle \tilde{S} \rangle$  is obviously different from that of  $\langle \tilde{M}_{\text{spine}} \rangle$  by comparing the result shown in Figure 2.4 with that in Figure 2.7. The mean specific mass of the supercluster spines in the SUGRA003 model turns out to be very similar to the  $\Lambda$ CDM case, while the two models show significant difference in the mean specific size of the supercluster spines. This result implies that the difference in the supercluster mass existent among the models should not be the cause

of the detected overall trend between the cDE models and the mean specific sizes of the supercluster spines.

The result shown in Figure 2.7 reveals that the dark sector coupling plays a role in diminishing the degree of the straightness of the superclusters. Our interpretation is as follows: The accelerating expansion of the Universe caused by the anti-gravitational action of dark energy sharpens the cosmic web while the gravitational clustering of clusters tends to blunt it since the former (latter) increases the relative dominance of the anisotropic (isotropic) stress on the supercluster scales. The competition between the two driving forces determines the degree of the straightness of the superclusters which reflects how sharp the cosmic web is in the universe. In the cDE models, the additional attractive fifth force with long range helps gravity blunt the cosmic web on the large scale, reducing the specific sizes of the supercluster spines, which is why the stronger dark sector coupling makes the supercluster spines less straight.

The lowest value of  $\langle \tilde{S} \rangle$  found for the SUGRA003 case may be also interpreted as follows. The degree of the supercluster straightness is also affected by the peculiar velocity perturbation. The large peculiar velocity perturbation tends to sharpen the cosmic web. A good analogy can be found in a warm dark matter (WDM) model where the peculiar velocity perturbation of DM particles is much larger than for the CDM case. Gao & Theuns (2007) clearly demonstrated by using a high-resolution hydrodynamic simulation that a WDM model produces a sharper cosmic web due to its larger velocity perturbation.

Given this analogy, one can expect that in the cDE models with smaller velocity perturbation the superclusters must become less straight. As shown in Baldi (2012b) and Lee & Baldi (2012), the velocity perturbation of the SUGRA003 model is as large as that of the EXP003 case before  $z \sim 7$  but suddenly changes its tendency, dropping rapidly below that of the  $\Lambda$ CDM model at lower redshifts (see Figure 7 in Lee & Baldi 2012). Therefore, at present epoch the velocity perturbation in the SUGRA003 model is even smaller than that of the  $\Lambda$ CDM case, which leads to blunt the cosmic web and to diminish the degree of the straightness of the supercluster spines. As for

the EXP002 and EXP003 model with constant coupling, the interplay between the dark sector coupling and the larger velocity perturbation determines the decrement in the degree of the supercluster straightness: The presence of the dark sector coupling tends to undermine the degree of the supercluster straightness while the large velocity perturbation relative to the  $\Lambda$ CDM case plays a role in straightening the superclusters. Our result shown in Figure 2.7 indicates that the former effect should be more dominant.

To investigate how the supercluster straightness evolves for each model, we repeat the whole process at three higher redshifts:  $z = 0.19, 0.35, 0.55$ . Figure 2.8 plots the mean specific sizes of the supercluster spines as a function of  $z$  for five different models. As can be seen, for all of the five cosmological models, the specific sizes of the supercluster spines increase with redshifts. It can be well understood by the fact that at higher redshifts the superclusters obtained as FoF groups from the mass-limited cluster sample (with the same mass threshold of  $10^{13} h^{-1} M_{\odot}$ ) correspond to more linear regimes where the clustering of clusters is not so strong.

As can be also seen in Figure 2.8, at all redshifts, the  $\Lambda$ CDM case is found to have the largest mean specific sizes of the supercluster spines. The strongest evolution in  $\langle \tilde{S} \rangle$  is found for the SUGRA003 case, while the EXP003 shows the weakest evolution. It is also interesting to see that at higher redshifts the EXP008e3 case differs significantly in  $\langle \tilde{S} \rangle$  from the  $\Lambda$ CDM case. As shown in Lee & Baldi (2012), the velocity perturbation in the EXP008e3 model increases exponentially relative to the  $\Lambda$ CDM case at lower redshifts. Therefore, the significant difference in  $\langle \tilde{S} \rangle$  between the EXP008e3 and the  $\Lambda$ CDM case at high redshifts must be due to the smaller velocity perturbation of the EXP008e3 at higher redshifts than at the present epoch, which is consistent with our interpretation that the larger (smaller) velocity perturbation functions for (against) sharpening the cosmic web.

The result shown in 2.8 also shows that at higher redshifts the differences in  $\langle \tilde{S} \rangle$  between the cDE and the  $\Lambda$ CDM cases become more significant. As mentioned in the above, the high- $z$  superclusters are more linear objects and thus they are more vulnerable to the long-range fifth force in cDE models. The crucial implication of this

result is that the redshift evolution of  $\langle \tilde{S} \rangle$  must be a powerful complimentary probe of cDE.

## 2.4 Summary and Discussion

Although the dependence of the 'filamentarity' of the rich superclusters on the initial conditions of the Universe was already noted by several authors, (e.g., Dekel et al. 1984; Kolokotronis et al. 2002; Lesgourgues & Pastor 2006), the supercluster shape distribution was not seriously considered as an efficient cosmological probe mainly because the rich filament-like superclusters were regarded too rare to provide good-number statistics. However, the recently available large datasets from the full sky galaxy surveys and the high-resolution simulations have allowed us to explore systematically what a new window the noticeable filamentary shapes of the rich supercluster can open on the early universe.

In this paper we have investigated how the presence of the dark sector coupling in cDE models changes the intrinsic clustering pattern of the clusters in the supercluster environments by utilizing the group catalogs from the CODECS. To single out the effect of the dark sector coupling on the clustering of supercluster clusters from the nonlinear growth of the large-scale density field, instead of dealing with the overall filamentary shapes of the superclusters, we focus only on the straightness of the main stems (i.e., spines) of the minimal spanning trees constructed out of the supercluster clusters. The degree of the straightness of a supercluster has been quantified by the specific size of its spine (spatial extent of the spine per member cluster). It has been finally shown that the stronger dark sector coupling makes the superclusters less straight and that in the presence of cDE governed by the supergravity potential (Brax & Martin 1999) the superclusters are least straight. The difference in the mean specific size of the supercluster spines between the  $\Lambda$ CDM and the viable cDE models has been found to become more significant at higher redshifts.

Our results have been physically explained as follows. The attractive fifth force in the cDE models helps the large-scale gravitational clustering blunt the cosmic web

while the anti-gravitational action of dark energy sharpens it. Since the supercluster straightness depends on how sharp the cosmic web is, the cDE models have less straight superclusters than the  $\Lambda$ CDM case. The degree of the supercluster straightness also depends on the peculiar velocity perturbation of clusters. The large peculiar velocity perturbation of clusters functions against blunting the cosmic web, contributing to the degree of the supercluster straightness. At higher redshifts, the superclusters for both of the cDE and the  $\Lambda$ CDM models are more straight since they correspond to more linear regimes where the isotropic stress is less dominant. The sharp increase of the supercluster straightness with redshifts found in the supergravity model is closely related to the bouncing behavior of dark energy equation of state in the supergravity model (Baldi 2012b). Finally, we conclude that the redshift evolution of the supercluster straightness should in principle become a complimentary new test of cDE.

For a practical test of cDE with the evolution of the supercluster straightness, however, it will be necessary to deal with the superclusters identified not in real space but in redshift space. If the host superclusters are elongated along the line-of-sight directions, the cluster bulk motions along the supercluster major axes would cause significant uncertainty on the measurements of the supercluster sizes. Furthermore, the effect of the redshift distortion caused by the cluster bulk motion on the supercluster straightness is likely related to the strength of dark sector coupling since in the cDE models the cluster bulk motions must be more active (e.g., Lee & Baldi 2012). It will be definitely important to account for the redshift distortion effect on the supercluster straightness and to examine how strongly the effect depends on the strength of dark sector coupling.

The other thing that it will be worth exploring is the robustness of our result against the algorithm to identify the filamentary structures in the cosmic web. In the current work, the MST algorithm has been exclusively utilized to determine the most prominent filamentary part of the richest section of the cosmic web. But, as mentioned in section 2, there exist several more recently developed algorithms which are expected to trace more rigorously the linear patterns of the cosmic web on the scales beyond the

superclusters (Sousbie et al. 2008; Aragón-Calvo et al. 2010; Cautun et al. 2013). If a consistent result be drawn even with a different algorithm, it would confirm strongly the usefulness of the supercluster straightness as a probe of coupled dark energy. Our future work is in this direction.

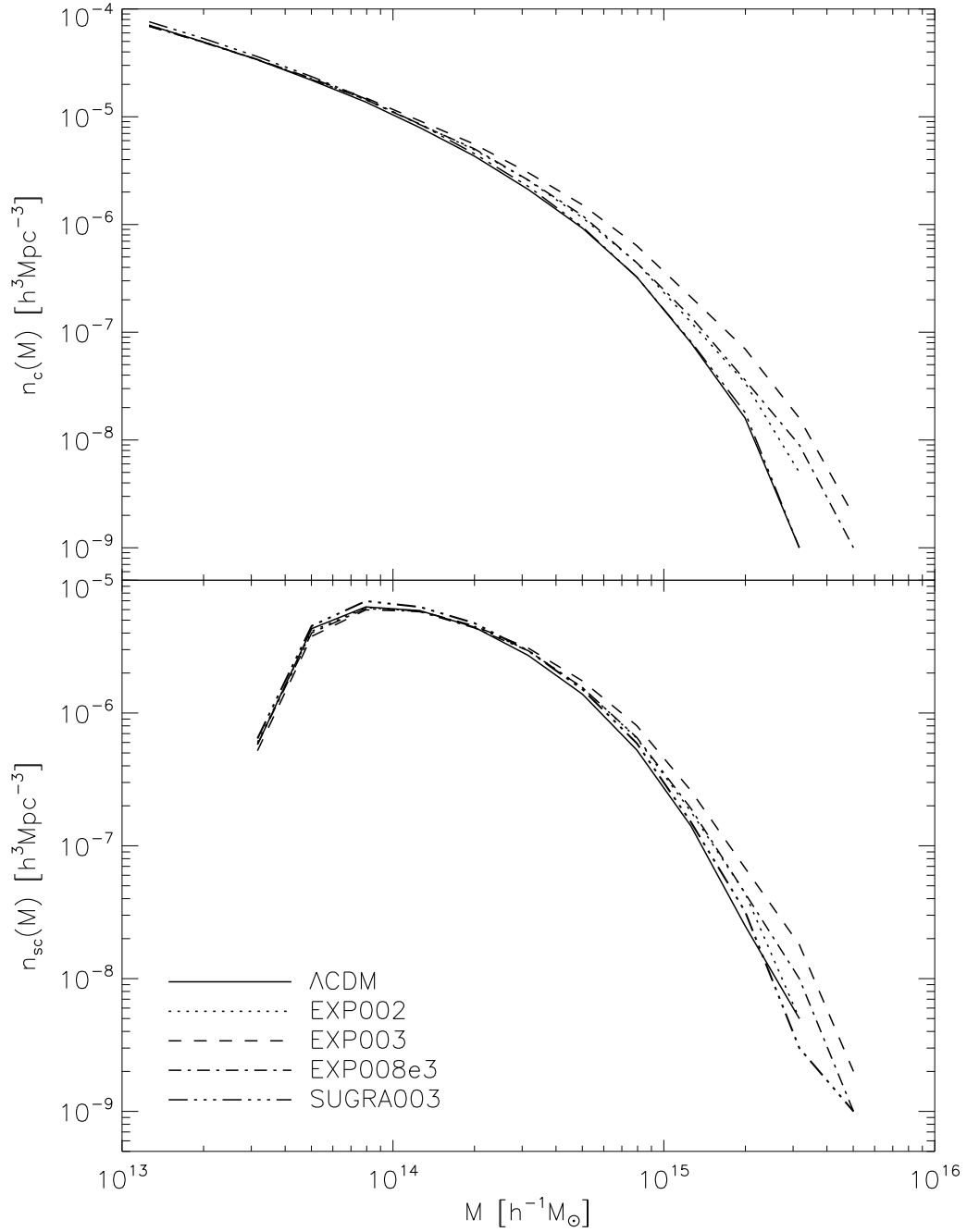


**Figure 2.1.** Number densities of the selected cluster halos (top panel) and the superclusters identified as the FoF groups of the selected cluster halos with linkage parameter of 1/3 (bottom panel) per unit volume at  $z = 0$  for five different cosmological models from the CODECS.

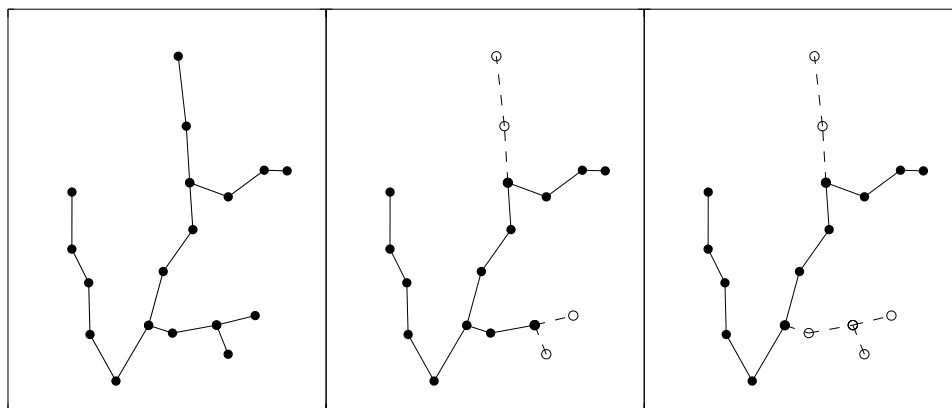


**Figure 2.2.** Illustration of the pruning process of a supercluster with 18 nodes identified in the CODECS group catalog at  $z = 0$  in the two dimensional plane. All the branches composed of two or less nodes are regarded as not a part of the main stem and thus cut down by the pruning process.

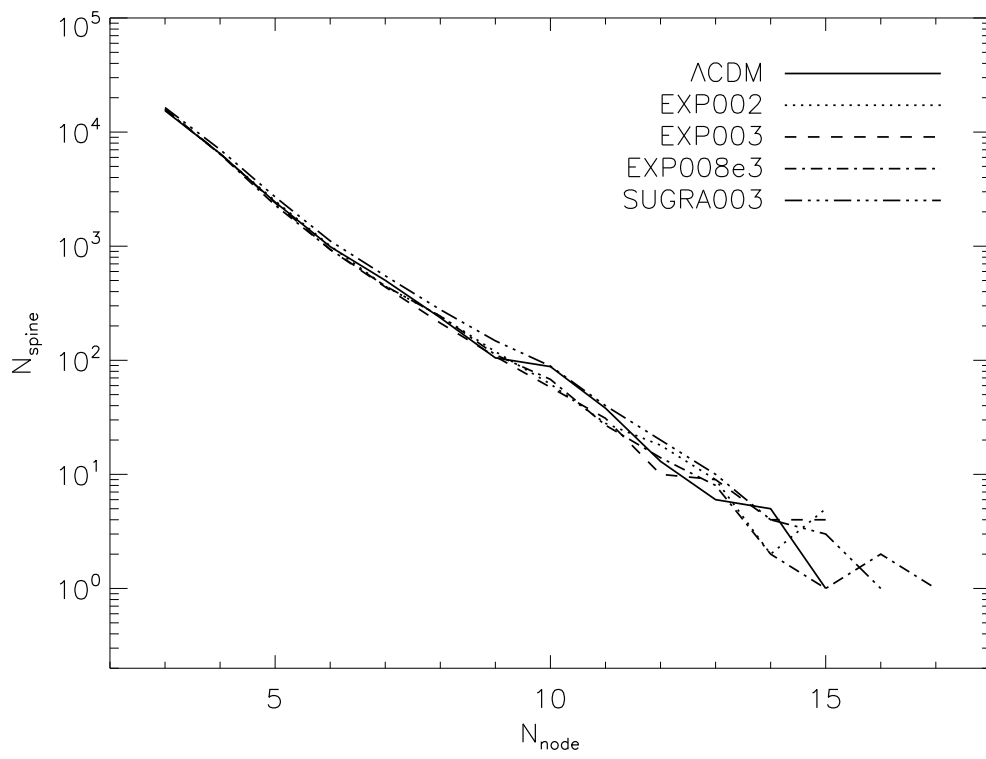


**Figure 2.3.** Node number distributions of the supercluster spines for five different models at  $z = 0$ .

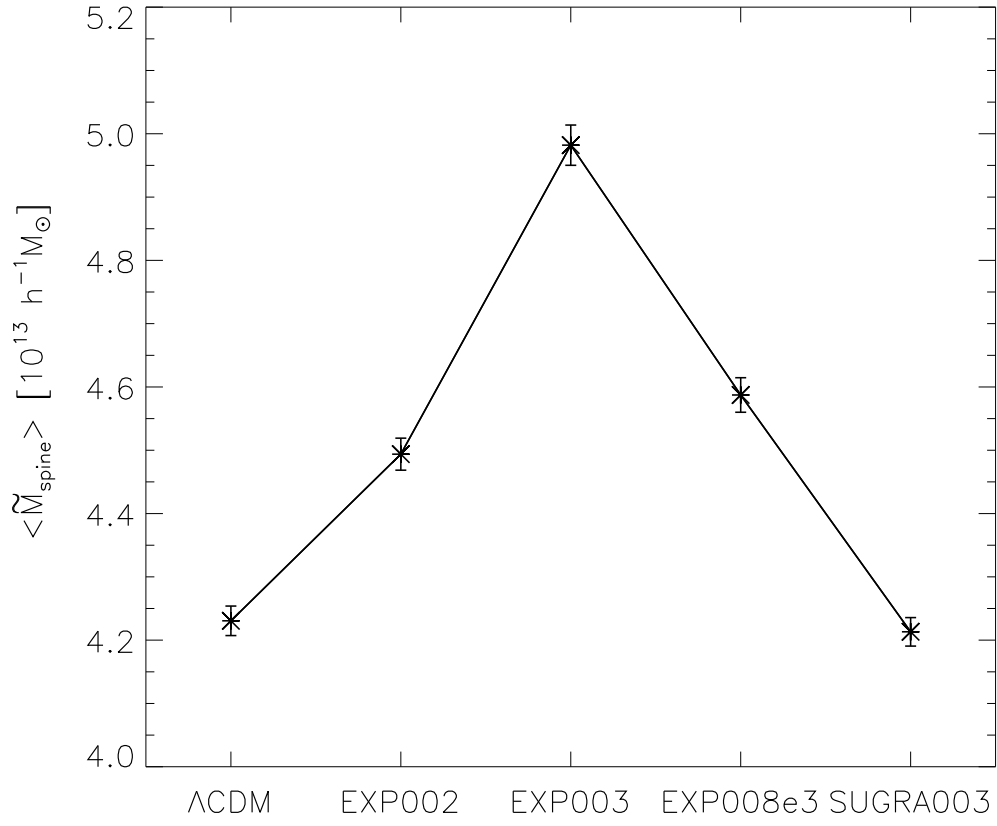


**Figure 2.4.** Mean specific masses of the supercluster spines at  $z = 0$  vs. the cosmological models.



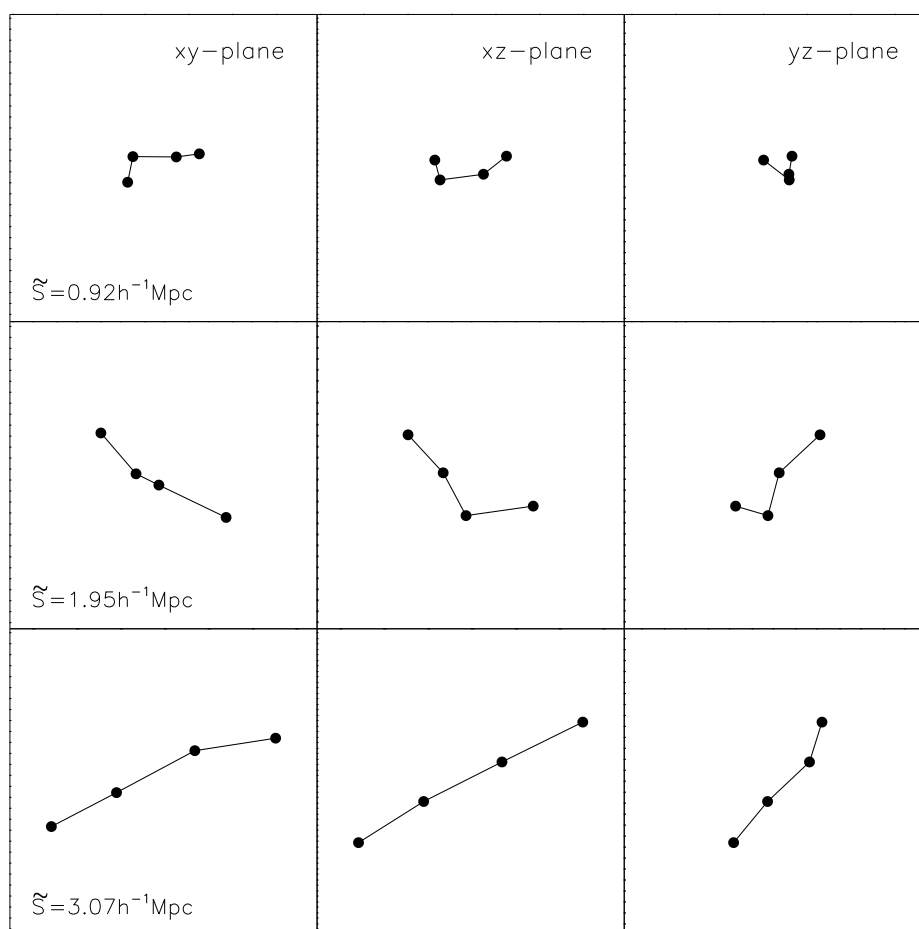


**Figure 2.6.** Projected images of three randomly chosen supercluster spines having same number of nodes but different specific sizes from the  $\Lambda$ CDM case at  $z = 0$ .

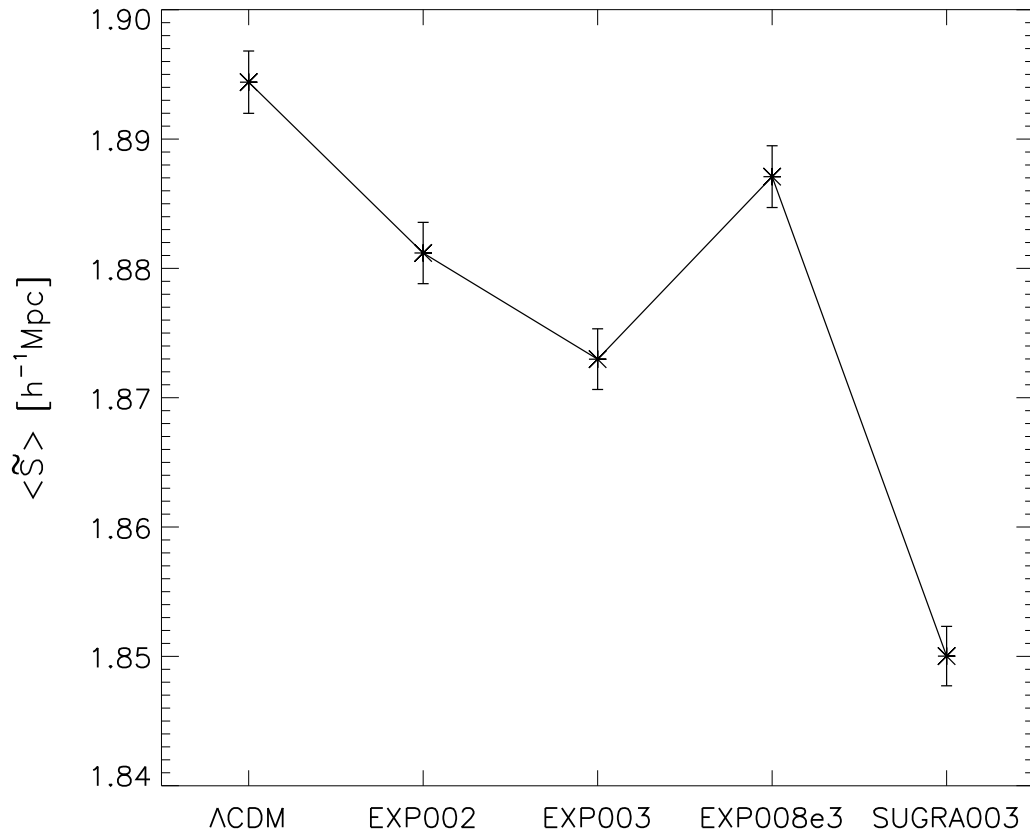


**Figure 2.7.** Mean specific sizes of the supercluster spines for the five models at  $z = 0$ .

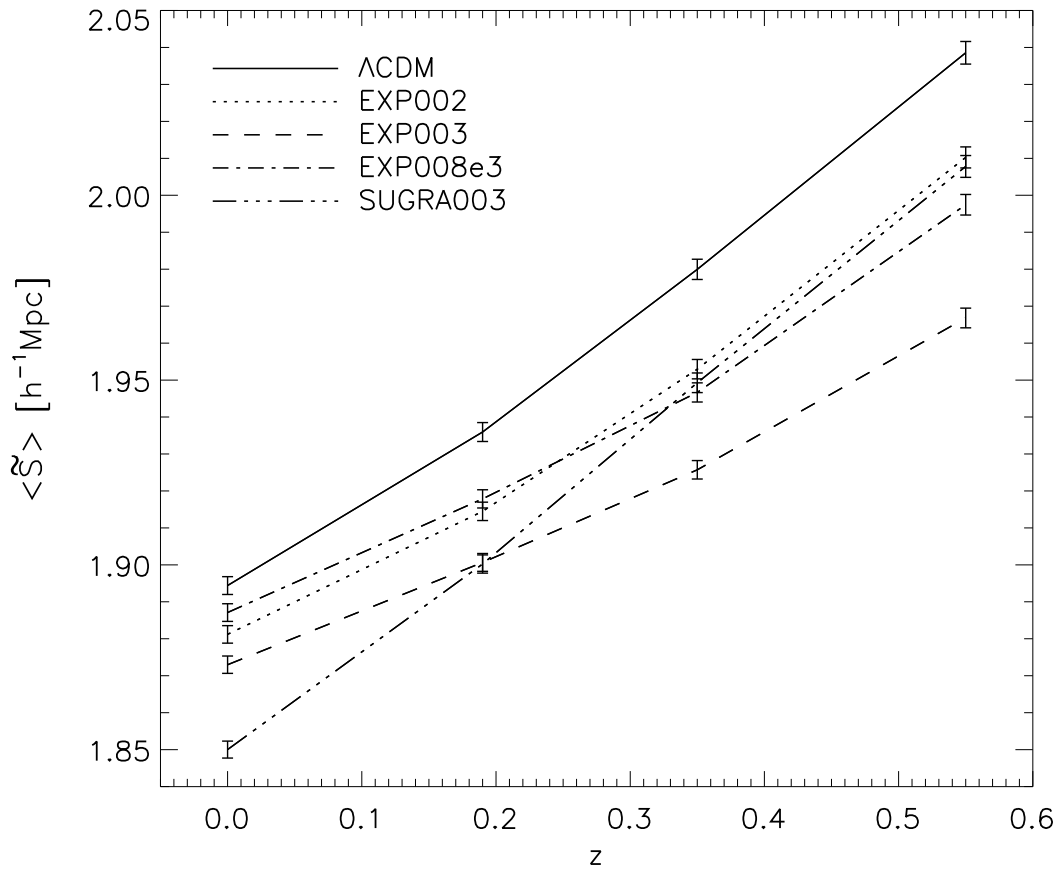


**Figure 2.8.** Redshift evolution of the mean specific sizes of the supercluster spines for the five models.

Table 2.1. Numbers of those supercluster spines with three or more nodes and the fraction occupied by those spines from which the most massive clusters are pruned away.

model	$N_{\text{spine}}$	fraction [%]
$\Lambda$ CDM	26311	2.79
EXP002	26678	2.59
EXP003	26636	2.32
EXP008e3	26259	2.51
SUGRA003	28400	2.82

# Bibliography

- Akahori, T., & Yoshikawa, K. 2012, PASJ, 64, 12
- Amendola, L. 2000, Phys. Rev. D, 62, 043511
- Amendola, L. 2004, Phys. Rev. D, 69, 103524
- Amendola, L. & Tsujikawa, S. 2010, Dark Energy (Cambridge University Press:Cambridge)
- Aragón-Calvo, M. A., van de Weygaert, R., & Jones, B. J. T. 2010, MNRAS, 408, 2163
- Baldi, M., & Viel, M. 2010, MNRAS, 409, L89
- Baldi, M., Pettorino, V., Robbers, G., & Springel, V. 2010, MNRAS, 403, 1684
- Baldi, M., & Pettorino, V. 2011, MNRAS, 412, L1
- Baldi, M., Lee, J., & Macciò, A. V. 2011, ApJ, 732, 112
- Baldi, M. 2011a, MNRAS, 411, 1077
- Baldi, M. 2011b, MNRAS, 414, 116
- Baldi, M. 2012, MNRAS, 420, 430
- Baldi, M. 2012, MNRAS, 422, 1028
- Barrow, J. D., Bhavsar, S. P., & Sonoda, D. H. 1985, MNRAS, 216, 17
- Basilakos, S., Plionis, M., & Rowan-Robinson, M. 2001, MNRAS, 323, 47

- Basilakos, S. 2003, MNRAS, 344, 602
- Basilakos, S., Plionis, M., Yepes, G., Gottlöber, S., & Turchaninov, V. 2006, MNRAS, 365, 539
- Bean, R., Flanagan, É. É., Laszlo, I., & Trodden, M. 2008, Phys. Rev. D, 78, 123514
- Benson, A. J. 2005, MNRAS, 358, 551
- Bond, J. R., Kofman, L., & Pogosyan, D. 1996, Nature, 380, 603
- Brax, P. H., & Martin, J. 1999, Physics Letters B, 468, 40
- Cautun, M., van de Weygaert, R., & Jones, B. J. T. 2013, MNRAS, 429, 1286
- Clowe, D., Gonzalez, A., & Markevitch, M. 2004, ApJ, 604, 596
- Clowe, D., Bradač, M., Gonzalez, A. H., Markevitch, M., Randall, S. W., Jones, C., & Zaritsky, D. 2006, ApJ, 648, L109
- Colberg, J. M. 2007, MNRAS, 375, 337
- Davis, M., Efstathiou, G., Frenk, C. S., & White, S. D. M. 1985, ApJ, 292, 371
- Dekel, A., West, M. J., & Aarseth, S. J. 1984, ApJ, 279, 1
- Doroshkevich, A. G., Tucker, D. L., Fong, R., Turchaninov, V., & Lin, H. 2001, MNRAS, 322, 369
- Einasto, M., Saar, E., Liivamägi, L. J., et al. 2007, A&A, 476, 697
- Einasto, M., Liivamägi, L. J., Tago, E., et al. 2011, A&A, 532, A5
- Farrar, G. R., & Rosen, R. A. 2007, Physical Review Letters, 98, 171302
- Gao, L., & Theuns, T. 2007, Science, 317, 1527
- Jaaniste, J., Tago, E., Einasto, M., et al. 1998, A&A, 336, 35
- Jee, M. J., Dawson, K. S., Hoekstra, H., et al. 2011, ApJ, 737, 59

- Ho, S., Bahcall, N., & Bode, P. 2006, *ApJ*, 647, 8
- Kasun, S. F., & Evrard, A. E. 2005, *ApJ*, 629, 781
- Kolokotronis, V., Basilakos, S., & Plionis, M. 2002, *MNRAS*, 331, 1020
- Komatsu, E., et al. 2011, *ApJS*, 192, 18
- Krzewina, L. G., & Saslaw, W. C. 1996, *MNRAS*, 278, 869
- Lee, J. 2006, *ApJ*, 643, 724
- Lee, J., & Park, D. 2006, *ApJ*, 652, 1
- Lee, J., & Park, D. 2009, *ApJ*, 696, L10
- Lee, J., Hahn, O., & Porciani, C. 2009, *ApJ*, 705, 1469
- Lee, J., & Komatsu, E. 2010, *ApJ*, 718, 60
- Lee, J. 2010, arXiv:1008.4620
- Lee, J., & Baldi, M. 2012, *ApJ*, 747, 45
- Lee, J. 2012, *ApJ*, 751, 153
- Lim, S., & Lee, J. 2014, *ApJ*, 783, 39
- Lucchin, F., & Matarrese, S. 1985, *Phys. Rev. D*, 32, 1316
- Macciò, A. V., Quercellini, C., Mainini, R., Amendola, L., & Bonometto, S. A. 2004, *Phys. Rev. D*, 69, 123516
- Mainini, R., & Bonometto, S. 2006, *Phys. Rev. D*, 74, 043504
- Mangano, G., Miele, G., & Pettorino, V. 2003, *Modern Physics Letters A*, 18, 831
- Markevitch, M., Gonzalez, A. H., David, L., Vikhlinin, A., Murray, S., Forman, W., Jones, C., & Tucker, W. 2002, *ApJ*, 567, L27

- Markevitch, M., Gonzalez, A. H., Clowe, D., Vikhlinin, A., Forman, W., Jones, C., Murray, S., & Tucker, W. 2004, *ApJ*, 606, 819
- Markevitch, M., Govoni, F., Brunetti, G., & Jerius, D. 2005, *ApJ*, 627, 733
- Mastropietro, C., & Burkert, A. 2008, *MNRAS*, 389, 967
- Oguri, M., Takahashi, K., Ichiki, K., & Ohno, H. 2004, arXiv:astro-ph/0410145
- Oguri, M., Takada, M., Okabe, N., & Smith, G. P. 2010, *MNRAS*, 405, 2215
- Park, D., & Lee, J. 2007, *Physical Review Letters*, 98, 081301
- Park, D., & Lee, J. 2009, *MNRAS*, 397, 2163
- Pettorino, V., & Baccigalupi, C. 2008, *Phys. Rev. D*, 77, 103003
- Plionis, M., Valdarnini, R., & Jing, Y.-P. 1992, *ApJ*, 398, 12
- Planck Collaboration, Ade, P. A. R., Aghanim, N., et al. 2014, *A&A*, 571, A16
- Planck Collaboration, Ade, P. A. R., Aghanim, N., et al. 2014, *A&A*, 571, A15
- Ratra, B., & Peebles, P. J. E. 1988, *Phys. Rev. D*, 37, 3406
- Salvatelli, V., Marchini, A., Lopez-Honorez, L., & Mena, O. 2013, *Phys. Rev. D*, 88, 023531
- Sousbie, T., Pichon, C., Colombi, S., Novikov, D., & Pogosyan, D. 2008, *MNRAS*, 383, 1655
- Springel, V., & Farrar, G. R. 2007, *MNRAS*, 380, 911
- Thompson, R., & Nagamine, K. 2012, *MNRAS*, 419, 3560
- Wen, Z. L., Han, J. L., & Liu, F. S. 2010, *MNRAS*, 407, 533
- West, M. J. 1989, *ApJ*, 347, 610
- Wetterich, C. 1988, *Nuclear Physics B*, 302, 668

Wetterich, C. 1995, *A&A*, 301, 321

Wintergerst, N., & Pettorino, V. 2010, *Phys. Rev. D*, 82, 103516

Wray, J. J., Bahcall, N. A., Bode, P., Boettiger, C., & Hopkins, P. F. 2006, *ApJ*, 652, 907



## Chapter 3

# Massive Gravity Wrapped in the Cosmic Web <sup>1</sup>

### 3.1 Introduction

The deepest and the most profound question in modern cosmology is what caused the universe to accelerate at the present epoch. Although the Planck mission team recently confirmed the stunning agreements between the predictions of the standard  $\Lambda$ CDM (cosmological constant  $\Lambda$  + cold dark matter) model and the CMB temperature power spectrum measured with unprecedentedly high precision (Planck collaboration XV 2013; Planck Collaboration XVI 2013), the notorious fine tuning problem of  $\Lambda$  still haunts the cosmologists to vigorously look for alternative models. There have been two main directions in developing viable alternatives. One direction is to replace  $\Lambda$  with some dynamic dark energy with negative pressure that could induce the current acceleration of the universe without requiring fine tuned conditions (see Amendola & Tsujikawa 2010, for a comprehensive review). Among various dynamic dark energy scenarios, the coupled dark energy (cDE) model where a scalar field dark energy interacts with dark matter has been found quite promising because of its capacity of alleviating

---

<sup>1</sup>The content of this Chapter has been already published as the following journal paper: Shim et al. (2014, ApJ, 784, 84) whose copyright is held by American Astronomical Society.

several reported tensions between the  $\Lambda$ CDM model and the observations (e.g., Baldi et al. 2011; Baldi 2012a; Lee & Baldi 2012; Salvatelli & Marchini 2013).

The other main direction is to modify the general relativity (GR) on the large scale, which makes the concept of anti-gravitational dark energy unnecessary to explain the observed distance-luminosity relation of Type Ia supernovae (see Clifton et al. 2012, for a comprehensive review). The tremendous success of GR on the local scale, however, leaves only very little room for possible deviation of true gravity from GR. The  $f(R)$  gravity is one of those few modified gravity models which has so far survived severe cosmological tests (Reyes et al. 2010; Wojtak et al. 2011). In this model,  $f(R)$  represents an arbitrary function of the Ricci scalar  $R$  that is substituted for  $R$  in the Einstein- Hilbert action, and the derivative,  $df/dR$ , induces a fifth force on the large scale, the strength of which is quantified by its absolute magnitude at the present epoch,  $f_{R0} \equiv |df/dR|_0$  (Sotiriou & Faraoni 2010; de Felice & Tsujikawa 2010). An essential feature of the  $f(R)$  gravity is the presence of the chameleon mechanism that blocks deviation of gravity from the GR in dense environment: The denser the environment is, the weaker the fifth force is (Khoury & Weltman 2004; Li & Barrow 2007).

Although the abundance of galaxy clusters and the strength of their gravitational clusterings have been widely used as one of the most powerful probes of the background cosmology (for a review, see Allen et al. 2011), these probes are unlikely to be efficient discriminators of modified gravity, since the galaxy clusters are usually located in the highly dense supercluster environments where the chameleon effect should be very strong. A recent trend in the cosmological study of  $f(R)$  gravity is to explore its effect on the low-density regions and to figure out which observables among the low-density phenomena is the best indicator of  $f(R)$  gravity. For instance, the dynamic mass of field galaxies, the spin parameters of dwarf void galaxies, the abundance of cosmic voids and etc. have been suggested as useful indicators of large-scale gravity (Zhao et al. 2011a; Lee et al. 2013; Clampitt et al. 2013).

Very recently, Shim & Lee (2013) showed by analyzing the halo catalogs from N-body simulations that the degree of the straightness of rich superclusters changes sig-

nificantly by the presence of cDE. Their results are summarized as (i) the superclusters tend to be less straight in cDE models with stronger coupling; (ii) the difference in the degree of the supercluster straightness is much larger than that in the abundance of the clusters (or superclusters) among different cDE models; (iii) the difference is larger at higher redshifts. Shim & Lee (2013) provided the following explanations for their result: The fifth force generated by the coupling between dark matter and dark energy in cDE models plays a role in making the gravitational clustering of galaxy clusters less isotropic, which is best manifested by the straightness of the superclusters that correspond to the most prominent filamentary structures of the cosmic web.

It is intriguing to ask if the long-range fifth force generated by the scalaron in the  $f(R)$  gravity model also affects on the supercluster straightness. In fact, given the result of Shim & Lee (2013), it is reasonable to expect that the superclusters should be less straight in  $f(R)$  gravity models than in the  $GR$  model. The essential work to undertake here is to investigate quantitatively how sensitively the degree of the supercluster straightness changes by the presence of  $f(R)$  gravity and to examine whether or not it would be powerful enough to distinguish  $f(R)$  not only from GR but also from cDE.

The contents of the upcoming sections are outline as follows. In section 4.2 are briefly described the data from N-body simulations for  $f(R)$  gravity and the algorithms employed to determine the superclusters and their degree of straightness. In section 3.3 are presented the mains result on the dependence of the degree of the supercluster straightness on the strength of  $f(R)$  gravity. In section 3.4 is drawn a final conclusion.

## 3.2 Data and Algorithm

To run a N-body simulation for a  $f(R)$  gravity model, it is first necessary to specify the function  $f(R)$ . We adopt the following Hu-Sawicki model characterized by two parameters  $n$  and  $c_1/c_2$  (Hu & Sawicki 2007):

$$f(R) = -m^2 \frac{c_1(-R/m^2)^n}{c_2(-R/m^2)^n + 1}, \quad (3.1)$$

Here,  $m \equiv 8\pi G\bar{\rho}_m/3$  where  $\bar{\rho}_m$  represents the mean mass density of the universe at present epoch. Following the previous works (Oyaizu 2008; Zhao et al. 2011b), the two parameter values are set at  $c_1/c_2 = 6\Omega_\Lambda/\Omega_m$  and  $n = 1$ . The comparison between the observed abundance evolution of galaxy clusters and the analytic mass function has yielded a tight constraint of  $|f_{R0}| \lesssim 10^{-4}$  for the Hu-Sawicki  $f(R)$  model (Schmidt et al. 2009; Lombriser et al. 2010). Given this cluster-scale constraint, we consider three models: GR and two  $f(R)$  gravity models, F5 and F6, for which the values of  $|f_{R0}|$  are set at  $10^{-5}$  and  $10^{-6}$ , respectively. Throughout this paper, GR represents the standard  $\Lambda$ CDM cosmology where the gravity is described by GR.

For each model, we run a large  $N$ -body simulation by employing the ECOSMOG code (Li et al. 2012b). The simulation contains a total of  $1024^3$  dark matter particles in its periodic box of linear size  $1 h^{-1}\text{Gpc}$ . The initial conditions for each model are all tuned by setting the key cosmological parameters at  $\Omega_m = 0.24$ ,  $\Omega_\Lambda = 0.76$ ,  $\Omega_b = 0.045$ ,  $h = 0.73$ ,  $\sigma_8 = 0.8$ ,  $n_s = 0.96$ . The Amiga's Halo Finder (AHF) code (Knollmann & Knebe 2009) are utilized to identify the bound halos from the spatial distributions of the dark matter particles. For the detailed description of the simulations and the halo-identification procedures, see Knollmann & Knebe (2009) and Li et al. (2012a,b).

Two additional algorithms are employed for our analysis: the friends-of-friends (FoF) group finder and the minimal spanning tree (MST) algorithm. The former is used for the identification of the superclusters and the latter detects the interconnection among the member clusters of each supercluster. Both of the codes treat the cluster-size halos as particles without weighing them by their mass. In other words, no information on the masses of cluster-size halos is required to apply the two algorithms. Only the lower cut-off mass has to be specified when the cluster-size halos are selected (see section 3.3). It is worth mentioning here that the AHF which is used to identify the bound halos is not appropriate to find the superclusters since the AHF is basically a refined spherical over density algorithm (Knollmann & Knebe 2009) while the superclusters are well known to have filamentary shapes (e.g., Dekel et al. 1984; West 1989;

Plionis et al. 1992; Jaaniste et al. 1998; Basilakos et al. 2001; Basilakos 2003; Einasto et al. 2007; Wray et al. 2006; Einasto et al. 2011).

The MST technique has been widely used to understand the interconnected structures of the cosmic web (e.g., Barrow et al. 1985; Krzewina & Saslaw 1996; Doroshkevich et al. 2001; Colberg 2007; Park & Lee 2009a,b; Shim & Lee 2013). As mentioned in Shim & Lee (2013), its usefulness lies in the fact that it does not require to know the underlying distribution of dark matter particles and thus can be directly applied to the observed spatial distributions of galaxies or clusters. In the following section, we describe in detail how the degree of the supercluster straightness is measured from the data with the help of the above algorithms and how it is different among the three modes, GR, F6 and F5. Five different epochs will be considered:  $a = 1.0, 0.9, 0.8, 0.7, 0.6$  where  $a$  is the scale factor.

### 3.3 Effect of $f(R)$ Gravity on the Supercluster Straightness

We take the same procedures that Shim & Lee (2013) followed to determine the degree of the supercluster straightness at each epoch for each model:

- Select those halos with mass  $M_c \geq 10^{13} h^{-1} M_\odot$  as the clusters and identify the FoF groups of clusters as the superclusters. The linking length for the FoF groups is set at  $0.3\bar{l}_c$  where  $\bar{l}_c$  is the mean separation distance among the selected clusters.
- Find the MSTs of those rich superclusters with  $N_c \geq 3$  where  $N_c$  is the number of the member clusters (nodes) and prune each supercluster MST to determine its main stem, called a ‘spine’ by Shim & Lee (2013).
- Select only those rich superclusters with  $N_{\text{node}} \geq 3$  after the pruning where  $N_{\text{node}}$  denotes the number of the nodes that make up the spine of each supercluster.
- Measure the size of each supercluster spine as  $S = \left[ \sum_{i=1}^3 (x_{i,\text{max}} - x_{i,\text{min}})^2 \right]^{1/2}$  when the comoving Cartesian coordinates of a node,  $\{x_i\}_{i=1}^3$ , is in the range of

$$x_{i,\min} \leq x_i \leq x_{i,\max}.$$

- Determine the degree of the straightness of each supercluster spine as its specific size defined as,  $\tilde{S} = S/N_{\text{node}}$  by Shim & Lee (2013) and then take the average of  $\tilde{S}$  over all the selected supercluster spines.

Figure 3.1 plots the mass functions of the clusters (top panel) and the superclusters (bottom panel) at the present epoch ( $a = 1.0$ ) for three different models. As can be seen, the mass functions have highest amplitudes in the F5 model while there is almost no difference between the GR and the F6 cases. Table 3.1 lists the number of the supercluster spines which consist of three or more nodes and the average values of their specific masses defined as  $M_{\text{spine}}/N_{\text{node}}$  where  $M_{\text{spine}}$  is the sum of the masses of all the nodes of a supercluster spine.

In Figure 3.2, the pruning process of a supercluster MST is depicted at  $z = 0$  for the GR case in the two dimensional plane projected onto the  $x_1$ - $x_2$  plane. In the left panel the solid line represents a supercluster MST before pruning and the dots connected by the solid line correspond to their nodes. In the right panel, the solid line corresponds to a supercluster spine (i.e., MST after pruning) while the dashed lines represents the minor branches pruned away from the MST. For the detailed explanation about the pruning process, please see Colberg (2007). Figure 3.3 plots the number distributions of the supercluster spines,  $N_{\text{spine}}$  vs. the number of nodes,  $N_{\text{node}}$  at the present epoch for three models. The result shows that other than the numerical fluctuations there is almost no difference in the node number distribution of the supercluster spines between the GR and the F6 models, while the F5 model has a noticeably higher amplitude.

Figure 3.4 plots the specific size function defined as  $dN_{\text{spine}}/d\tilde{S}$  per unit volume at the present epoch for the three models. As can be seen, there is a noticeable difference in the specific size function among the three models. The specific size function has the highest (lowest) amplitude in the GR (F5) case. Note that there is appreciable difference in the specific size function even between GR and F6. The comparison with the results shown in Figure 3.1 reveals that the difference in the specific size functions among the three models is much bigger than that in the mass function of the superclusters. In

other words, the specific size function of the supercluster spine should be much better indicator of large-scale gravity.

Figure 3.5 shows the average specific sizes of the supercluster spines vs. the scale factor for the three models, demonstrating how  $\langle \tilde{S} \rangle$  evolves in each model. The errors are calculated as the one standard deviation in the measurements of the averages. As can be seen, the mean specific sizes of the superclusters in the GR (F5) model has the highest (lowest) values at all epochs. Note that there is a significant difference between the F6 and the GR models in the average specific size of the supercluster spines although it looks small compared with that between the F5 and the GR models. This result implies that the degree of the straightness of the superclusters should be useful as a new cosmological test of gravity.

Note also that the difference in  $\langle \tilde{S} \rangle$  between the F6 and the GR model increases as the universe evolves. In other words, the effect of  $f(R)$  gravity on the degree of the supercluster straightness becomes stronger as the Universe evolves. It is interesting to compare this result with that of Shim & Lee (2013) according to which the effect of CDE on the degree of the supercluster straightness is stronger at earlier epochs (see Figure 8 in Shim & Lee (2013)). Both of the CDE and the  $f(R)$  gravity has the same effect of lowering the degree of the supercluster straightness but their evolution is directly the opposite, which implies that the degree of the supercluster straightness can be useful to distinguish between the two models.

### 3.4 Discussion and Conclusion

A cosmological test of gravity has become a touchy topic. If an observable is to be regarded powerful in testing gravity, it should be sensitive enough not only to detect any little deviation of true gravity from GR but also to discriminate the effect of modified gravity from that of other energy contents such as coupled dark energy, warm dark matter, and etc. Since it was shown in the several literatures that the linear growth factor  $D(z)$  and the Hubble expansion rate  $H(z)$  evolve differently in modified gravity models from that in the standard  $\Lambda$ CDM, much effort has been made to find observables

which depend strongly on  $D(z)$  and  $H(z)$ .

Very recently, however, Wei et al. (2013) theoretically proved that it is practically impossible to distinguish among the scenarios of modified gravity, coupled dark energy and warm dark matter just by measuring  $D(z)$  and  $H(z)$ , because the predictions of the three scenarios for the growth rate of the large scale structure and the expansion rate of the universe are effectively identical. They called this degeneracy among the three scenarios the "cosmological trinity". Given their claim, an urgent work to undertake is to figure out which cosmological test has a power to break this inherent "trinity". Here, we have shown that the degree of the supercluster straightness has a capacity of completing such a delicate mission. We have found that the superclusters are significantly less straight in  $f(R)$  gravity models than in the GR+ $\Lambda$ CDM. This effect is shown to become stronger in the models with larger values of  $f_{R0}$ . But, even the F6 model which is almost indistinguishable from the standard GR+ $\Lambda$ CDM model exhibits appreciable difference in the degree of the supercluster straightness. The crucial implication of our result is that although the clusters are massive enough to screen modified gravity in them, the intra-cluster force can still be unscreened.

A comparison of our results with those obtained by Shim & Lee (2013) that the effect of cDE on the degree of the supercluster straightness becomes stronger at higher redshifts indicates that the degree of the supercluster straightness can be useful to discriminate the effect of modified gravity from that of cDE. Although we have not investigated how the degree of the superclusters in the WDM models, it is very likely that the presence of WDM would make the superclusters more straight. As discussed in Shim & Lee (2013), the high peculiar velocities of dark matter particles plays a role in making the clustering of galaxy clusters more anisotropic. That is, the WDM would make the superclusters more straight than the CDM.

To use the degree of the supercluster straightness as a cosmological test of gravity, however, it will be much more desirable to have a theoretical framework within which the specific sizes of the supercluster spines can be evaluated for any cosmological models. Since we have obtained our results numerically from a N-body simulations which ran for

a fixed model with specified values of the cosmological parameters, we do not know how much change it would cause to the degree of the supercluster straightness if different initial conditions were used as the simulation inputs. The size of the main stems of the superclusters may correspond to the free streaming scale of the member clusters. Treating each cluster as a particle, it might be possible to model how sensitive their free streaming scales are to the initial conditions of the Universe, using the Lagrangian perturbation theory. Our future work is in this direction.

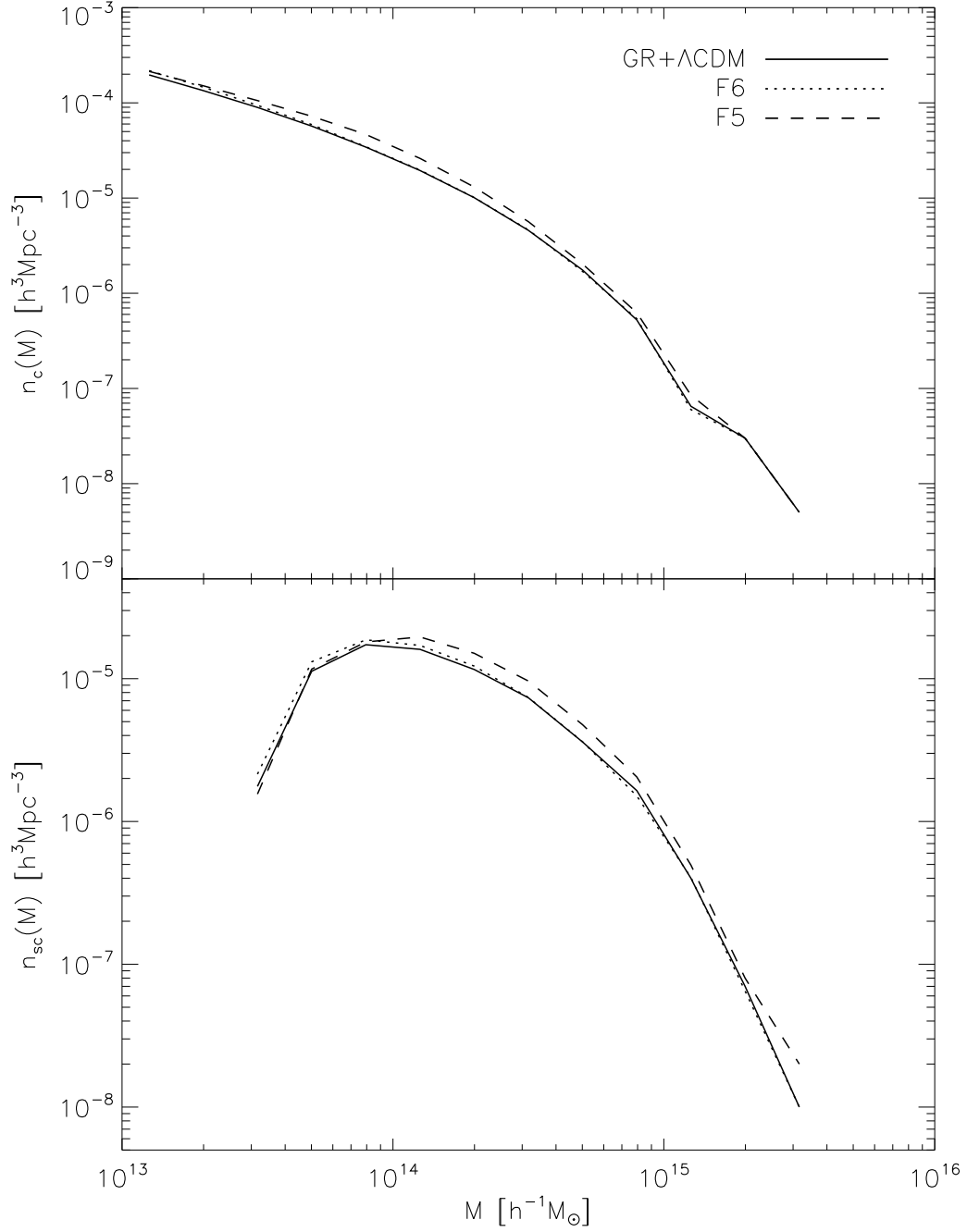


**Figure 3.1.** Mass functions of the cluster and the supercluster halos at  $z = 0$  for three different gravity models in the top and bottom panels, respectively.

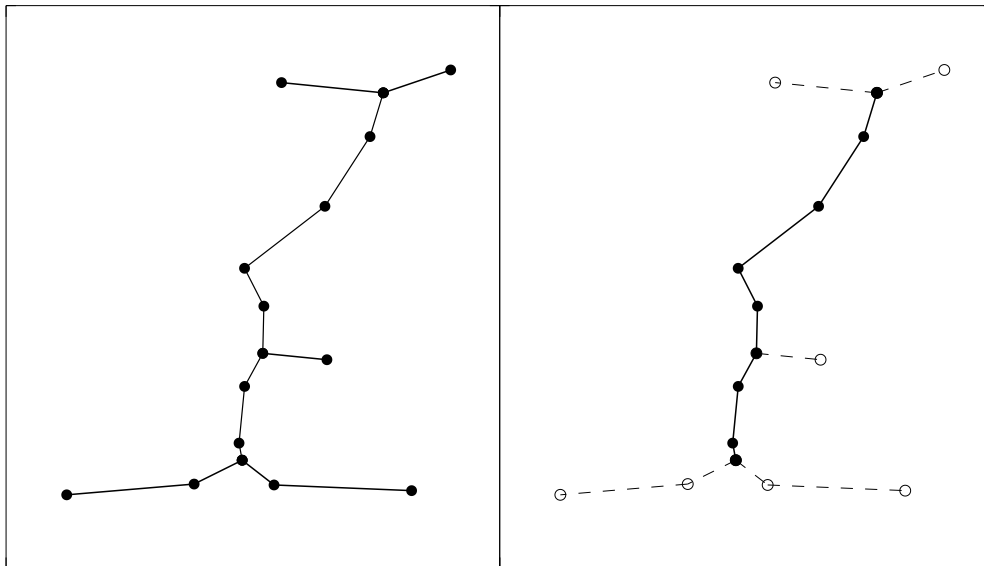


**Figure 3.2.** Pruning of a supercluster to determine its main stems (spine).

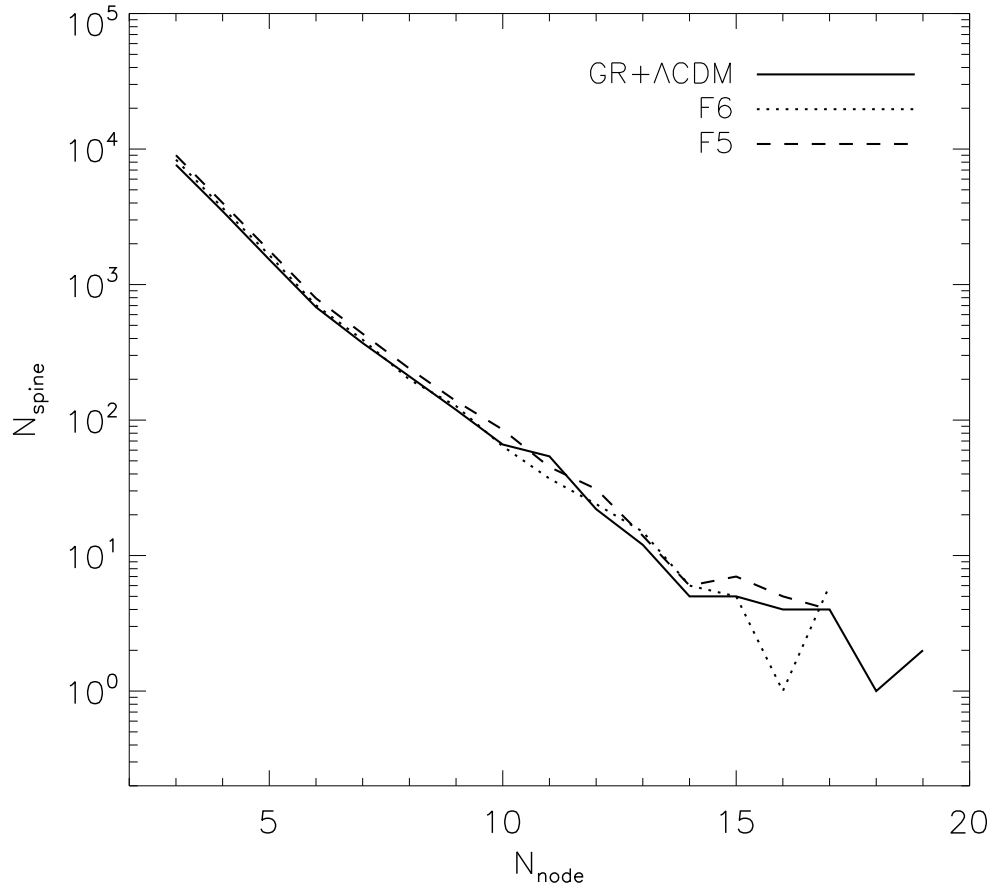


**Figure 3.3.** Number distribution of the superclusters as a function of node at  $z = 0$  for three different models.

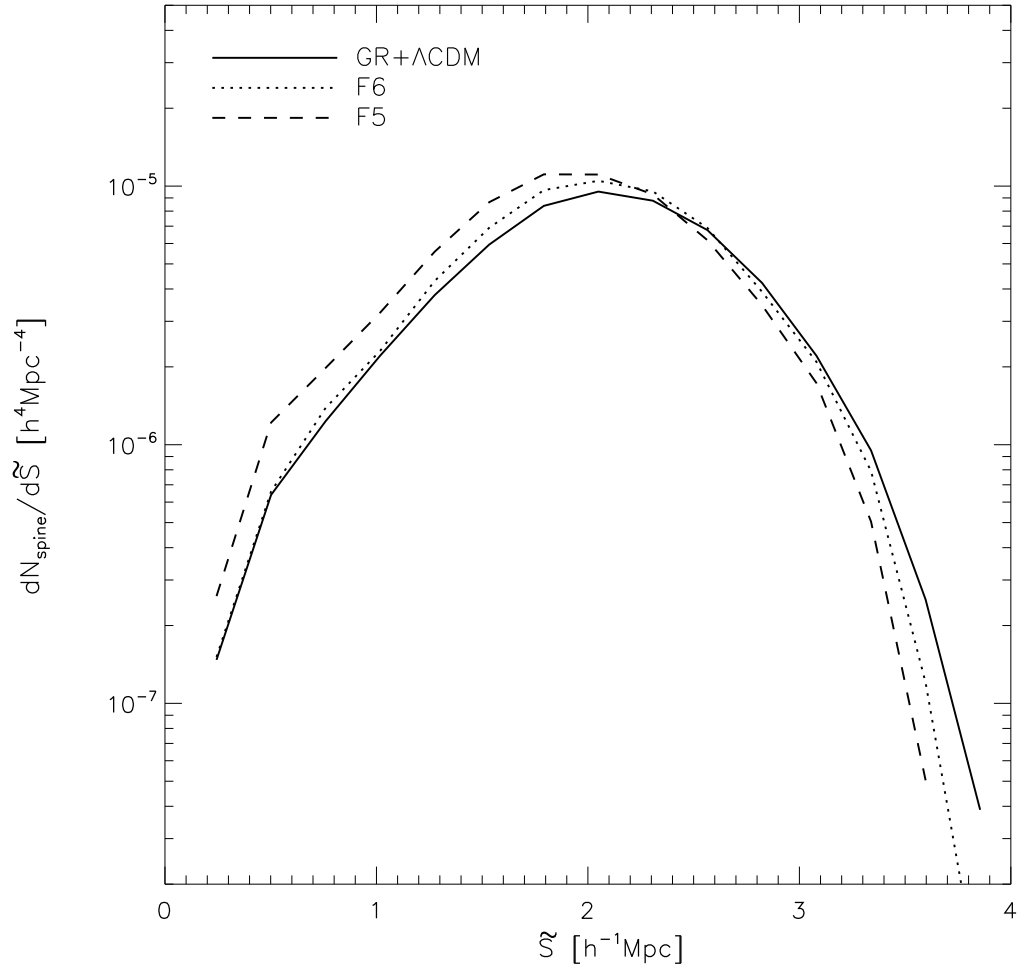


**Figure 3.4.** Specific size distributions of the superclusters at  $z = 0$  for three different models.

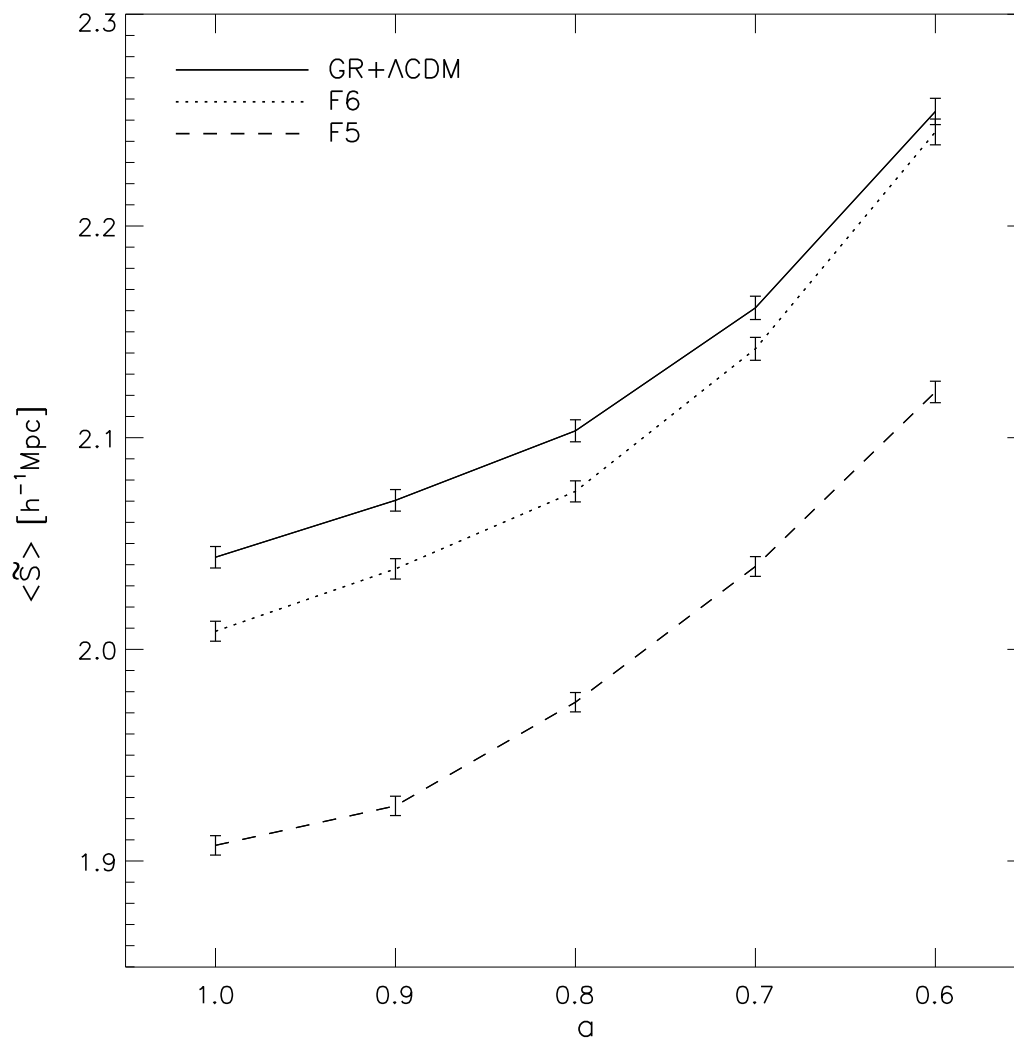


**Figure 3.5.** Evolution of the mean specific sizes of the superclusters with the scale factor  $a$  for three different models.

Table 3.1. Numbers of those supercluster spines with three or more nodes and their mean specific mass for the three models.

model	$N_{\text{spine}}$	$\langle \tilde{M}_{\text{spine}} \rangle$ [ $10^{13} h^{-1} M_{\odot}$ ]
GR	14204	3.92
F6	15260	3.80
F5	16592	4.18



# Bibliography

- Allen, S. W., Evrard, A. E., & Mantz, A. B. 2011, *ARA&A*, 49, 409
- Amendola, L. 2000, *Phys. Rev. D*, 62, 043511
- Amendola, L. 2004, *Phys. Rev. D*, 69, 103524
- Amendola, L. & Tsujikawa, S. 2010, *Dark Energy* (Cambridge University Press:Cambridge)
- Aragón-Calvo, M. A., van de Weygaert, R., & Jones, B. J. T. 2010, *MNRAS*, 408, 2163
- Barrow, J. D., Bhavsar, S. P., & Sonoda, D. H. 1985, *MNRAS*, 216, 17
- Baldi, M., Pettorino, V., Robbers, G., & Springel, V. 2010, *MNRAS*, 403, 1684
- Baldi, M., Lee, J., & Macciò, A. V. 2011, *ApJ*, 732, 112
- Baldi, M. 2012, *MNRAS*, 420, 430
- Basilakos, S., Plionis, M., & Rowan-Robinson, M. 2001, *MNRAS*, 323, 47
- Basilakos, S. 2003, *MNRAS*, 344, 602
- Basilakos, S., Plionis, M., Yepes, G., Gottlöber, S., & Turchaninov, V. 2006, *MNRAS*, 365, 539
- Bean, R., Flanagan, É. É., Laszlo, I., & Trodden, M. 2008, *Phys. Rev. D*, 78, 123514
- Benson, A. J. 2005, *MNRAS*, 358, 551

- Bond, J. R., Kofman, L., & Pogosyan, D. 1996, *Nature*, 380, 603
- Cautun, M., van de Weygaert, R., & Jones, B. J. T. 2013, *MNRAS*, 429, 1286
- Clampitt, J., Cai, Y.-C., & Li, B. 2013, *MNRAS*, 431, 749
- Clifton, T., Ferreira, P. G., Padilla, A., & Skordis, C. 2012, *Phys. Rep.*, 513, 1
- Colberg, J. M. 2007, *MNRAS*, 375, 337
- Davis, M., Efstathiou, G., Frenk, C. S., & White, S. D. M. 1985, *ApJ*, 292, 371
- de Felice, A., & Tsujikawa, S. 2010, *Living Reviews in Relativity*, 13, 3
- Dekel, A., West, M. J., & Aarseth, S. J. 1984, *ApJ*, 279, 1
- Doroshkevich, A. G., Tucker, D. L., Fong, R., Turchaninov, V., & Lin, H. 2001, *MNRAS*, 322, 369
- Einasto, M., Saar, E., Liivamägi, L. J., et al. 2007, *A&A*, 476, 697
- Einasto, M., Liivamägi, L. J., Tago, E., et al. 2011, *A&A*, 532, A5
- Jaaniste, J., Tago, E., Einasto, M., et al. 1998, *A&A*, 336, 35
- Ho, S., Bahcall, N., & Bode, P. 2006, *ApJ*, 647, 8
- Hu, W., & Sawicki, I. 2007, *Phys. Rev. D*, 76, 064004
- Kasun, S. F., & Evrard, A. E. 2005, *ApJ*, 629, 781
- Khoury, J., & Weltman, A. 2004, *Phys. Rev. D*, 69, 044026
- Knollmann, S. R., & Knebe, A. 2009, *ApJS*, 182, 608
- Kolokotronis, V., Basilakos, S., & Plionis, M. 2002, *MNRAS*, 331, 1020
- Komatsu, E., et al. 2011, *ApJS*, 192, 18
- Krzewina, L. G., & Saslaw, W. C. 1996, *MNRAS*, 278, 869

- Lee, J. 2006, *ApJ*, 643, 724
- Lee, J., & Park, D. 2006, *ApJ*, 652, 1
- Lee, J., & Park, D. 2009, *ApJ*, 696, L10
- Lee, J., Hahn, O., & Porciani, C. 2009, *ApJ*, 705, 1469
- Lee, J. 2010, arXiv:1008.4620
- Lee, J. 2012, *ApJ*, 751, 153
- Lee, J., Zhao, G.-B., Li, B., & Koyama, K. 2013, *ApJ*, 763, 28
- Lee, J., & Baldi, M. 2012, *ApJ*, 747, 45
- Li, B., & Barrow, J. D. 2007, *Phys. Rev. D*, 75, 084010
- Li, B., Zhao, G.-B., & Koyama, K. 2012, *MNRAS*, 421, 3481
- Li, B., Zhao, G.-B., Teyssier, R., & Koyama, K. 2012, *JCAP*, 1, 51
- Lombriser, L., Slosar, A., Seljak, U., & Hu, W. 2010, arXiv:1003.300
- Lucchin, F., & Matarrese, S. 1985, *Phys. Rev. D*, 32, 1316
- Macciò, A. V., Quercellini, C., Mainini, R., Amendola, L., & Bonometto, S. A. 2004, *Phys. Rev. D*, 69, 123516
- Mainini, R., & Bonometto, S. 2006, *Phys. Rev. D*, 74, 043504
- Mangano, G., Miele, G., & Pettorino, V. 2003, *Modern Physics Letters A*, 18, 831
- Oyaizu, H. 2008, *Phys. Rev. D*, 78, 123523
- Park, D., & Lee, J. 2007, *Physical Review Letters*, 98, 081301
- Park, D., & Lee, J. 2009, *MNRAS*, 397, 2163
- Park, D., & Lee, J. 2009, *MNRAS*, 400, 1105

- Pettorino, V., & Baccigalupi, C. 2008, *Phys. Rev. D*, 77, 103003
- Plionis, M., Valdarnini, R., & Jing, Y.-P. 1992, *ApJ*, 398, 12
- Planck collaboration, Ade, P. A. R., Aghanim, N., et al. 2013, arXiv:1303.5075
- Planck Collaboration, Ade, P. A. R., Aghanim, N., et al. 2013, arXiv:1303.5076
- Ratra, B., & Peebles, P. J. E. 1988, *Phys. Rev. D*, 37, 3406
- Reyes, R., Mandelbaum, R., Seljak, U., et al. 2010, *Nature*, 464, 256
- Salvatelli, V., & Marchini, A. 2013, arXiv:1304.7119
- Schmidt, F., Vikhlinin, A., & Hu, W. 2009, *Phys. Rev. D*, 80, 083505
- Schmidt, F. 2010, *Phys. Rev. D*, 81, 103002
- Shim, J., & Lee, J. 2013, *ApJ*, 777, 74
- Sotiriou, T. P., & Faraoni, V. 2010, *Reviews of Modern Physics*, 82, 451
- Sousbie, T., Pichon, C., Colombi, S., Novikov, D., & Pogosyan, D. 2008, *MNRAS*, 383, 1655
- Wei, H., Liu, J., Chen, Z.-C., & Yan, X.-P. 2013, *Phys. Rev. D*, 88, 043510
- Wen, Z. L., Han, J. L., & Liu, F. S. 2010, *MNRAS*, 407, 533
- West, M. J. 1989, *ApJ*, 347, 610
- Wetterich, C. 1988, *Nuclear Physics B*, 302, 668
- Wetterich, C. 1995, *A&A*, 301, 321
- Wintergerst, N., & Pettorino, V. 2010, *Phys. Rev. D*, 82, 103516
- Wojtak, R., Hansen, S. H., & Hjorth, J. 2011, *Nature*, 477, 567
- Wray, J. J., Bahcall, N. A., Bode, P., Boettiger, C., & Hopkins, P. F. 2006, *ApJ*, 652, 907

Zhao, G.-B., Li, B., & Koyama, K. 2011, Physical Review Letters, 107, 071303

Zhao, G.-B., Li, B., & Koyama, K. 2011, Phys. Rev. D, 83, 044007



## Chapter 4

# Breaking the Cosmic Degeneracy with the Cosmic Web <sup>1</sup>

### 4.1 Introduction

The gravitational clustering of the large scale structure (LSS) and its evolution reflect the initial conditions of the universe. The basic statistics such as the two point-correlation function of the density field, the mass function of galaxy clusters and the matter-to-halo bias are frequently employed to quantify the strength of the clustering of LSS and to connect them with the early universe. Putting tight constraints on the matter density parameter ( $\Omega_m$ ), the amplitude of the linear power spectrum ( $\sigma_8$ ) and the dark energy equation of state ( $w$ ), the basic statistics of LSS have played a vital role in establishing the concordance  $\Lambda$ CDM (cosmological constant  $\Lambda$  and cold dark matter) cosmology.

Furthermore, it has been found in many literatures that the standard statistics of LSS are quite useful not only for constraining the key cosmological parameters of the  $\Lambda$ CDM cosmology (e.g., Addison et al. 2013; Di Dio et al. 2014, and references therein) but also for testing the viability of the alternative cosmologies such as the warm dark

---

<sup>1</sup>The content of this Chapter was submitted for publication in ApJ and posted in the preprint arXiv with arXiv number arXiv:1404.3639

matter (WDM), coupled dark energy (cDE), and modified theories of gravity (MG) (e.g., Sutter & Ricker 2008; Song & Koyama 2009; Stril et al. 2010; Smith & Markovic 2011; Lombriser et al. 2012; Abebe et al. 2013; Moresco et al. 2013).

The main motivation for proposing the alternative models was to overcome the observational and the theoretical challenges against the  $\Lambda$ CDM cosmology. For instance, the free-streaming effect of the WDM particles may resolve the tensions between the observations and the  $\Lambda$ CDM predictions on the (sub-)galactic scales (e.g., Menci et al. 2012; Viel et al. 2013, and references therein). The dark sector coupling in the cDE models can avoid the finely tuned initial conditions of the universe which was haphazardly required in the  $\Lambda$ CDM cosmology (e.g., Wetterich 1995; Amendola 2000, 2004) while the deviation of the gravitational law from GR on the large scale can accommodate the present acceleration of the universe without requiring dark energy with negative pressure (for a comprehensive review, see Clifton et al. 2012).

However, some cautions have been recently thrown to the rosy prospects for the basic statistics of LSS as a powerful discriminator of the alternative cosmologies. Wei et al. (2013) theoretically proved that the WDM, cDE and MG models are hard to be differentiated from one another just by tracing the expansion and growth history with the LSS observations. Baldi et al. (2014) studied the simultaneous effect of the  $f(R)$  gravity and the massive neutrinos  $\nu$  (say,  $f(R) + \nu$  model) on the structure formation by using large  $N$ -body simulations. The  $f(R)$  gravity is one of the chameleon MG theories (e.g., Lombriser 2014, and references therein) where the  $f(R)$  stands for a specific function of the Ricci scalar  $R$  that appears in the Hilbert-Einstein action as a substitute for  $R$ . The derivative,  $df/dR$ , called, *scalaron*, which represents an additional degree of the freedom quantities the strength of a *fifth force* (see de Felice & Tsujikawa 2010; Sotiriou & Faraoni 2010, for a review). The chameleon mechanism has an effect of screening off the scalaron in the high-densitiy regions where the  $f(R)$  gravity becomes indistinguishable from the GR (e.g., Khoury & Weltman 2004; Brax et al. 2008).

What Baldi et al. (2014) noted in the studies based on the N-body analysis was that the  $f(R) + \nu$  and the  $\Lambda$ CDM models yielded essentially the same basic statistics

of LSS. The effect of free streaming of massive neutrinos (Lesgourgues & Pastor 2006) effectively cancels out that of the fifth force of the  $f(R)$  gravity on the large scale structure. Calling it a cosmic degeneracy, they regarded it as an indication of the fundamental limitation of the basic statistics of LSS as a test of alternative cosmologies, concluding that a novel statistics independent of the standard observables is necessary to break the cosmic degeneracy.

Meanwhile, Shim & Lee (2013) have recently developed a new diagnostic based on the filamentary cosmic web for testing the cDE models under the assumption that the filamentary pattern of the cosmic web would be sensitively affected by the presence of cDE. Regarding the supercluster spines (i.e., the main stems of the superclusters) as the richest filamentary structures in the cosmic web, they determined the specific sizes of the supercluster spines to quantify the degree of the straightness of the superclusters and found that the specific size distributions of the supercluster spines substantially differ among various cDE models, implying that it is indeed a good indicator of cDE. Furthermore, Shim et al. (2014) investigated the effect of  $f(R)$  gravity on the specific sizes of the supercluster spines and showed that the evolution trends of the specific size distributions of the superclusters differ between the cDE and the  $f(R)$  gravity models, which indicated that this new diagnostic developed by Shim & Lee (2013) is in principle capable of breaking the degeneracy between the two models.

In the light of the works of Shim et al. (2014) and Baldi et al. (2014), we would like to explore here whether or not the the degree of the straightness of the superclusters quantified by the specific size of the supercluster spines can be also useful for breaking the cosmic degeneracy between the  $\Lambda$ CDM and the  $f(R) + \nu$  models. In section 4.2 we will describe how the supercluster samples are obtained from the simulation datasets obtained from the work of Baldi et al. (2014). In section 4.3 we will show how the specific sizes of the supercluster spines are affected by the simultaneous effects of the  $f(R)$  gravity and the massive neutrinos. In section 6.4 we discuss the implication of our result as well as its prospect.

## 4.2 Constructing the Supercluster Samples

Baldi et al. (2014) carried out large N-body simulations for the standard GR+ $\Lambda$ CDM and also for four different  $f(R) + \nu$  models (namely, F4+ $\nu$ 0, F4+ $\nu$ 02, F4+ $\nu$ 04, F4+ $\nu$ 06) for which the value of the neutrino mass  $mu_\nu$  was set at 0.2, 0.4, 0.6 eV, respectively. The Hu-Sawicki formula was adopted to specify  $f(R)$  (Hu & Sawicki 2007) and the value of the scalaron at the present epoch,  $f_{R0} \equiv df/dR|_{t_0}$ , was set at  $10^{-4}$ . Although recent observations indicate  $f_{R0} \leq 10^{-5}$  on the cluster scale (e.g., Schmidt et al. 2009; Lombriser et al. 2012), Baldi et al. (2014) chose this rather exaggeratedly high value of  $f_{R0}$  to see clearly how the free streaming of massive neutrinos cancel out that of the fifth force.

For the computation of the trajectories of a total of  $512^3$  CDM particles of mass in the simulation box of linear size,  $L_p = 1 h^{-1}\text{Gpc}$ , the prevalent Tree PM GADGET3 was utilized as the basic code into which the MG- GADGET scheme (Puchwein et al. 2013) was incorporated. The effect of the free streaming of the  $512^3$  massive neutrinos included in the simulation box was modeled by using the algorithm constructed by Viel et al. (2010). The values of the key cosmological parameters for the  $\Lambda$ CDM cosmology was set at the Planck values (Planck Collaboration et al. 2014). The bound dark halos were resolved as the standard friends-of-friends (FoF) groups of only CDM particles for which the linkage parameter of the FoF was set at the conventional value of 0.2. For the detailed description of the simulation, see Baldi et al. (2014).

From the cluster halos selected from the  $N$ -body datasets of Baldi et al. (2014) at three different epochs ( $z = 0, 0.3, 0.6$ ), we extract the superclusters. As done in Shim & Lee (2013) and Shim et al. (2014), a sample of the cluster halo is first created by choosing those dark halos in the catalog whose masses exceed the lower limit of  $10^{13} h^{-1} M_\odot$  at each redshift for each model. The mean separation distance among the cluster halos is calculated and then the marginally bound superclusters are identified as the FoF groups of the cluster halos with the linkage parameters of 0.3. Binning the halo mass range and calculate their number densities belonging to each mass bin, we determine both of the cluster and the supercluster mass functions.

The top and the bottom panel of Figure 4.1 shows the cluster and the supercluster mass function, respectively, at  $z = 0$  for five models. As can be seen, those models with lower values of  $m_\nu$  exhibit higher number densities of high-mass superclusters ( $M \geq 10^{15} h^{-1} M_\odot$ ). Note also that the supercluster mass function for the  $\Lambda$ CDM model is almost identical to that for the F4+ $\nu$ 04 model, which indicates that the neutrino mass required to cancel out the effect of the fifth force on the supercluster mass functions is 0.4 eV. This result is in a complete agreement with the finding of Baldi et al. (2014) that the standard statistics including the cluster functions are not capable of discriminating the  $\Lambda$ CDM model from the F4+ $\nu$ 04 model.

### 4.3 Simultaneous Effect of MG and $\nu$ on the Supercluster Straightness

We analyze the supercluster sample for each model at each redshift to determine the mean specific sizes of the supercluster spines, by the prescriptions described in Shim & Lee (2013) and Shim et al. (2014):

- Apply the minimum spanning tree (MST) algorithm (Barrow et al. 1985; Colberg 2007) to the supercluster sample from the simulation of Baldi et al. (2014) to determine a MST of each supercluster.
- From each supercluster MST, prune away repeatedly the minor twigs having less than three nodes until the main stem of each supercluster (spine) is determined and count the numbers of the member clusters belonging to the main stem (nodes).
- Select only those superclusters whose spines consist of three or more nodes.
- Find a cuboid which fits the spatial distribution of the nodes of each supercluster spine and measure the length of its diagonal line as the size of each supercluster spine (Park & Lee 2009).

- Determine the specific size ( $\tilde{S}$ ) of each supercluster spine by dividing the size by the node number ( $N_{\text{node}}$ ).
- Calculate the mean value of  $\tilde{S}$  averaged over all supercluster spines.

Figure 4.2 plots the mean specific sizes,  $\langle \tilde{S} \rangle$  of the supercluster spines versus the models. The errors are calculated as one standard deviation in the measurement of the mean value. The value of  $\langle \tilde{S} \rangle$  is shown to monotonically increase as the value of  $m_\nu$  increases from 0 to 0.6 eV. Interestingly, it is not the F4+ $\nu$ 04 model but the F4+ $\nu$ 02 model which predicts almost the same  $\langle \tilde{S} \rangle$  as the  $\Lambda$ CDM cosmology. In fact, between the  $\Lambda$ CDM and the F4+ $\nu$ 04 there is a substantial difference in the value of  $\langle \tilde{S} \rangle$ . Given that that it is the F4+ $\nu$ 04 model which the standard statistics fails to distinguish from the GR+ $\Lambda$ CDM model, our results indicates that the values of  $m_\nu$  required to compensate for the effect of the fifth force on the specific sizes of the supercluster spines and on the basic statistics of LSS are different from each other. This result leads us to expect that it may be possible to break the cosmic degeneracy between the GR+ $\Lambda$ CDM and the F4+ $\nu$  models if the basic statistics of LSS are combined with the specific size distribution of the supercluster spines.

Figure 4.3 plots the mean specific sizes of the supercluster spines versus redshifts for the five models, showing how  $\langle \tilde{S} \rangle$  evolves in each model and how different the evolution trend is. As can be seen, the difference in  $\langle \tilde{S} \rangle$  among the fives models becomes larger at higher redshifts, which is consistent with the result of Shim et al. (2014) who showed that the effect of  $f(R)$  gravity on the specific size distribution becomes larger at higher redshifts. At higher redshifts the mean specific size of the supercluster spine becomes larger in all of the five models. The F4+ $\nu$ 06 model exhibits the most rapid evolution of  $\langle \tilde{S} \rangle$ , which implies that the free streaming of more massive neutrinos have a higher effect of sharpening the filamentary structures when they were more energetic at higher redshifts. Note that although it is impossible to distinguish between the GR+ $\Lambda$ CDM and the F4+ $\nu$ 02 model by measuring  $\langle \tilde{S} \rangle$ , it is possible at  $z \geq 0.3$  when the value of  $\langle \tilde{S} \rangle$  even for the F4+ $\nu$ 02 model deviates from that for the GR+ $\Lambda$ CDM case. In other words, if measured at redshifts  $z \geq 0.3$ , even without being combined with the basic

statistics of LSS, the new statistics based on the specific size of the supercluster spine is in principle capable of breaking the cosmic degeneracy between the standard  $\Lambda$ CDM and the  $f(R) + \nu$  models.

#### 4.4 Discussion and Conclusion

This work has been inspired by two recent literatures. One is Shim et al. (2014) which demonstrated that the specific size of the supercluster spine is a powerful diagnostic not only for detecting any  $f(R)$  modification of the GR but also for distinguishing the effect of  $f(R)$  gravity from that of the presence of cDE. The other is Baldi et al. (2014) which raised a cosmic degeneracy problem that the basic statistics of LSS would inherently fail to distinguish the  $F4+\nu04$  model from the standard  $\Lambda$ CDM cosmology since the free streaming effect of massive neutrinos with mass 0.4eV effectively cancels out the clustering effect of the fifth force scalaron with  $|f_{R0}| = 10^{-4}$  on the basic statistics of LSS such as cluster mass function, two-point correlation function of the density field and matter-to-halo bias.

Using the numerical data from the N-body simulations conducted by Baldi et al. (2014) and the techniques developed by Shim et al. (2014), we have determined the mean specific sizes of the supercluster spines at three different redshifts ( $z = 0, 0.3, 0.6$ ) for various different  $f(R) + \nu$  models. It has been found that the neutrino mass required to cancel out the effect of the fifth force on the specific size distribution of the supercluster spines at  $z = 0$  is 0.2eV, which turns out to be different from the value 0.4eV required to fail the basic statistics of LSS in distinguishing between the  $F4+\nu$  and the  $GR+\Lambda$ CDM models. Henceforth, the specific size of the supercluster spine will play a complimentary role in breaking the cosmic degeneracy at  $z = 0$ . We have also found that at redshifts  $z \geq 0.3$  the specific size of the supercluster spine pulls it off to distinguish all of the  $f(R) + \nu$  models from the  $GR+\Lambda$ CDM cosmology without the help of the basic statistics of LSS. We finally conclude that by tracing the evolution of the specific sizes of the supercluster spines, it will be capable of breaking the cosmic degeneracy between the  $\Lambda$ CDM and the  $f(R) + \nu$  model.

Room for future improvements exist for backing up the final conclusion of ours. First of all, the datasets used for our analysis were obtained from only an intermediate-resolution  $N$ -body simulations. Since the identification of the superclusters especially at high redshifts are likely to be affected by the resolution of  $N$ -body simulations, a new dataset from high-resolution simulations is required to examine more carefully how the mean specific sizes of the supercluster spines evolve with redshifts. Secondly, in the current work we have considered only the case that the scalaron has a exaggeratedly high value of  $f_{R0} = 10^{-4}$ . It will be necessary to examine if the specific size of the supercluster spine is able to break the cosmic degeneracy even in the case that the scalaron has a lower value. Another direction into which the future improvements should be made is constructing an analytic model for the mean specific size of the supercluster spine. One of the reasons that the basic statistics of LSS has been so widely used as a test of cosmology is that they can be analytically predictable. Whereas the mean specific sizes of the supercluster spines have so far been only numerically determined without being guided by any analytic prescription, which is an obvious downside that has to be overcome for its practical application in the future.

Finally, the most important part may be an applicability of this scheme on observation. Considering the current and previous numerical findings (Shim & Lee 2013; Shim et al. 2014), we conducted a feasibility study by applying our approach to both observation and simulation data to test if the  $\Lambda$ CDM cosmology well reproduces our Universe in terms of the specific sizes of filaments<sup>2</sup>. Large-scale filaments are identified from the galaxy distributions of SDSS DR12 and mock surveys of the Horizon Run 4 (HR4) simulation of  $\Lambda$ CDM cosmology. We successively apply the FOF algorithm to identify galaxy clusters from the galaxies, and filaments from the clusters. For fair comparison, the same number density of galaxies and observation geometry are applied. (We regard the galaxies within  $z \approx 0.09$  correspond to those in the  $z = 0$  snapshot data of the simulation assuming negligible evolution of the galaxies and filaments at that redshift range.)

---

<sup>2</sup>Shim J., Hwang H., Kim J., Hong S., & Park C. in preparation

In Figure 4.4, the cumulative  $\tilde{S}$  distribution of the DR12 filaments safely lies within the range spanned by those of the mocks. As can be seen in Figure 4.5, the mean specific size of the DR12 filaments is slightly biased toward the rightwing of the HR4 mocks, but is only  $1.3\sigma$  away from the mean of mean distribution of HR4 mocks. Hence, we do not detect any inconsistency between the observation and the  $\Lambda$ CDM with filaments at the present epoch. It will be more beneficial to perform a similar analysis at higher redshift, because larger deviation (if any) from the  $\Lambda$ CDM is expected to show up in distant Universe (Shim & Lee 2013; Shim et al. 2014). Hopefully, this preliminary analysis can be extended to the distant Universe via the upcoming large galaxy redshift surveys that are focusing on high redshift galaxies, like Euclid (Laureijs et al. 2011), DESI (DESI Collaboration et al. 2016), and possibly eBOSS (Dawson et al. 2016).

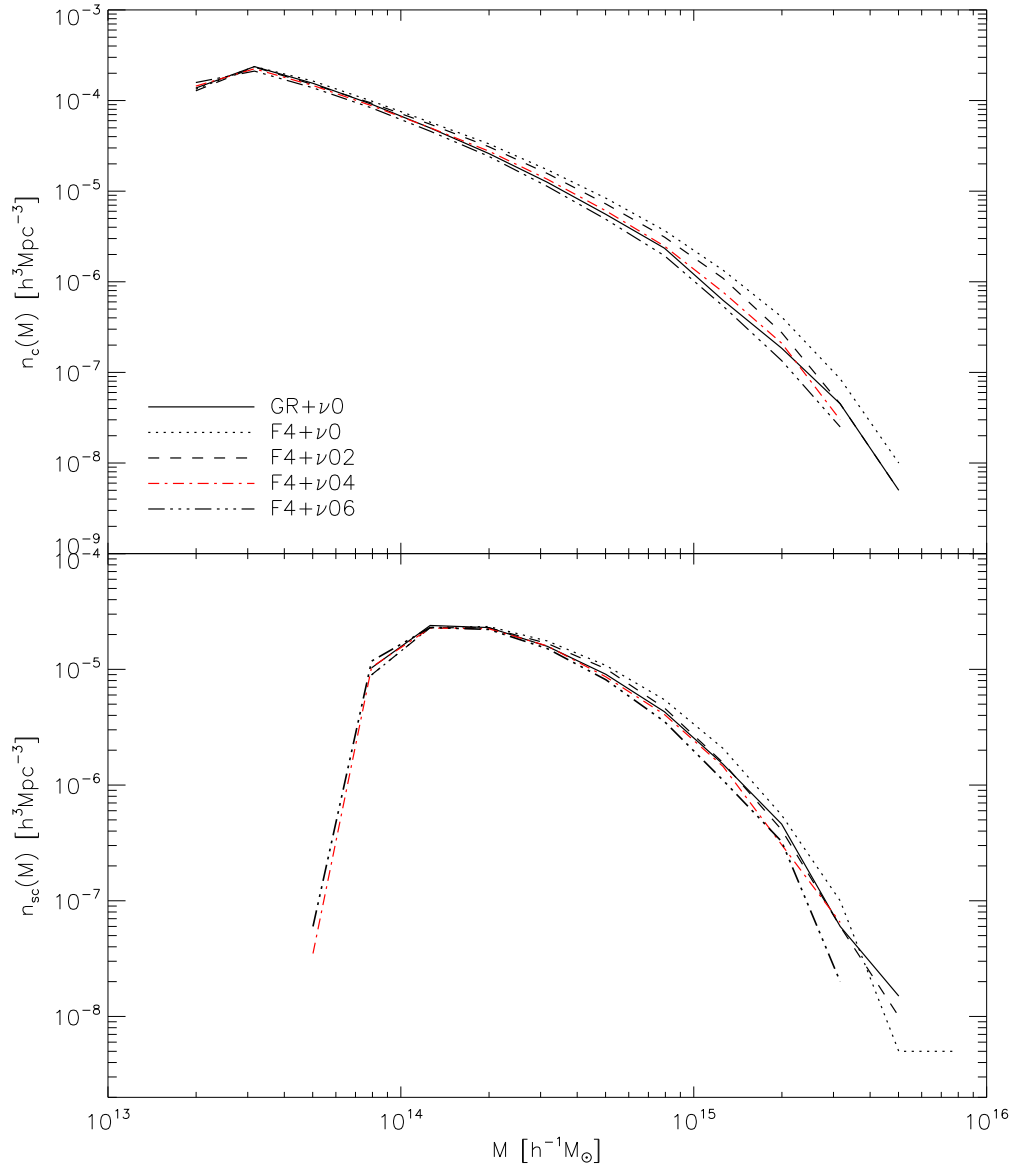


**Figure 4.1.** Mass functions of the cluster halos and the superclusters for five different models at  $z = 0$  in the top and the bottom panel, respectively.

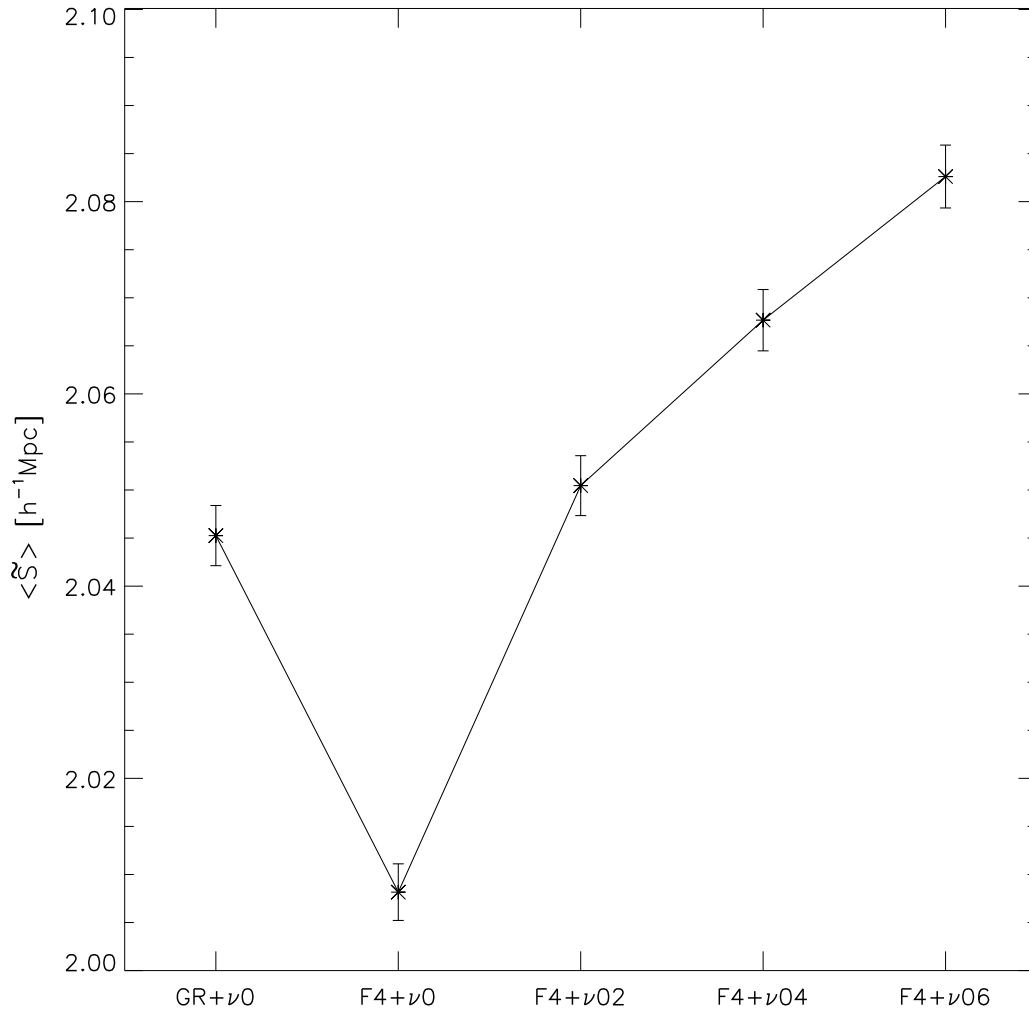


**Figure 4.2.** Mean specific sizes of the supercluster spines for five different models at  $z = 0$ . The errors represent one standard deviation in the measurement of the mean value.

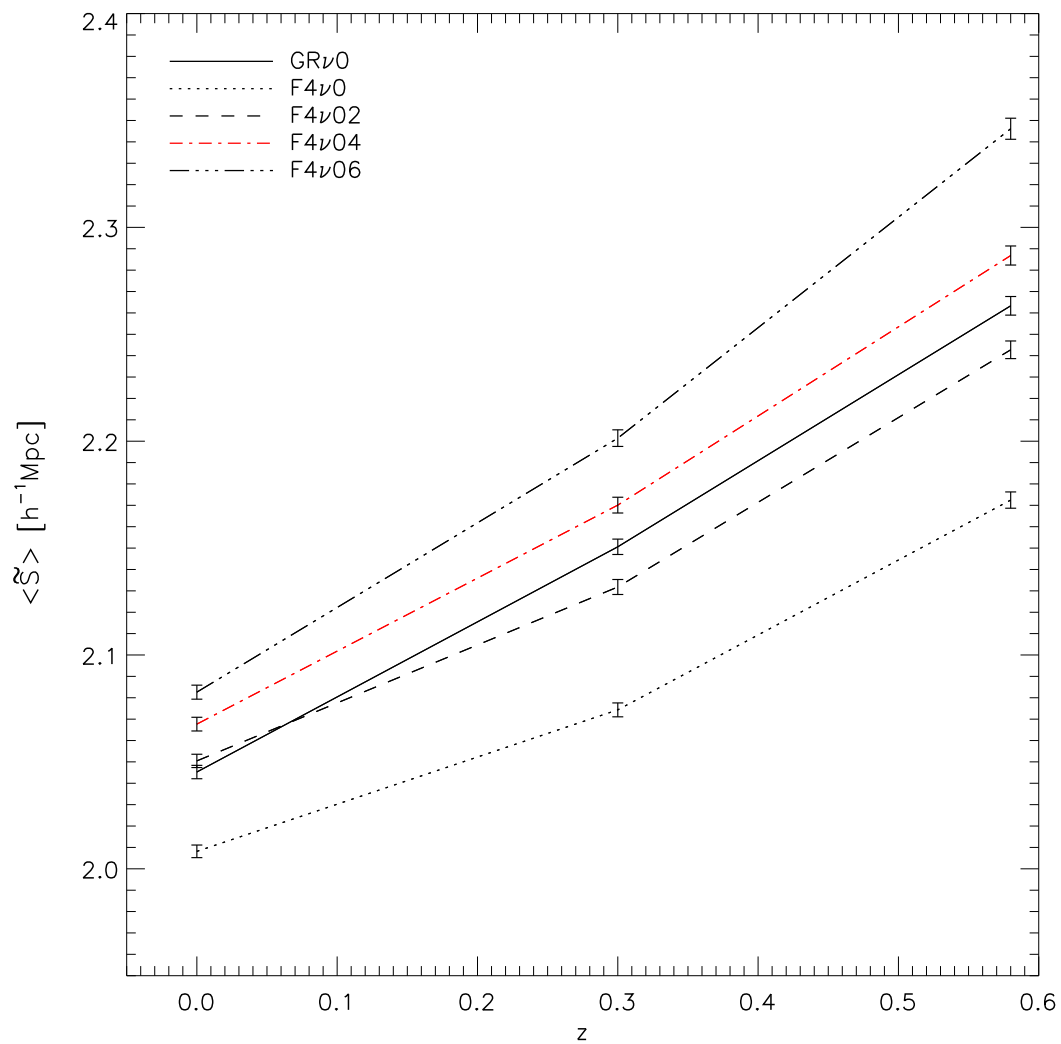


**Figure 4.3.** Evolution of the mean specific sizes of the supercluster spines for five different models.

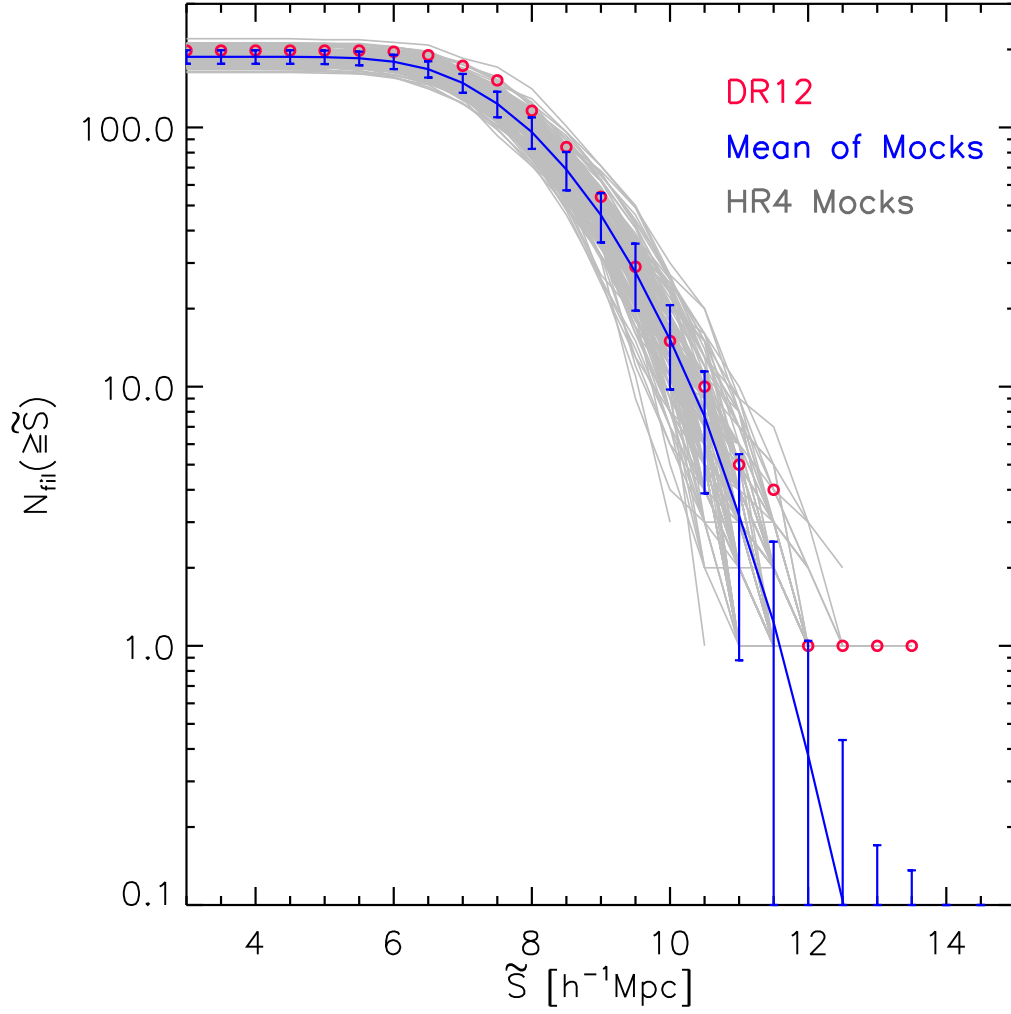


**Figure 4.4.** Cumulative specific size distributions of filaments in DR12 (red open circle), 135 HR4 mocks (gray line), and the mean of mocks (blue line) with the errors calculated as the standard deviation in the mocks. The cumulative specific size distribution of DR12 filaments is consistent to those of HR4.

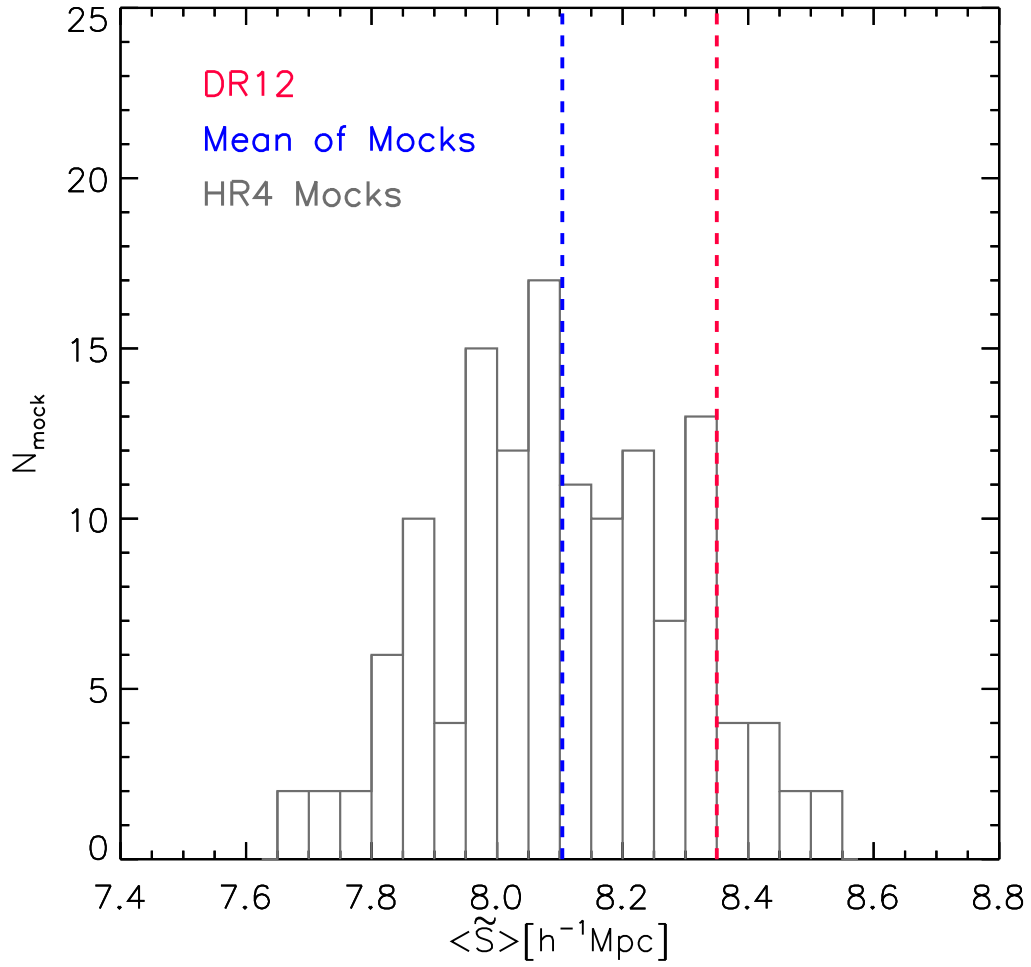


**Figure 4.5.** Number distribution of mean specific sizes of 135 HR4 mock surveys in gray bars. The mean of mock distribution is indicated in blue dashed lines, while that of DR12 is in red dashed line. The mean specific size of DR12 filaments deviates from that of the mock distribution by  $1.3\sigma$ .

# Bibliography

- Abebe, A., de la Cruz-Dombriz, Á., & Dunsby, P. K. S. 2013, *Phys. Rev. D*, 88, 044050
- Addison, G. E., Hinshaw, G., & Halpern, M. 2013, *MNRAS*, 436, 1674
- Amendola, L. 2000, *Phys. Rev. D*, 62, 043511
- Amendola, L. 2004, *Phys. Rev. D*, 69, 103524
- Baldi, M., Villaescusa-Navarro, F., Viel, M., et al. 2013, *MNRAS* in press  
[arXiv:1311.2588]
- Barrow, J. D., Bhavsar, S. P., & Sonoda, D. H. 1985, *MNRAS*, 216, 17
- Brax, P., van de Bruck, C., Davis, A.-C., & Shaw, D. J. 2008, *Phys. Rev. D*, 78, 104021
- Clifton, T., Ferreira, P. G., Padilla, A., & Skordis, C. 2012, *Phys. Rep.*, 513, 1
- Colberg, J. M. 2007, *MNRAS*, 375, 337
- de Felice, A., & Tsujikawa, S. 2010, *Living Reviews in Relativity*, 13, 3
- DESI Collaboration, Aghamousa, A., Aguilar, J., et al. 2016, arXiv:1611.00036
- Di Dio, E., Montanari, F., Durrer, R., & Lesgourgues, J. 2014, *JCAP*, 1, 42
- Hu, W., & Sawicki, I. 2007, *Phys. Rev. D*, 76, 064004
- Khoury, J., & Weltman, A. 2004, *Phys. Rev. D*, 69, 044026
- Krzewina, L. G., & Saslaw, W. C. 1996, *MNRAS*, 278, 869

- Lesgourgues, J., & Pastor, S. 2006, *Phys. Rep.*, 429, 307
- Li, B., & Barrow, J. D. 2007, *Phys. Rev. D*, 75, 084010
- Lombriser, L., Slosar, A., Seljak, U., & Hu, W. 2012, *Phys. Rev. D*, 85, 124038
- Lombriser, L. 2014, arXiv:1403.4268
- Menci, N., Fiore, F., & Lamastra, A. 2012, *MNRAS*, 421, 2384
- Moresco, M., Marulli, F., Baldi, M., Moscardini, L., & Cimatti, A. 2013, arXiv:1312.4530
- Park, D., & Lee, J. 2009, *MNRAS*, 397, 2163
- Planck Collaboration, Ade, P. A. R., Aghanim, N., et al. 2014, *A&A*, 571, A16
- Puchwein, E., Baldi, M., & Springel, V. 2013, *MNRAS*, 436, 348
- Schmidt, F., Vikhlinin, A., & Hu, W. 2009, *Phys. Rev. D*, 80, 083505
- Shim, J., & Lee, J. 2013, *ApJ*, 777, 74
- Shim, J., Lee, J., & Li, B. 2013, *ApJ*, 784, 84
- Smith, R. E., & Markovic, K. 2011, *Phys. Rev. D*, 84, 063507
- Song, Y.-S., & Koyama, K. 2009, *JCAP*, 1, 48
- Sotiriou, T. P., & Faraoni, V. 2010, *Reviews of Modern Physics*, 82, 451
- Stril, A., Cahn, R. N., & Linder, E. V. 2010, *MNRAS*, 404, 239
- Sutter, P. M., & Ricker, P. M. 2008, *ApJ*, 687, 7
- Viel, M., Haehnelt, M. G., & Springel, V. 2010, *JCAP*, 6, 15
- Viel, M., Becker, G. D., Bolton, J. S., & Haehnelt, M. G. 2013, *Phys. Rev. D*, 88, 043502

- Wei, H., Liu, J., Chen, Z.-C., & Yan, X.-P. 2013, *Phys. Rev. D*, 88, 043510
- Wetterich, C. 1995, *A&A*, 301, 321



## Chapter 5

# Dependence of the Substructure Abundance on the Orientation Coherence of the Halo Tidal Field <sup>1</sup>

### 5.1 Introduction

The substructure of dark matter halos has been the subject of many literatures in which analytical and/or numerical methods were employed to investigate such intriguing topics as the mass and spatial distributions of substructures, the dependence of substructure abundance on the large-scale density and tidal fields as well as on the host halo mass, the effects of tidal stripping and dynamical friction on the survival rates of substructures and so on (e.g., Tormen et al. 1998; Sheth 2003; Lee 2004; De Lucia et al. 2004; Natarajan & Springel 2004; Oguri & Lee 2004; van den Bosch et al. 2005; Hahn et al. 2009; Hester & Tasitsiomi 2010; Gao et al. 2011; Tillson et al.

---

<sup>1</sup>The content of this Chapter was submitted as a journal paper for publication in ApJ and posted in the preprint arXiv with arXiv number arXiv:1801:09960v1. Once it is published, the copyright will belong to the American Astronomical Society.

2011; Wang et al. 2011; Croft et al. 2012; Wu et al. 2013; Xie & Gao 2015; Jiang & van den Bosch 2017; Borzyszkowski et al. 2017; Garaldi et al. 2017). Owing to those previous endeavors, a coarse roadmap is now established to explain the presence and properties of the substructures of dark matter halos in the standard  $\Lambda$ CDM ( $\Lambda$  + Cold Dark Matter) universe.

The presence of substructures in a bound halo is a natural consequence of hierarchical merging process. Once a substructure forms, it is prone to severe mass-loss due to various dynamical effects such as tidal stripping, close encounter, and dynamical friction inside its host halo (e.g., Tormen et al. 1998; Taylor & Babul 2004). The longer a substructure is exposed to those dynamical effects, the harder it can survive. Thus, at fixed mass a halo that forms earlier tends to contain less number of substructures (or equivalently, less mass fraction) (e.g., see Jiang & van den Bosch 2017). Among various factors that affect the formation epoch of a halo, the most principal one has been found the strength of the external tidal forces exerted by the neighbor halos, which tend to interrupt the infall of satellites and the accretion of matter particles onto the halo: The galactic halos of fixed mass in the stronger tidal fields form on average earlier and in consequence possess less substructures (Wang et al. 2011).

It is not only the tidal strength but also the configurations of the tidal fields in the surrounding that play a crucial role in the obstruction of the satellite infall and mass accretion into the halos (Hahn et al. 2009; Shi et al. 2015; Borzyszkowski et al. 2017). Two recent numerical studies based on the high-resolution simulations (Borzyszkowski et al. 2017; Garaldi et al. 2017) found a significant difference in the substructure abundance between the galactic halos located in two different tidal environments. One is inside a thick "prominent" filament while the other is at the junction of multiple thin "secondary" filaments. For the former case, the satellite infall and matter accretion into a galactic halo is encumbered since the satellites and matter particles develop tangential velocities perpendicular to the direction of the elongated axis of the filament, while for the latter case the satellites and matter particles can acquire radial motions falling onto the halos (Borzyszkowski et al. 2017). The galactic halos located in the bulky

straight filaments tend to form early before the complete formation of the filaments, which leads to smaller number of substructures than their counterparts at the present epoch (Garaldi et al. 2017).

As the main purpose of the previous works that have established the above roadmap was to physically explain the assembly bias on the galactic scale as well as a paucity of satellites around the Milky Way (Gao & White 2007), their focus was primarily put on the galactic halos and their substructures (Hahn et al. 2009; Mao et al. 2015). Although it is expected that the formation of the substructures of the cluster halos would be similarly affected by the tidal fields, the link between the substructure abundances of the cluster halos and the external tidal field may not be the formation epochs unlike for the case of the galactic halos. It was indeed numerically found that the formation epochs of the cluster halos were nearly independent of the strength of the external tidal forces and that the formation epochs (or equivalently the concentration parameters) of cluster halos at fixed mass did not play the most decisive role in shaping the substructure abundance (Gao et al. 2011). Besides, on the cluster scale it is difficult to make a quantitative distinction between the thick primary and the thin secondary filaments unlike on the galactic scale, and thus the results of Borzyszkowski et al. (2017) and Garaldi et al. (2017) cannot be readily extended to the cluster scale.

Here, we take a different approach to address the issue of the tidal effect on the substructure abundance of the cluster halos. Introducing a new concept of the *orientation coherence* of the surrounding tidal fields and quantitatively distinguishing between different tidal environments in terms of the specific sizes of the filaments, we will quantitatively investigate how the substructure abundance of the cluster halos depend on the orientation coherence of the surrounding tidal fields. The organization of this Paper is as follows. Section 5.2 represents the procedures to identify the filaments composed of the cluster halos from a high-resolution N-body simulation and to determine their specific sizes. Section 5.3 presents the measurements of the correlations between the substructure abundance of the cluster halos and the specific sizes of the filaments. Section 5.4 presents a physical interpretation of the results, discussing the necessary future

improvements of our analysis.

## 5.2 Identifying the Filaments of Cluster Halos

In the previous numerical works which endeavored to quantify the tidal influence on the substructure abundance of dark halos, the first step taken was usually to construct the surrounding tidal field either from the dark matter particles (matter tidal field) or from the neighbor halos (halo tidal field) (e.g., Hahn et al. 2009; Wang et al. 2011; Shi et al. 2015). In the current work, however, instead of constructing the tidal field, our first step is to identify the filaments composed of cluster halos by employing the adapted minimal spanning tree (MST) algorithm (Colberg 2007; Park & Lee 2009a,b; Shim & Lee 2013; Alpaslan et al. 2014). An advantage of our approach is that it can reduce the risk of contamination caused by the numerical noise generated during the construction of the halo tidal field on the cluster scale. As shown by Wang et al. (2011), the substructure abundance of dark halos exhibits a stronger correlation with the halo tidal field constructed from the neighbor halos with comparable masses rather than with the matter tidal field.

But, it would suffer considerably from the small-sample statistics to construct the halo tidal field from the spatial distributions of the cluster halos due to the rareness of the cluster halos. Furthermore, during the construction procedure, the halo tidal field is often smoothed with a spherical window function, which has an effect of undermining the degree of the anisotropy of the tidal field. Given the previous result that the strongest tidal influence on the substructure abundance of dark halos can be found when the surrounding tidal field has highest anisotropy (Borzyszkowski et al. 2017), the smoothing process during the construction of the halo tidal field could also obscure the results. Since no smoothing process is involved in the identification of the MST filaments, our approach can avoid this possible systematics. Another merit of our approach based on the adapted MST algorithm is its direct applicability to real observations. As well explained and compared with the other algorithms in Libeskind et al. (2018), the adapted MST algorithm is capable of automatically adjusting the red-shift

space distortion effect. Without making any specified assumption of the background cosmology, it is possible to extract the filaments out of the spatial distributions of the bound objects observed in redshift space and to directly study the tidal influences of the extracted filaments.

For our analysis, we will make five samples of the cluster halos and their substructures retrieved from the Rockstar Halo Catalog of the Big MultiDark-Planck (Big MDPL) simulations (Riebe et al. 2013; Behroozi et al. 2013; Klypin et al. 2016). The Planck cosmology was adopted for the Big MDPL simulation starting from the initial conditions described by the following key parameters:  $\Omega_m = 0.307$ ,  $\Omega_b = 0.048$ ,  $\Omega_\Lambda = 0.693$ ,  $n_s = 0.96$ ,  $\sigma_8 = 0.8228$  and  $h = 0.6777$  (Planck Collaboration et al. 2014). The comoving linear length of the simulation box ( $L_b$ ), the mass resolution ( $m_{\text{cdm}}$ ), and the number of the CDM particles ( $N_{\text{cdm}}$ ) used for the Big MDPL simulations are given as  $L_b = 2.5 h^{-1} \text{Gpc}$ ,  $m_{\text{cdm}} = 2.359 \times 10^{10} h^{-1} M_\odot$ , and  $N_{\text{cdm}} = 3840^3$ , respectively.

Information on the ID, virial mass, spin parameter, comoving position and velocity of the center of mass, parent ID (pID) of each dark halo can be retrieved from the Rockstar Halo Catalog of the Big MDPL. If a dark halo has a parent ID equal to  $-1$ , then it is a distinct halo without belonging to a larger halo. Otherwise, it is a substructure contained in a larger host halo and its parent ID represents the corresponding ID of its host halo. For our analysis, a cluster halo is defined as a distinct Rockstar halo with pID =  $-1$  having virial mass of  $M_{\text{host}} \geq 10^{14} h^{-1} M_\odot$ , while those Rockstar halos with parent ID equal to the ID of a given cluster halo are regarded as its substructure. We put a mass cut of  $10^{12} h^{-1} M_\odot$  on the substructure mass,  $M_{\text{sub}}$ , excluding those substructures with masses smaller than this mass-cut, regarding them poorly resolved in the simulations (Gao et al. 2011).

To find the filaments from the cluster halos with the adapted MST technique, we first apply the friends-of-friends (FOF) group finder with a linking length of  $20.4 h^{-1} \text{Mpc}$  to the spatial distributions of the cluster halos. The choice of this specific linking length is made through investigating the number of the filaments,  $N_{\text{fil}}$ , against the variation of the linking length  $l_p$  and determining the value of  $l_p$  that maximizes  $N_{\text{fil}}$ . Each of the

identified FoF groups represents a network system in which the member cluster halos are within the realm of gravitational influence from one another. Starting from the position of a member halo located in the group center (Alpaslan et al. 2014), we find its nearest member halo, connect the two halos by a straight line, and repeat the same process till all of the member halos are connected to construct a MST for each FoF group. Then, through pruning each MST at the level of  $p = 3$ , we identify a filamentary connection that stands out with the most linear pattern. A detailed description of the adapted MST algorithm and its pruning process, see Shim & Lee (2013) and Alpaslan et al. (2014).

Each identified filamentary network of the cluster halos, which we will call simply a filament from here on, corresponds to a site where the tidal field peaks both in its strength and its degree of anisotropy on the cluster scale. Suppose that a cluster halo is found to reside in a filament. The strongest tidal influence that this cluster halo receives is from the other member cluster halos belonging to the same filament. Hence, the substructure abundance of this cluster halo is naturally expected to depend on the physical properties of the host filament such as its richness, spatial extent, shape and etc.

In Section 5.3, we will statistically examine how the substructure abundance of a member cluster halo depends on the *specific size* of its host filament,  $\tilde{S}$ , which is defined as the spatial extent of a filament divided by its node number, where a node number refers to the number of its member cluster halos. A filament forms in a region where the tidal field has two positive and one negative eigenvalues. The gravitational stretch of matter distribution will occur along the direction of the eigenvector corresponding to the negative eigenvalue (the minor principal axis) while the other two (major and intermediate) principal axes coincide with the directions for the gravitational collapse (see Forero-Romero et al. 2009, and references therein). A large-scale coherence of the tidal fields in the orientations of their minor principal axes will lead to the formation of a spatially extended rich filament. We will adopt the specific sizes of the filaments as a practical measure of this *orientation coherence* of the tidal field. We will adopt the

following formula given by Shim & Lee (2013) to determine the specific size,  $\tilde{S}$ , of each filament.

$$\tilde{S} = \frac{1}{N_{\text{node}}} \left[ (\Delta x)^2 + (\Delta y)^2 + (\Delta z)^2 \right]^{1/2}, \quad (5.1)$$

where  $\Delta x$ ,  $\Delta y$  and  $\Delta z$  represent the ranges of the three Cartesian coordinates of the member cluster halos.

Figure 5.1 compares two identified filaments which differ from each other in their specific sizes. As can be seen, the filament with larger specific size is more elongated and straight than the other filament with smaller specific sizes. Figure 5.2 plots the number counts of the filaments,  $N_{\text{fil}}$ , as a function of their node numbers,  $N_{\text{node}}$ , showing a sharp decrement of the filament abundance with the increment of the node number. Those filaments which have less than four nodes are excluded from our analysis since the filaments with  $N_{\text{node}} \leq 3$  may have biased distribution of the specific sizes due to the small number of nodes.

### 5.3 Substructure Abundance of the Cluster Halos in the Filaments

Now that the specific sizes of the filaments with  $N_{\text{node}} \geq 4$  are determined, we classify the cluster halos into five samples by the specific sizes of their host filaments and examine the mass distributions for each sample. The top panel of Figure 5.3 shows the number counts of the cluster halos belonging to each sample as a function of mass, revealing that the five samples have different mass distributions. To avoid any false signal of  $N_{\text{sub}}-\tilde{S}$  correlation caused by the difference in the mass distributions, we deliberately exclude those cluster halos whose masses fall out of the common range to tally the mass distributions of the five samples. The bottom panel of Figure 5.3 shows the same as the top panel but after the mass-synchronization process.

Let  $N_{\text{sub}}^{\alpha}$  represent the number of the substructures in the  $\alpha$ -th cluster halo belonging to a given mass-synchronized sample which contains a total of  $N_{\text{host}}$  cluster halos. Taking the average of the substructure number counts over the cluster halos belonging

to each mass-synchronized sample as  $\langle N_{\text{sub}} \rangle \equiv \sum_{\alpha} N_{\text{sub}}^{\alpha} / N_{\text{host}}$ , we investigate how the mean number of the substructures of the cluster halos changes with the specific sizes of the host filaments. The top panel of Figure 5.4 plots  $\langle N_{\text{sub}} \rangle$  versus  $\tilde{S}$  with the Bootstrap errors, from which one can witness an obvious trend that  $\langle N_{\text{sub}} \rangle$  increases as the decrement of  $\tilde{S}$ . Counting only those massive substructures with  $M_{\text{sub}}/M_{\text{host}} \geq 0.1$ , we repeat the same analysis, the result of which is shown in the bottom panel of Figure 5.4. As can be seen, the massive substructures also retains a signal of the  $N_{\text{sub}}-\tilde{S}$  anti-correlation, albeit the errors become larger.

For the results shown in Figure 5.4, we include all of the identified filaments, regardless of their node numbers. However, the node number,  $N_{\text{node}}$ , of a filament can contribute to the  $N_{\text{sub}}-\tilde{S}$  anti-correlation since both of  $N_{\text{sub}}$  and  $\tilde{S}$  depend on  $N_{\text{node}}$ . The specific size of a filament obviously depends on its node number by its definition. The abundance of the substructures of a cluster halo is dependent on the node number of its host filament since a cluster halo hosted by a filament with higher  $N_{\text{node}}$  should be exposed to stronger tidal effect from more neighbor halos in the same filament.

To single out the effect of the filamentary tidal influence on the substructure abundance of the cluster halos, we now fix the node number of a filament at a certain value and reinvestigate if  $N_{\text{sub}}$  still retains its anti-correlation with  $\tilde{S}$ . Using those filaments whose node numbers are equal to a fixed value, we reclassify them into five subsamples according to their values of  $\tilde{S}$  and resynchronize their mass distributions in a similar manner, and calculate  $\langle N_{\text{sub}} \rangle$  for each subsample. Figures 5.5-5.6 display the results for the cases of  $N_{\text{node}} = 4$  and 5, respectively. Noting, that for the cases of the higher node numbers, the results suffer from large errors due to the small number of the filaments with more than five nodes, we consider only the two case of  $N_{\text{node}} = 4$  and 5. As can be seen, even when the node number is fixed, the mean substructure abundance of the cluster halos on average exhibits a clear signal of anti-correlation with the specific sizes of the host filaments. Although the anti-correlation signal becomes weak at fixed node number for the massive substructure case of  $M_{\text{sub}}/M_{\text{host}} \geq 0.1$ , the results shown in Figures 5.5-5.6 reveal that the dependence of  $N_{\text{sub}}$  on the number of the cluster halos

in the filaments is not the main contribution to the observed anti-correlation signal.

Now that the substructure abundance of the cluster halos in the filaments is found to be anti-correlated with the specific sizes of the filaments, we would like to understand what originates this anti-correlation. The usual suspect is the assembly bias, i.e., the difference in the formation epochs of the cluster halos as for the case of the galactic halos (Garaldi et al. 2017). If at fixed mass scale the cluster halos in the filaments with larger  $\tilde{S}$  have a tendency to form earlier, it could explain the observed  $N_{\text{sub}}-\tilde{S}$  anti-correlation since those halos formed earlier are known to have on average less substructures. Figure 5.7 plots the number counts of the cluster halos as a function of their formation epochs,  $z_{\text{form}}$ . For the majority of the cluster halos, the formation epochs lie in the range of  $0.2 \leq z_{\text{form}} \leq 0.8$ .

We compute the mean formation epochs,  $\langle z_{\text{form}} \rangle$ , of the cluster halos belonging to each subsample at fixed node number,  $N_{\text{node}} = 4$  and 5, and display the result in Figure 5.8. As can be seen, the mean formation epochs of the clusters seem to depend only quite weakly on the specific sizes of the host filaments, which indicates that the observed signal of the anti-correlation between  $N_{\text{sub}}$  and  $\tilde{S}$  should not be produced by the dependence of  $N_{\text{sub}}$  on  $z_{\text{form}}$ . Notwithstanding, to eliminate completely any possible contribution of the  $\tilde{S}-z_{\text{form}}$  correlation to the detected signal, we narrow down the range of the formation epochs and reinvestigate the  $\tilde{S}-N_{\text{sub}}$  correlation. From each of the five sample, selecting only those cluster halos whose formation epochs fall in a narrow  $z_{\text{form}}$ -interval with a width of  $\Delta z_{\text{form}} = 0.1$  to make a subsample and synchronizing the mass distributions of the five subsamples, we remeasure  $\langle N_{\text{sub}} \rangle$  as a function of  $\tilde{S}$ , the results of which are displayed in Figures 5.9-5.16. As can be seen, narrowing down the range of the formation epochs does not erase the anti-correlation signal. We also test the survival of the anti-correlation signal against fixing both of  $N_{\text{node}}$  and  $z_{\text{form}}$ , the result is shown Figure 5.17 which confirms the robustness of the  $N_{\text{sub}}-\tilde{S}$  anti-correlation.

Motivated by our detection of the  $N_{\text{sub}}-\tilde{S}$  anti-correlation, we would like to know if and how the spatial distributions of the substructures in the cluster halos depend on the specific sizes of the host filaments. Let  $r$  be the comoving radial distance of a

substructure from the center of mass of its host halo whose virial radius is  $r_{\text{vir}}$ . Binning the values of the ratios,  $r/r_{\text{vir}}$ , we count the numbers of the substructures at each  $r/r_{\text{vir}}$  bin,  $\Delta N_{\text{sub}}(r/r_{\text{vir}})$ , for each cluster halo. Then, we compute the cumulative distribution of the number counts of the substructures and then take its average over the cluster halos to determine,  $\langle N_{\text{sub}}(\leq r/r_{\text{vir}}) \rangle$ , which is plotted in Figure 5.18. The red (blue) solid line corresponds to the case of the cluster halos whose host filaments have the top (bottom) 10% largest (smallest) specific sizes. The blurred envelopes of the solid lines represent the corresponding bootstrap errors. As can be seen, when all substructures are counted (top panel), the top and the bottom 10% cases make a notable difference only at the large radial distance section ( $r \geq 0.6r_{\text{vir}}$ ). Whereas, when only the massive substructures are counted, the opposite trend is found at the small radial distance section ( $r < 0.6r_{\text{vir}}$ ): the cluster halos belonging to the filaments with bottom 10% smallest specific sizes have more massive substructures at shorter radial distances.

## 5.4 Summary and Discussion

Given that the substructures of the cluster halos form through the satellite infall and matter accretion and that the majority of the cluster halos reside in the large-scale filaments which are the reservoirs of the satellites and matter particles, the formation and evolution of the substructures of the cluster halos are expected to depend on the physical properties of the host filaments. We have investigated the correlations between the substructure abundance of the cluster halos and the specific sizes of the host filaments, by utilizing the datasets from the Big MDPL (Klypin et al. 2016). The filaments that comprise the cluster halos as nodes have been identified via the adapted MST algorithm (Colberg 2007) and their specific sizes have been determined as their spatial extents per node (Shim & Lee 2013). If the tidal fields are coherent over large scales in their orientations of the minor principal axes, then the filaments formed through the gravitational stretch of matter along the minor principal axes of the tidal fields are expected to have large specific sizes. Hence, the orientation coherence of the tidal field on the cluster scale can be practically quantified by the specific sizes of the

filaments.

A signal of anti-correlation between the substructure abundance of the member cluster halos and the specific sizes of their host filaments has been detected (see Figure 5.4). Those cluster halos that constitute the filaments with smaller specific sizes have turned out to contain on average more substructures. This anti-correlation signal has been found robust against narrowing down the range of the formation epochs of the cluster halos (see Figures 5.9-5.17 as well as against fixing the node numbers of the filaments (see Figures 5.5-5.6), which implies that the most dominant role in the generation of this anti-correlation should not be the difference in the tidal strength among the filaments with different specific sizes.

We explain that the anti-correlation should be caused by the obstructed infall of satellites onto the cluster halos in the filaments with large specific sizes due to the development of the tangential velocities of the satellites in the confined plane perpendicular to the elongated axes of the filaments: When a region evolves to form a filament through its gravitational compression along the major and intermediate axes and the gravitational dilation along the minor principal axis of the local tidal field, the satellites and matter particles located in the region develop their inward velocities mainly in the plane spanned by the major and the intermediate principal axes. In other words, inside a filament, the velocities of satellites and matter particles grow in the directions perpendicular to the elongated axis of the filament. Once a filament forms, the satellite infall and matter accretion into the cluster halos that reside in the filament should be obstructed since their velocities in the filaments are perpendicular to the direction toward the cluster halos. The more coherent the minor principal axes of the tidal fields are in their orientations over large scales, the larger specific sizes the filaments would have and thus the more severely the satellite infall and matter accretion should be obstructed. For the cluster halos residing in the filaments with small specific sizes, the satellite and matter particles can develop radial velocities at non-negligible level in the direction parallel to the elongated axes of the filaments.

We have also determined the cumulative number counts of the substructures, as a

function of their radial distances from the cluster centers (Figure 5.18). The difference in the substructure abundance between the cluster halos in the filaments with large and small specific sizes has been found to disappear in the small distance section  $r \leq 0.6r_{\text{vir}}$  but to show up in the large distance section  $r > 0.6r_{\text{vir}}$ . Given that a substructure located at the large (small) distances form through relatively recent (early) infall of a satellite, this result implies that the obstruction of the satellite infall and matter accretion becomes effective only after the filamentary connection with high orientation coherence is established. In addition, we have noted that for the case of the cluster halos contained in the filaments with large (small) specific sizes the massive substructures with  $M_{\text{sub}} \geq 0.1M_{\text{host}}$  are placed in the small (large) distance section. We speculate that the origin of this phenomenon is the difference between the tidal stripping effect of the cluster halos embedded in the filaments with small and large specific sizes. In the former (latter) the massive substructures are more (less) severely stripped off in the inner region of their hosts.

Our result is consistent with the finding of Garaldi et al. (2017) that the galactic halos belonging to "prominent" filaments possess on average less substructures than those located at the junction of multiple secondary filaments. They used the thickness as a criterion for the distinction of a prominent filament from a secondary one. According to their qualitative description, if a filament is straight and thicker than the size of a galactic halo, it is the prominent one where the development of the tangential velocities obstruct the satellite infall and matter accretion onto the member galactic halos. On the cluster scale, however, most of the filaments are as thick as the halo size. Therefore, the thickness cannot be used to determine whether a given filament is prominent or secondary. In the current work dealing with the cluster halos, we have made a quantitative distinction between prominent and secondary filaments in terms of their specific sizes and detected a robust signal of the anti-correlation between the substructure abundance of the cluster halos and the specific sizes of the host filaments, which implies that the orientation coherence of the surrounding tidal field reflected by the specific sizes of the filaments plays a key role in regulating the growth of the cluster

halos by obstructing the satellite infall and matter accretion.

Yet, to prove the claim that the satellite infall and matter accretion onto the cluster halos in the filaments with large specific sizes are indeed obstructed by the development of the tangential velocities in the plane perpendicular to the filament axes, it will be necessary to investigate how strongly the velocities of the satellites before falling into the cluster halos and the elongated axes of the filaments are correlated and how the correlation strength varies with the specific sizes of the filaments. In line with this claim, it will be also interesting to figure out what physical properties of the cluster halos other than their substructure abundance depend on the specific sizes of the filaments, which will allow us to have a better understanding of the effect of the orientation coherence of the large-scale tidal field on the growth of the cluster halos. Our future work will be in this direction.

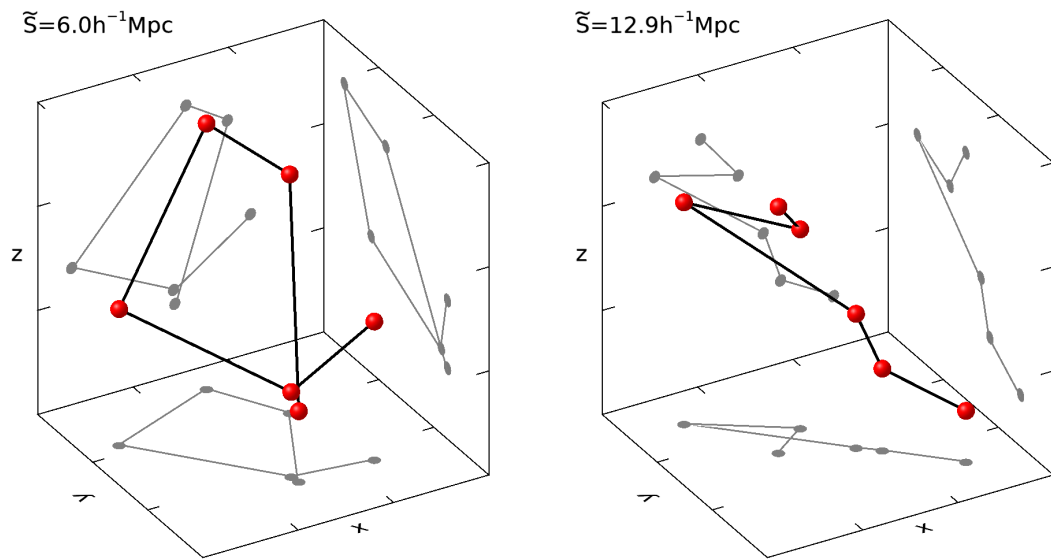


**Figure 5.1.** Configurations of the cluster halos in the filaments for two different cases of the specific sizes.

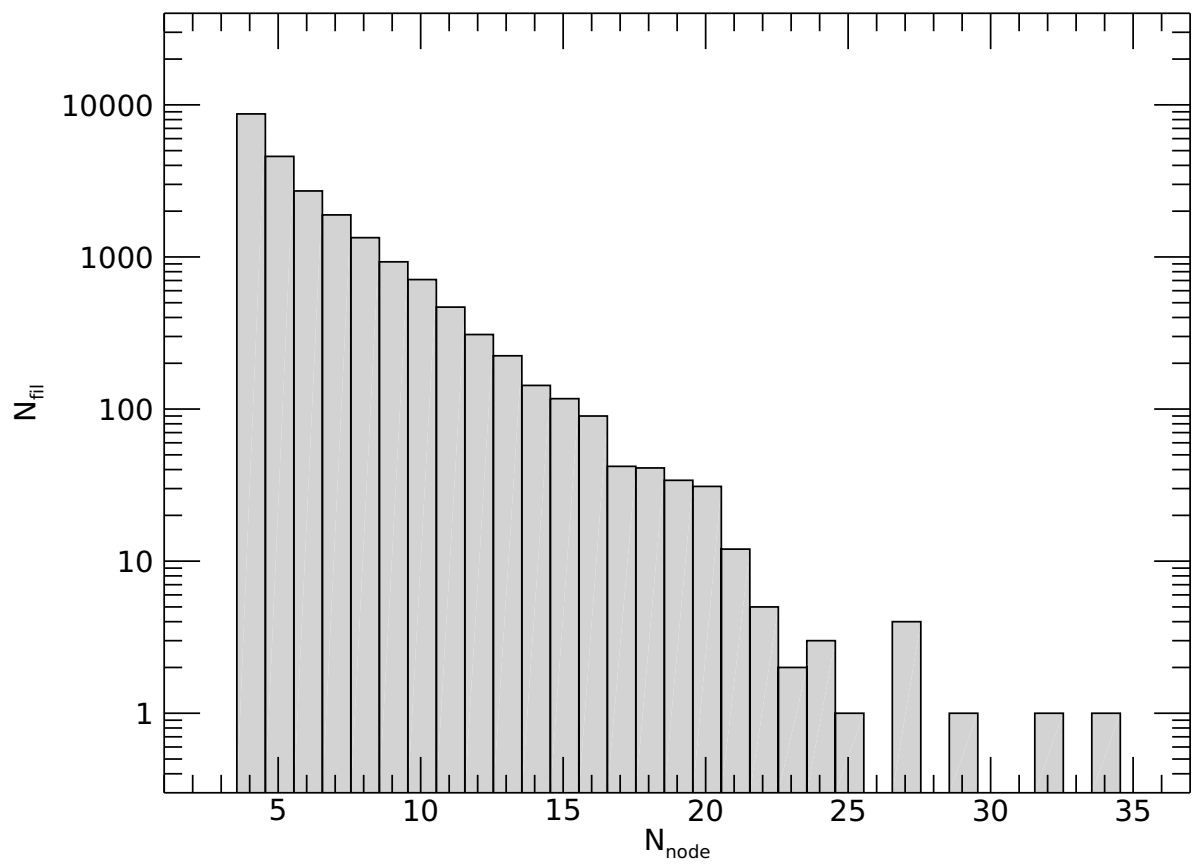


**Figure 5.2.** Number counts of the filaments as a function of the node numbers.

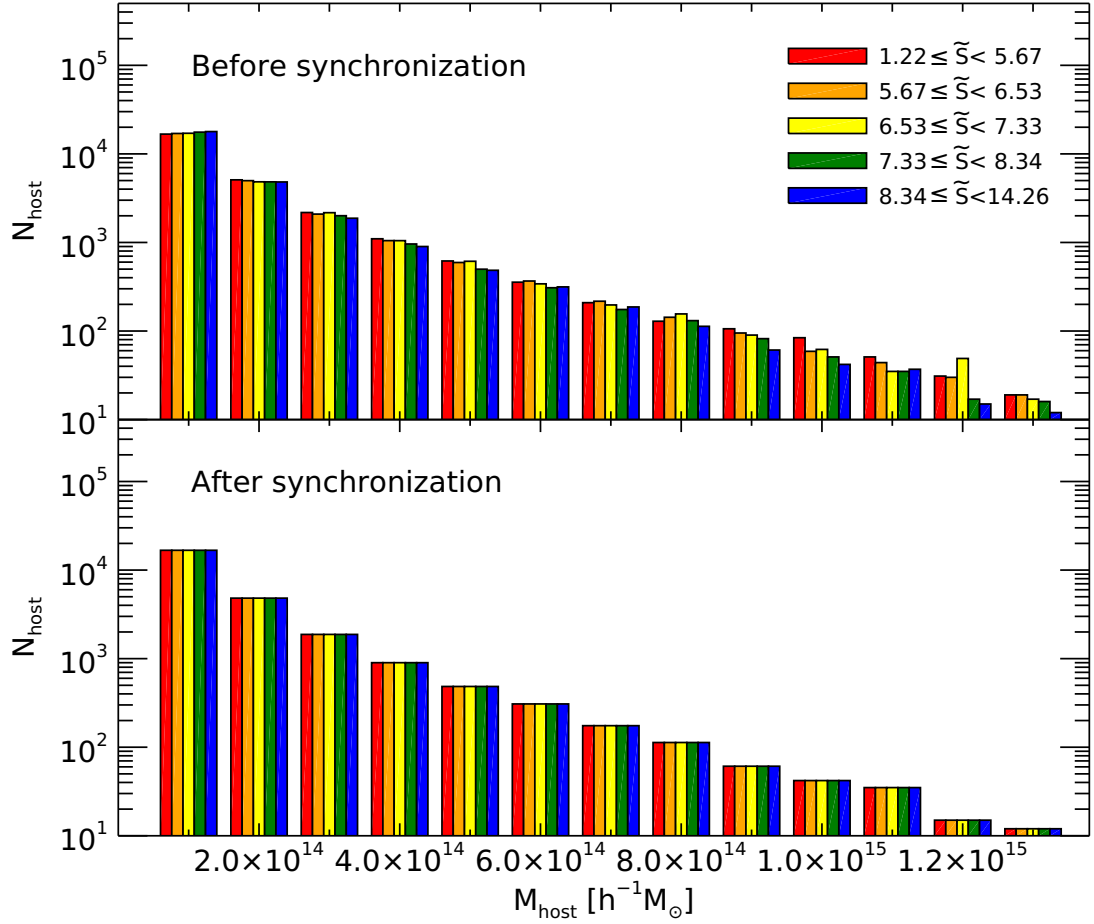


**Figure 5.3.** Number counts of the cluster halos contained in the filaments as a function of their masses for five samples before and after the mass-synchronization process in the top and bottom panels, respectively. The specific sizes are in unit of  $h^{-1}\text{Mpc}$ .

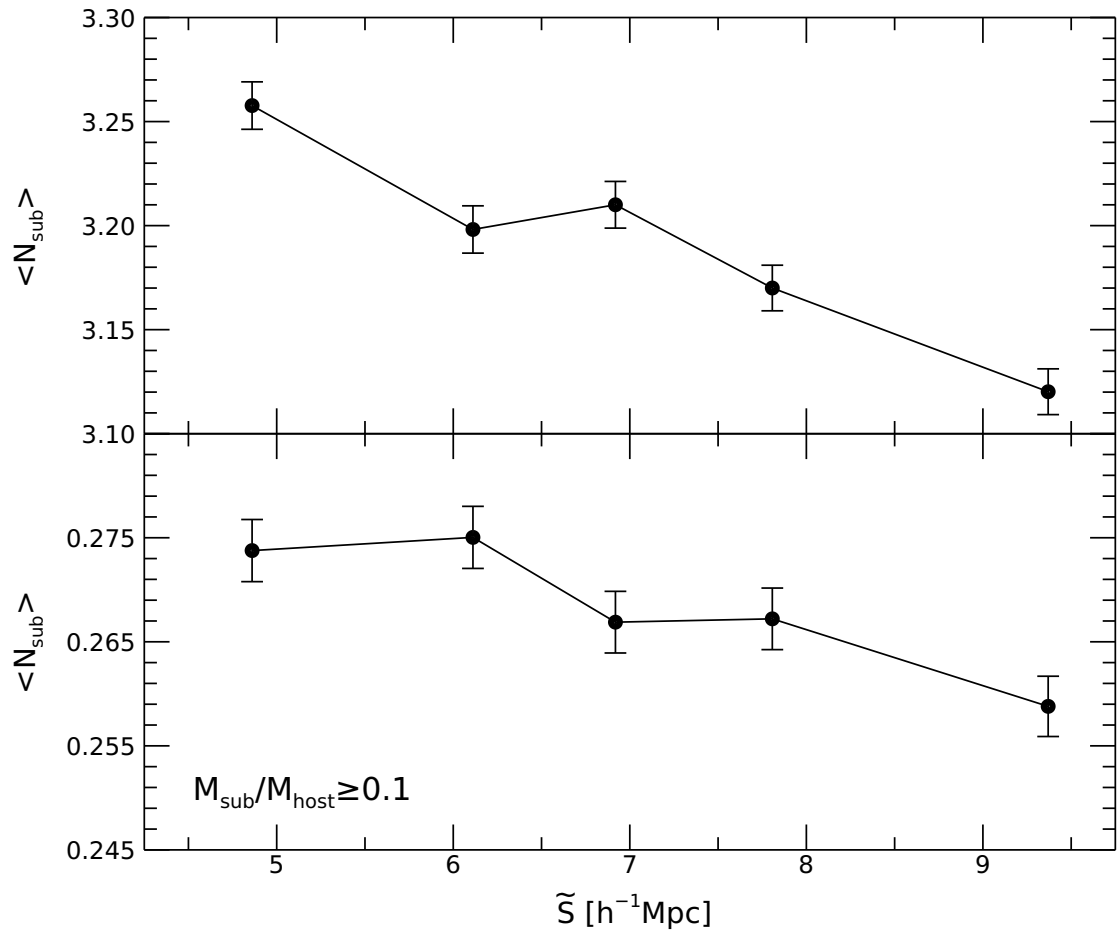


**Figure 5.4.** Mean substructure abundance of the cluster halos versus the specific sizes of their host filaments.

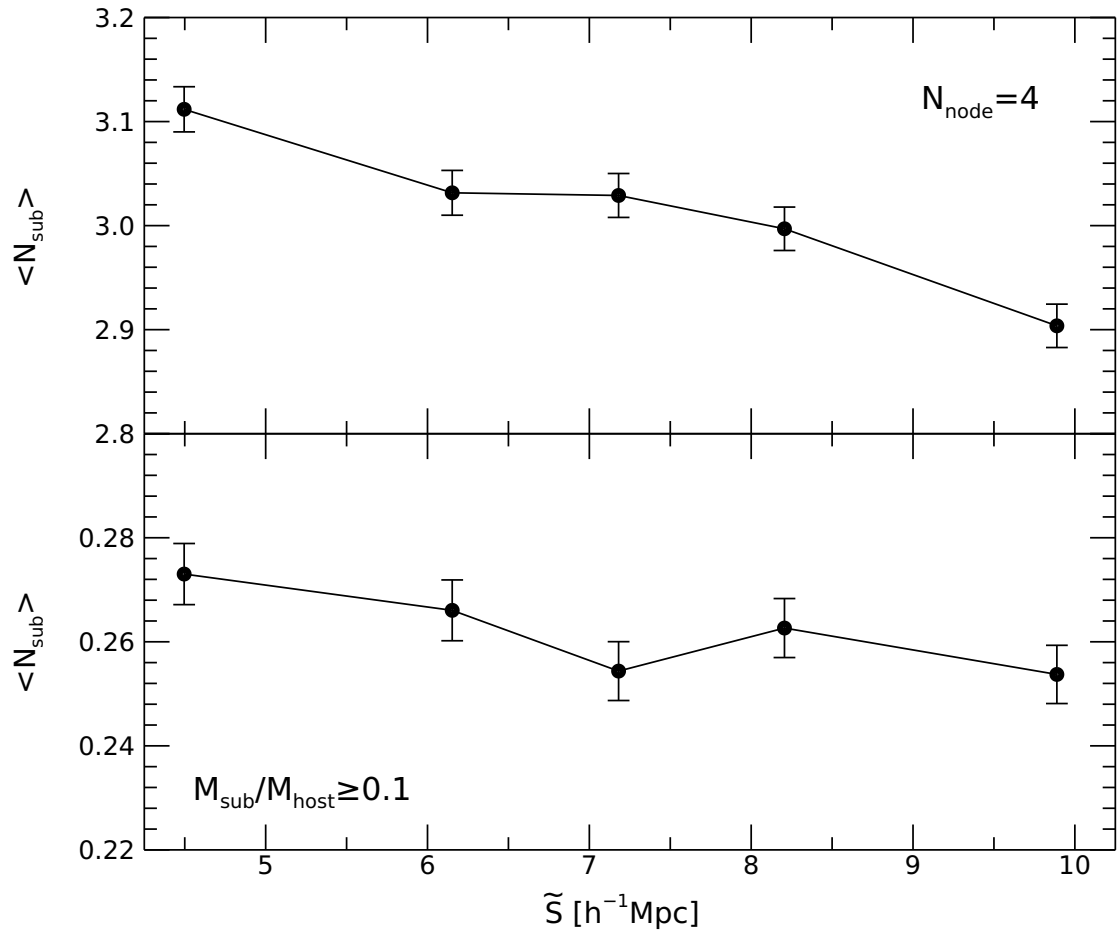


**Figure 5.5.** Same as Figure 5.4 but for the case that only those clusters whose host filaments have a fixed node number of  $N_{\text{node}} = 4$ .

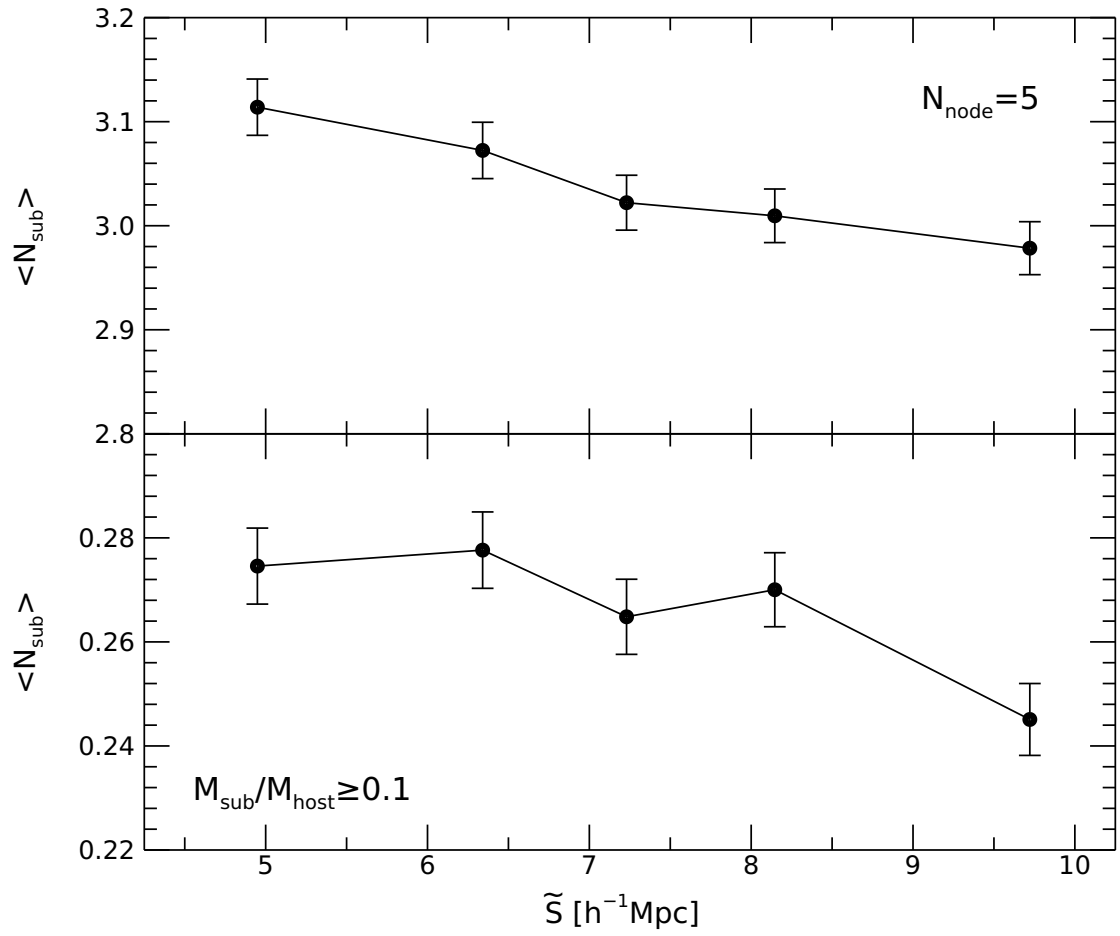


**Figure 5.6.** Same as Figure 5.5 but for the case of  $N_{\text{node}} = 5$ .

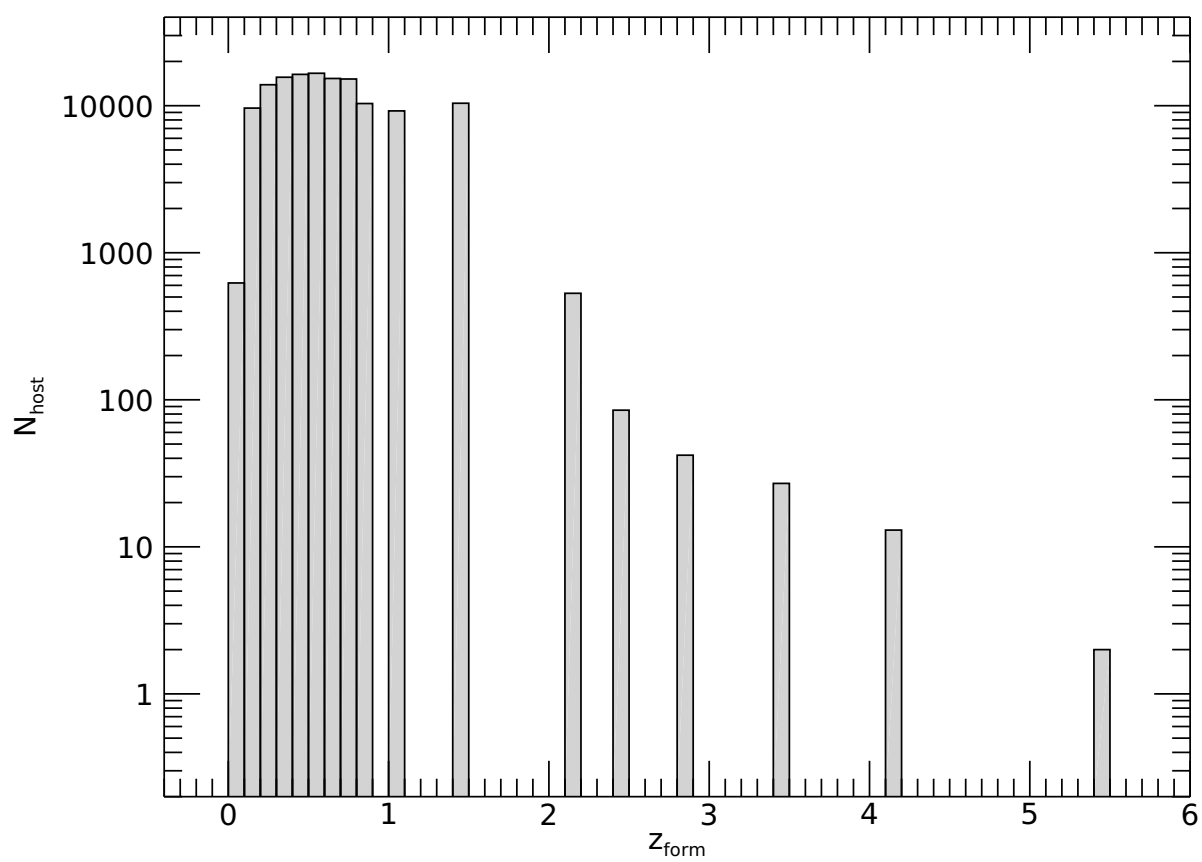


**Figure 5.7.** Number distribution of the cluster halos as a function of their formation epochs.

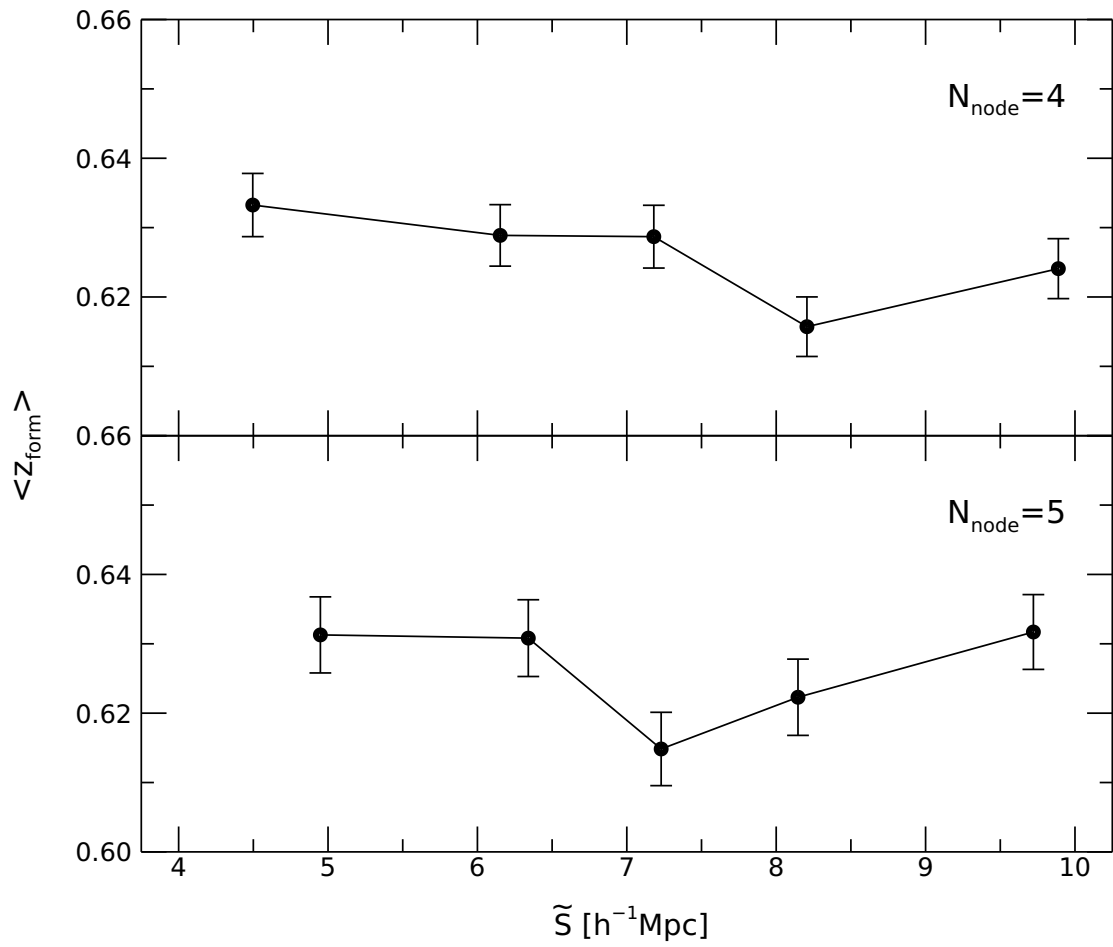


**Figure 5.8.** Mean formation epochs of the cluster halos vs. the specific sizes of their host filaments.

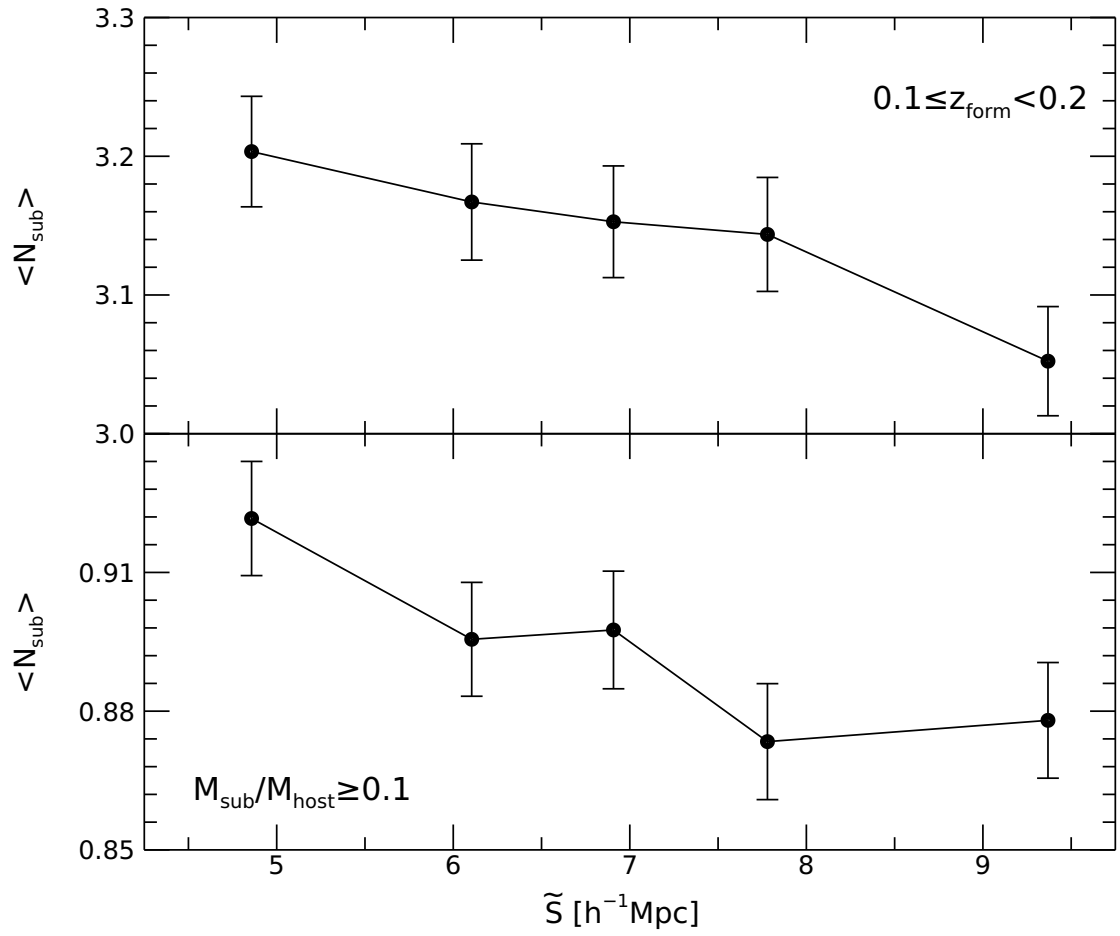


**Figure 5.9.** Same as Figure 5.4 but for the case of only those clusters with formation epochs in the narrow range of  $0.1 \leq z_{\text{form}} < 0.2$ .

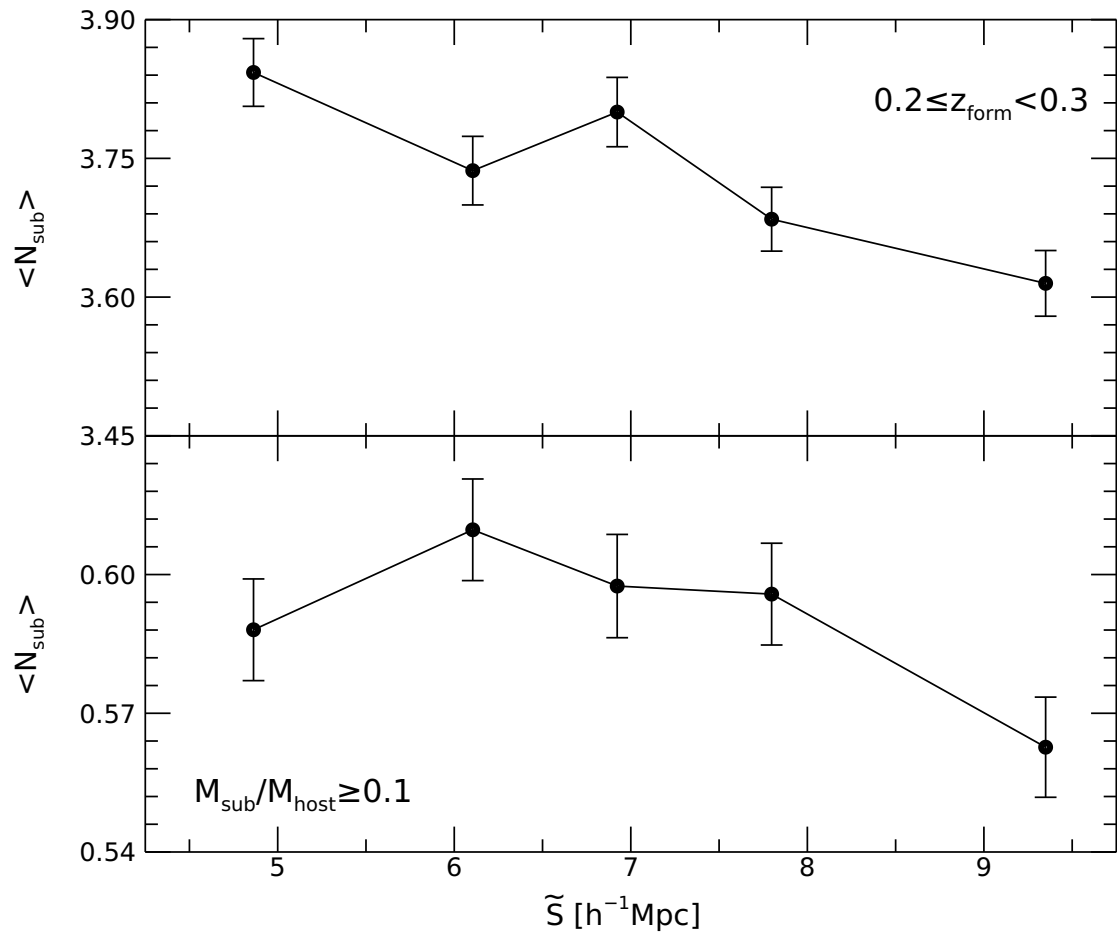


**Figure 5.10.** Same as Figure 5.9 but for the case of  $0.2 \leq z_{\text{form}} < 0.3$ .

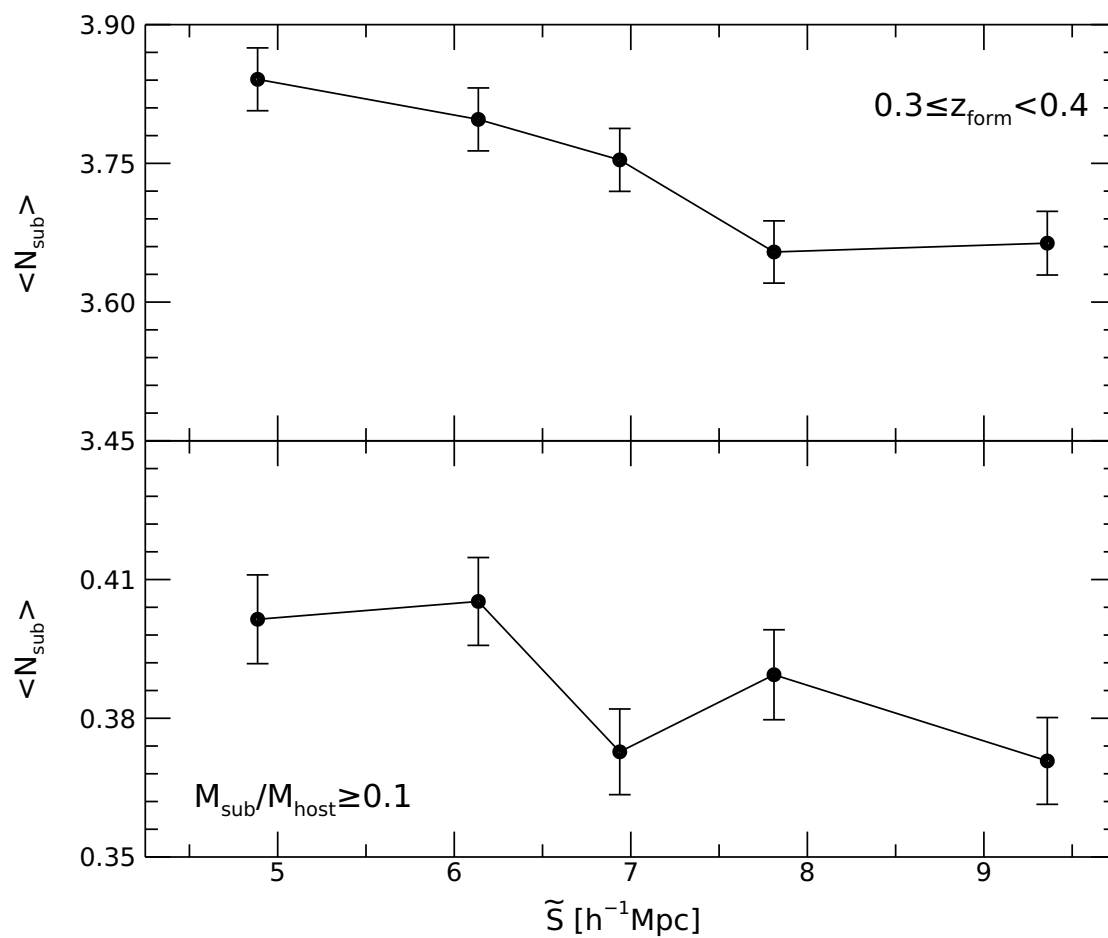


**Figure 5.11.** Same as Figure 5.9 but for the case of  $0.3 \leq z_{\text{form}} < 0.4$ .

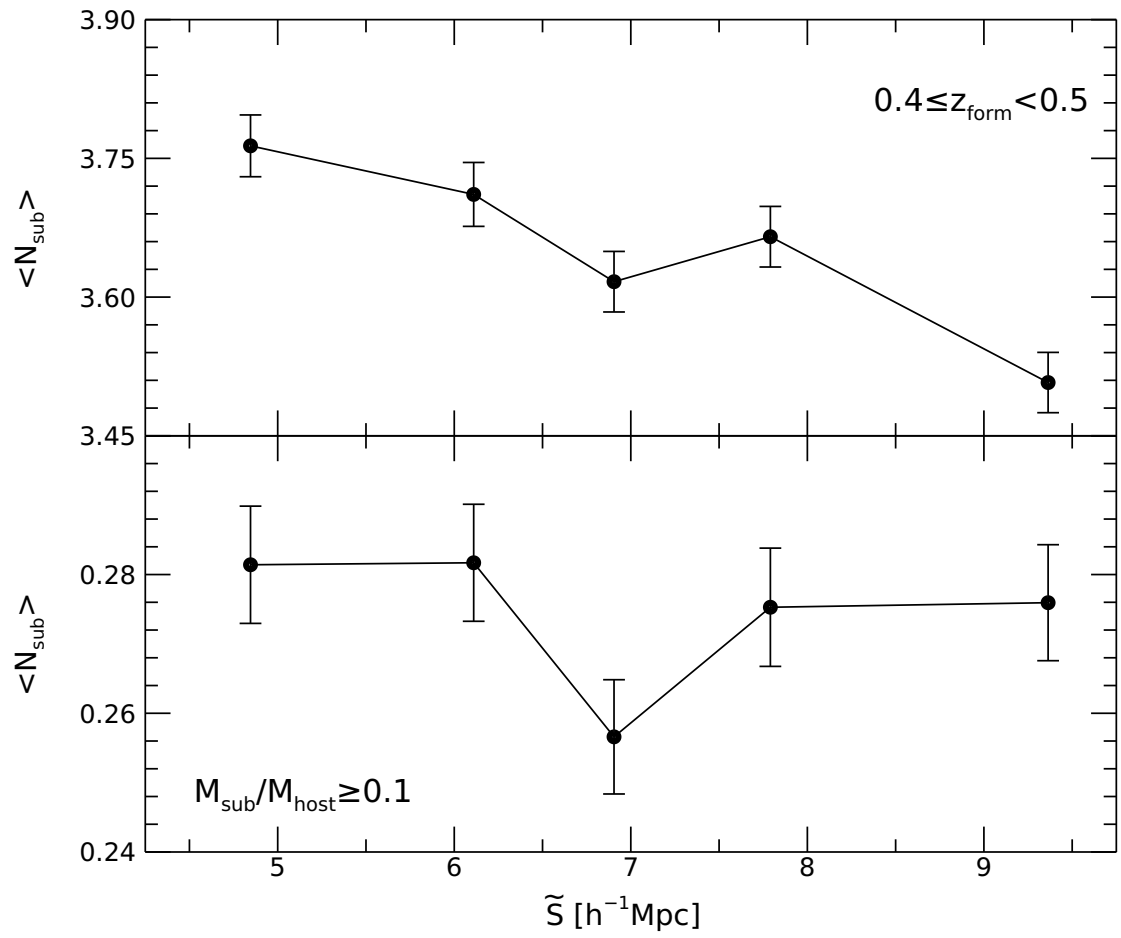


**Figure 5.12.** Same as Figure 5.9 but for the case of  $0.4 \leq z_{\text{form}} < 0.5$ .

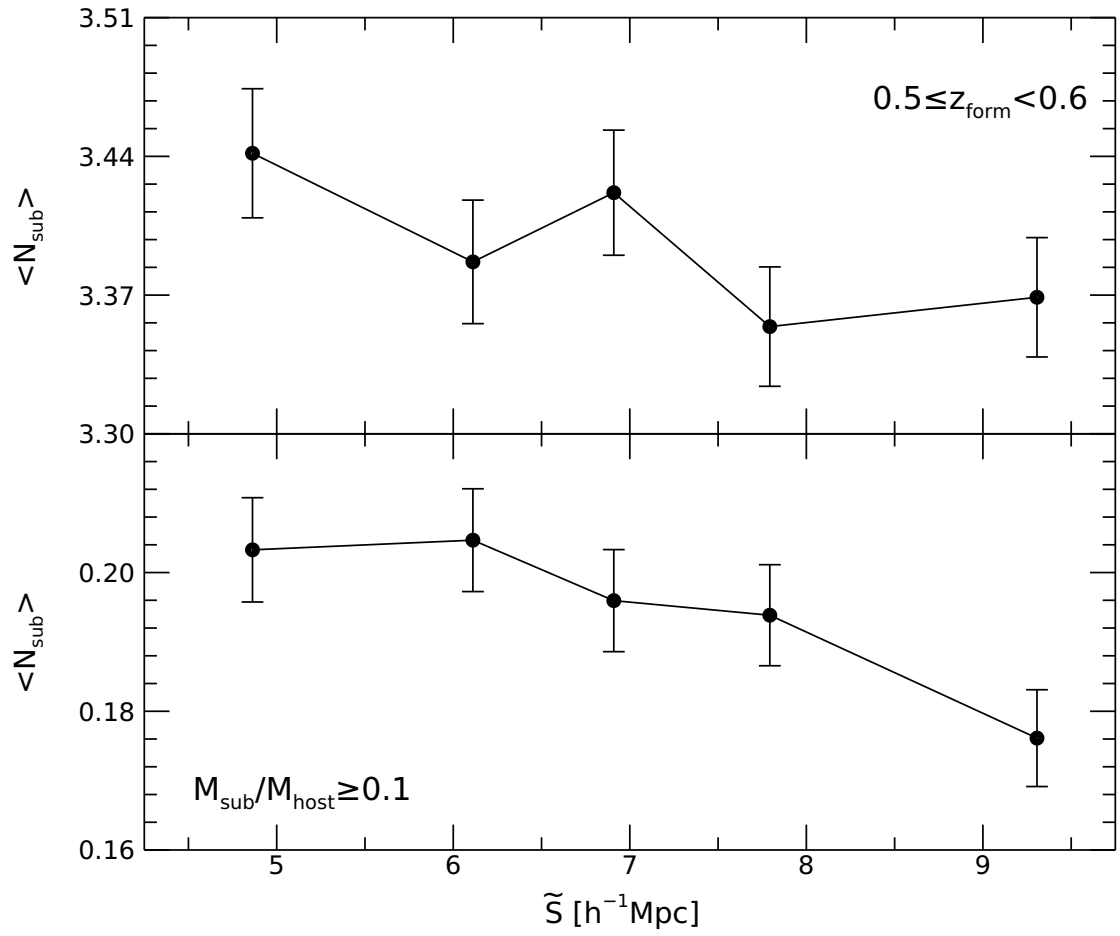


**Figure 5.13.** Same as Figure 5.9 but for the case of  $0.5 \leq z_{\text{form}} < 0.6$ .

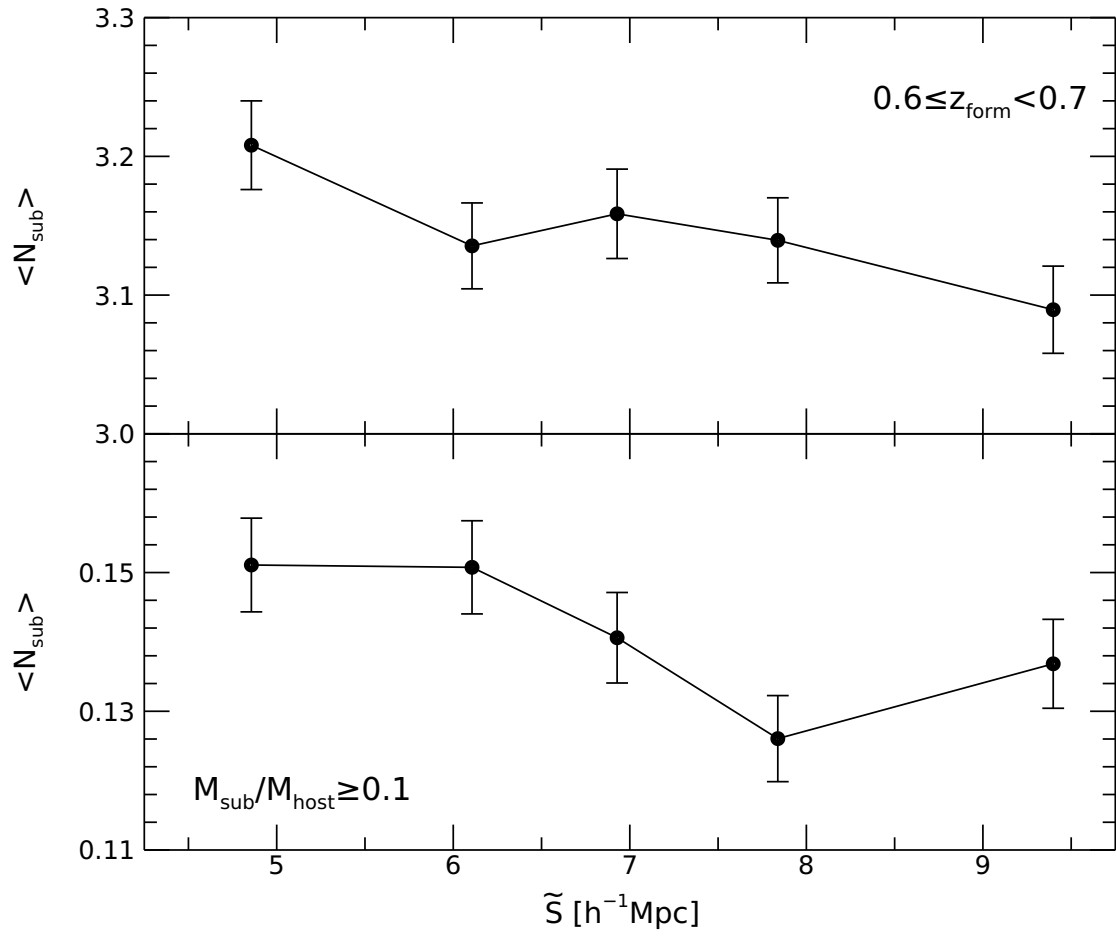


**Figure 5.14.** Same as Figure 5.9 but for the case of  $0.6 \leq z_{\text{form}} < 0.7$ .

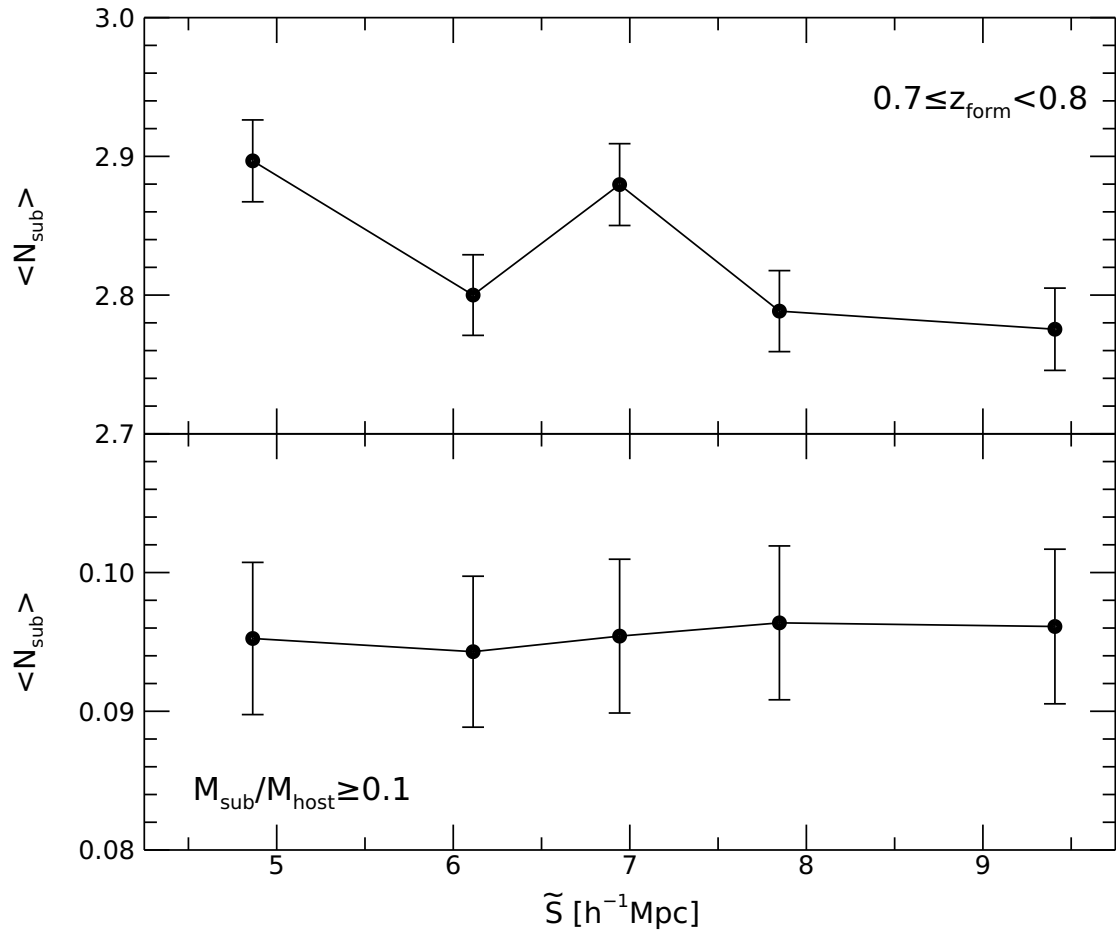


**Figure 5.15.** Same as Figure 5.9 but for the case of  $0.7 \leq z_{\text{form}} < 0.8$ .

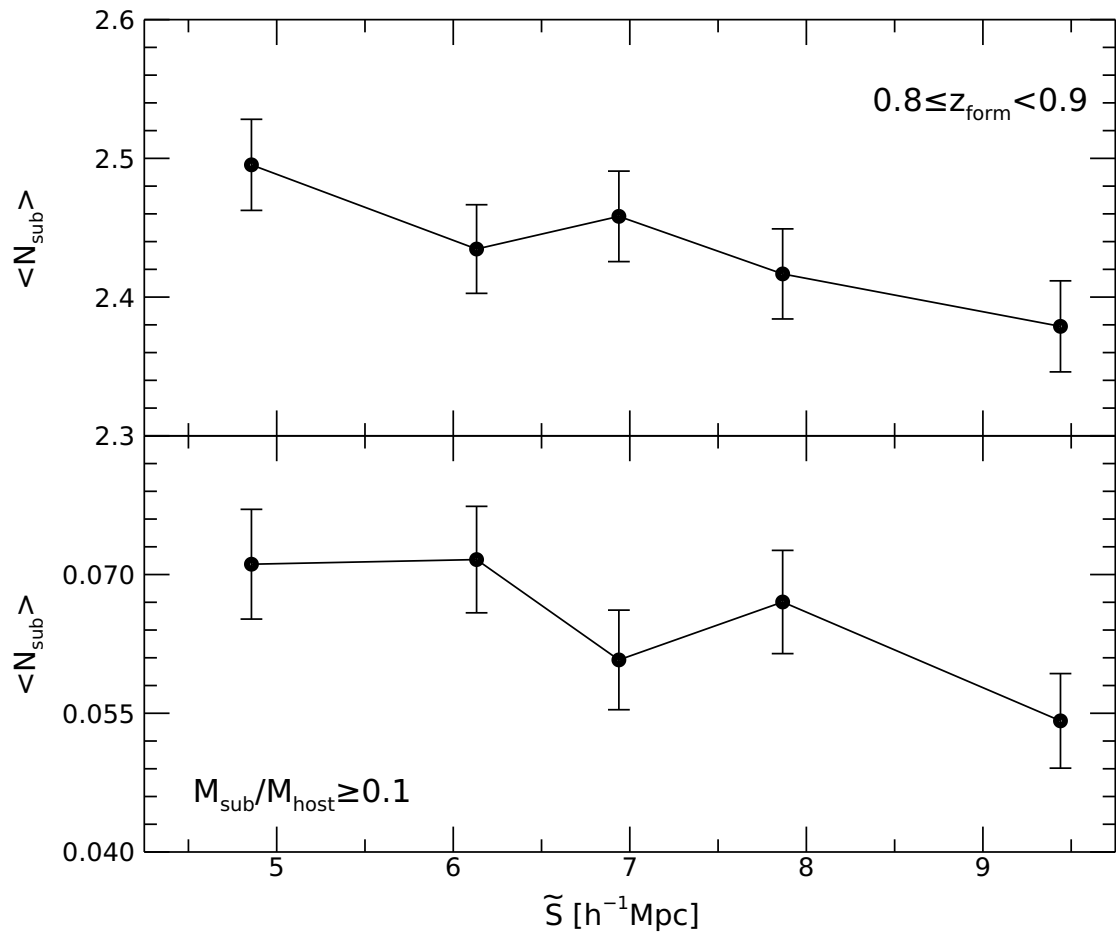


**Figure 5.16.** Same as Figure 5.9 but for the case of  $0.8 \leq z_{\text{form}} < 0.9$ .

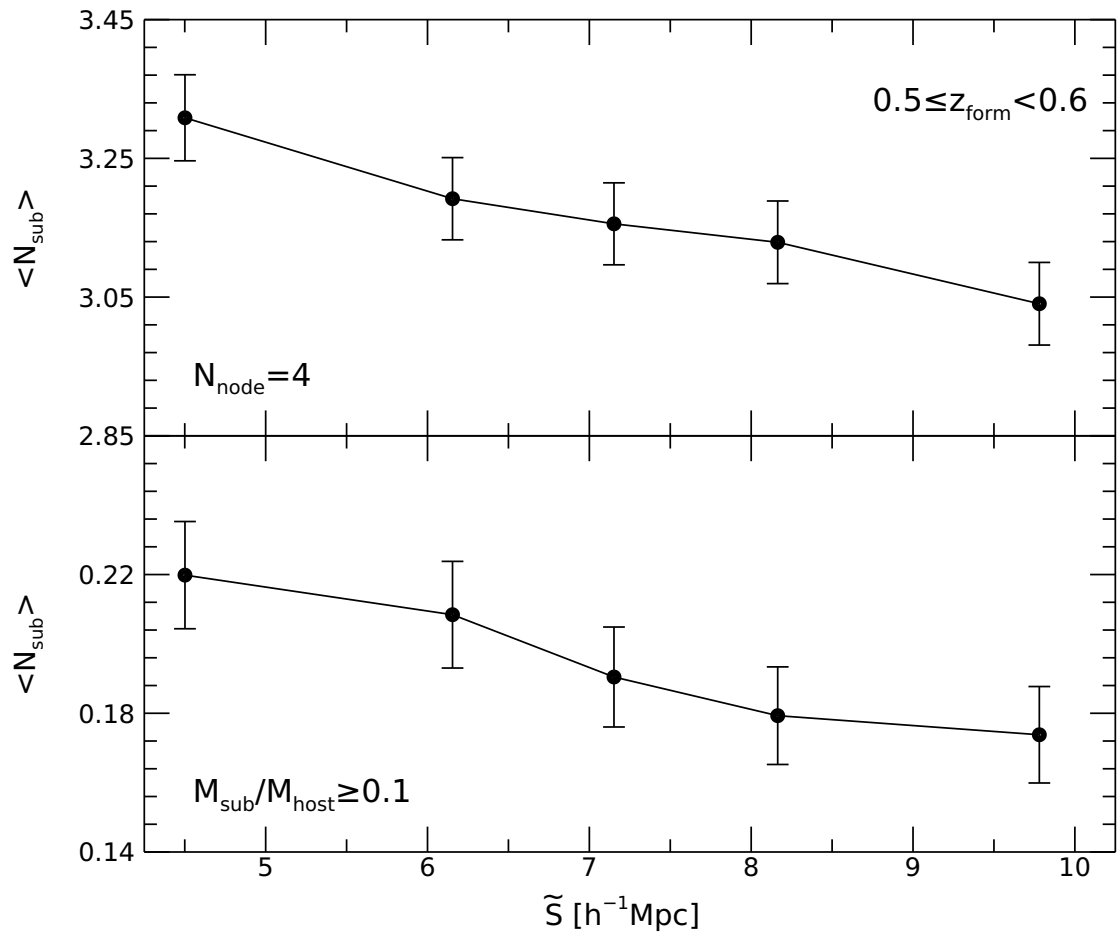


**Figure 5.17.** Same as Figure 5.4 but for the case of  $0.5 \leq z_{\text{form}} < 0.6$  and  $N_{\text{node}} = 4$ .

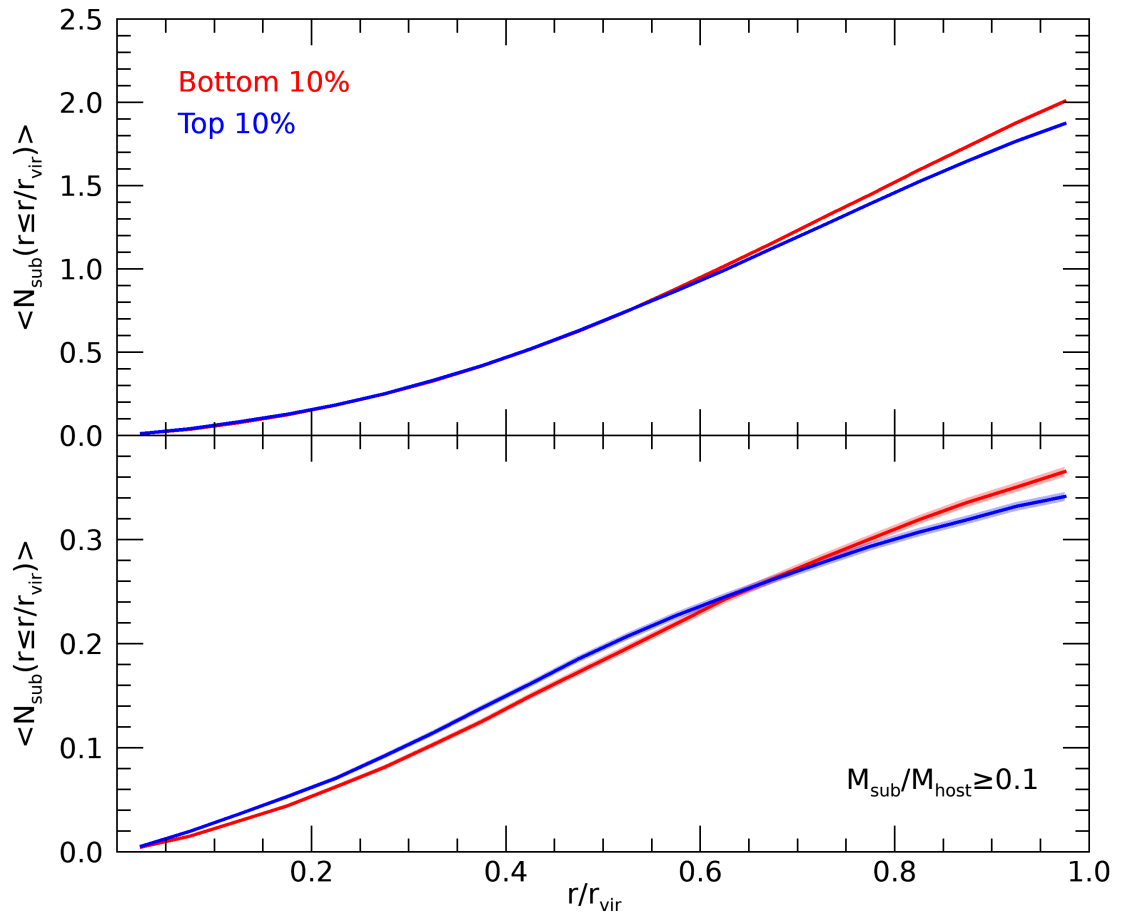


**Figure 5.18.** Cumulative number counts of the substructures in the cluster halos as a function of their rescaled radial distances,  $r/r_{\text{vir}}$  for the case that the host filaments have the top 10% largest (blue lines) and the bottom 10% smallest specific sizes (red lines), respectively.



# Bibliography

- Alpaslan, M., Robotham, A. S. G., Driver, S., et al. 2014, MNRAS, 438, 177
- Behroozi, P. S., Wechsler, R. H., & Wu, H.-Y. 2013, ApJ, 762, 109
- Borzyszkowski, M., Porciani, C., Romano-Díaz, E., & Garaldi, E. 2017, MNRAS, 469, 594
- Chirivì, G., Suyu, S. H., Grillo, C., et al. 2017, arXiv:1706.07815
- Colberg, J. M. 2007, MNRAS, 375, 337
- Contini, E., & Kang, X. 2015, MNRAS, 453, L53
- Croft, R. A. C., di Matteo, T., Khandai, N., et al. 2012, MNRAS, 425, 2766
- De Lucia, G., Kauffmann, G., Springel, V., et al. 2004, MNRAS, 348, 333
- Fakhouri, O., & Ma, C. P. 2009, MNRAS, 394, 1825
- Fakhouri, O., & Ma, C. P. 2010, MNRAS, 401, 2245
- Forero-Romero, J. E., Hoffman, Y., Gottlöber, S., Klypin, A., & Yepes, G. 2009, MNRAS, 396, 1815
- Gao, L., & White, S. D. M. 2007, MNRAS, 377, L5
- Gao, L., Frenk, C. S., Boylan-Kolchin, M., et al. 2011, MNRAS, 410, 2309
- Gao, L., Navarro, J. F., Frenk, C. S., et al. 2012, MNRAS, 425, 2169

- Garaldi, E., Romano-Díaz, E., Borzyszkowski, M., & Porciani, C. 2017, arXiv:1707.01108
- Hahn, O., Porciani, C., Dekel, A., & Carollo, C. M. 2009, MNRAS, 398, 1742
- Hester, J. A., & Tasitsiomi, A. 2010, ApJ, 715, 342
- Jiang, F., & van den Bosch, F. C. 2017, MNRAS, 472, 657
- Klypin, A., Yepes, G., Gottlöber, S., Prada, F., & Heß, S. 2016, MNRAS, 457, 4340
- Lee, J. 2004, ApJ, 604, L73
- Libeskind, N. I., van de Weygaert, R., Cautun, M., et al. 2018, MNRAS, 473, 1195
- Mao, Y.-Y., Williamson, M., & Wechsler, R. H. 2015, ApJ, 810, 21
- Mao, T.-X., Wang, J., Frenk, C. S., et al. 2017, arXiv:1708.01400
- Natarajan, P., & Springel, V. 2004, ApJ, 617, L13
- Oguri, M., & Lee, J. 2004, MNRAS, 355, 120
- Planck Collaboration, Ade, P. A. R., Aghanim, N., et al. 2014, A&A, 571, A16
- Park, D., & Lee, J. 2009, MNRAS, 397, 2163
- Park, D., & Lee, J. 2009, MNRAS, 400, 1105
- Riebe, K., Partl, A. M., Enke, H., et al. 2013, Astronomische Nachrichten, 334, 691
- Schwinn, J., Jauzac, M., Baugh, C. M., et al. 2017, MNRAS, 467, 2913
- Sheth, R. K. 2003, MNRAS, 345, 1200
- Shi, J., Wang, H., & Mo, H. J. 2015, ApJ, 807, 37
- Shim, J., & Lee, J. 2013, ApJ, 777, 74
- Taylor, J. E., & Babul, A. 2004, MNRAS, 348, 811

Tillson, H., Miller, L., & Devriendt, J. 2011, *MNRAS*, 417, 666

Tormen, G., Diaferio, A., & Syer, D. 1998, *MNRAS*, 299, 728

van den Bosch, F. C., Tormen, G., & Giocoli, C. 2005, *MNRAS*, 359, 1029

Wang, H., Mo, H. J., Jing, Y. P., Yang, X., & Wang, Y. 2011, *MNRAS*, 413, 1973

Winther, H. A., Mota, D. F., & Li, B. 2012, *ApJ*, 756, 166

Wu, H.-Y., Hahn, O., Wechsler, R. H., Behroozi, P. S., & Mao, Y.-Y. 2013, *ApJ*, 767,  
23

Xie, L., & Gao, L. 2015, *MNRAS*, 454, 1697



## Chapter 6

# An Observational Detection of the Bridge Effect of Void Filaments<sup>1</sup>

### 6.1 Introduction

Despite its extreme low-density, a void exhibits a dilute miniature of the cosmic web that interconnects the void galaxies (e.g., Sahni et al. 1994; Gottlöber et al. 2003; Kreckel et al. 2011; Aragon-Calvo & Szalay 2013; Alpaslan et al. 2014). The anisotropic spatial correlation of the tidal shear field is believed to be mainly responsible for the formation of the mini-web in a void just as it is for the cosmic web in the whole universe (van de Weygaert & van Kampen 1993; Bond et al. 1996). As the tidal shear field develops nonlinear correlations during the evolutionary process, the mini-web in a void region should become more and more filamentary.

An intriguing issue is what effect the filamentary mini-web has on the evolution of the void galaxies and how strong it is. This can be addressed by looking for correlations between the intrinsic properties of the void galaxies and the characteristics of the void

---

<sup>1</sup>The content of this Chapter has been already published as the following journal paper: Shim et al. (2015, ApJ, 815, 107) whose copyright is held by American Astronomical Society.

filaments. In fact, the voids should be an optimal ground for the investigation of the effect of the filamentary web on the galaxy evolution (e.g., see Kreckel et al. 2011). First of all, since the void filaments are much less intricate than their wall counterparts, it is less difficult to identify and characterize them. Furthermore, since the densities of the voids are all constrained to extremely low values, the effect of the environmental density on the properties of the void galaxies can be controlled and thus it should be easier to single out the dependence of the galaxy properties on the filamentary web for the case of the void galaxies.

The mini-filaments that pass through a void are expected to bridge the void galaxies with the surrounding denser regions. Hence, the gas and dark matter from the surroundings can be transported into the void regions along the mini-filaments, which would enhance the growth of the void galaxies (Park & Lee 2009b; Kreckel et al. 2011). The recent observation of Beygu et al. (2013) which reported a detection of real-time star-forming activities in the void galaxies embedded in the filamentary channels full of HI cold gases is in line with this picture that the void galaxies can rapidly grow through the filamentary connection with the surroundings.

The bridge effect of void filaments was first noted and quantitatively investigated in the numerical work of Park & Lee (2009b) using the Millennium Run semi-analytic galaxy catalog (Springel et al. 2005). What they found was that the intrinsic properties of the void galaxies such as the total mass, luminosity and blackhole mass are strongly correlated with the degree of the straightness of the host filaments. Park & Lee (2009b) suggested that the presence of this correlation should be attributed to the dependence of the efficacy of gas transportation on the geometrical shapes of the void filaments: the more straight void filaments should more efficiently carry gas and matter onto the void galaxies. Here, our goal is to detect the bridge effect of the void filament from observational data.

The upcoming sections are outlined as follows. In Section 6.2 we describe how the void filaments are identified from the Sloan void catalog and how the degrees of their straightness are measured. In Section 6.3 we report an observational detection of the

correlation signals between the luminosities of the void galaxies and the degrees of the straightness of their host filaments. In Section 6.4 we summarise the results and discuss what clues we can obtain to the formation and evolution of the void galaxies from this observational detection as well as what future works would improve the current analysis. Throughout this paper, we assume a flat  $\Lambda$ CDM universe where the cosmological constant  $\Lambda$  and cold dark matter (CDM) dominate at the present epoch whose initial conditions are described by  $\Omega_m = 0.27$ ,  $\Omega_\Lambda = 0.73$ , ( $h = 0.7$ ,  $\sigma_8 = 0.8$ ), to be consistent with Pan et al. (2012).

## 6.2 Identifying the Mini-Filaments from the Sloan Voids

Since there is no unique way to define both the filaments and the voids, it is first necessary to decide on which algorithm to use for the identification of both. In the current analysis, to be consistent with Park & Lee (2009b), we choose the filament-finding and the void-finding algorithms developed by Colberg (2007) and Hoyle & Vogeley (2002, hereafter HV02), respectively. The former is based on the minimal spanning tree (MST) technique to find the networking pattern (i.e., MST) in the spatial distributions of the point sources and identify the filamentary structures as the most conspicuous cylindrical structures in the interconnected MSTs (Barrow et al. 1985; Colberg 2007).

In the HV02 algorithm, a void is identified as an underdense region containing only field but no wall galaxies. The distance to the fourth nearest galaxy was used as a criterion for the classification of a galaxy: For the wall (field) galaxy,  $d \leq d_{\text{th}}$  ( $d > d_{\text{th}}$ ) where  $d_{\text{th}}$  is a given threshold distance whose value depends on the parent sample of the galaxies (El-Ad & Piran 1997). The boundary of a void is approximated by the continuous surfaces of the superimposed spheres that fit the underdense region (El-Ad & Piran 1997; Hoyle & Vogeley 2002).

Pan et al. (2012) constructed a catalog of the local voids by applying the HV02 algorithm to the seventh Data Release of the Sloan Digital Sky Survey (SDSS DR7) (Abazajian et al. 2009). The void catalog contains a total of 1055 giant voids in the redshift range of  $0 \leq z \leq 0.107$ . It is basically a magnitude-limited sample of the void galaxies for

each of which information on redshift, equatorial coordinates and the  $r$ -band magnitude is all available. The effective radii ( $R_{\text{eff}}$ ) and the numbers of the member galaxies ( $N_g$ ) of the voids were found to be in the ranges of  $9.85 \leq R_{\text{eff}}/(h^{-1}\text{Mpc}) \leq 33.92$  and  $2 \leq N_g \leq 2984$ , respectively (Pan et al. 2012).

As Park & Lee (2009b) did, we exclude those voids which have less than thirty member galaxies from the void catalog of Pan et al. (2012) on the grounds that the filamentary structures are hard to find from those voids. A sample of 831 giant local voids is constructed to which we apply the MST-based filament finding algorithm as follows. For each void in the sample, the member galaxies are regarded as points. The link between a randomly chosen point and its nearest point forms an initial MST, which grows and become updated as the other points in the same void are sequentially added to it in an decreasing order of the separation distances via an iterative search for the nearest points.

A full MST comes out from each void if all of the points become connected. The void filaments are obtained by reducing down a full MST, which requires us to specify two parameters: the pruning level  $p$  and the separation threshold  $d_c$ . After the minor branches consisting of less than  $p$  points are all pruned away, the remaining part of the MST is separated into several mini-filaments by disjoining the galaxies whose separation distances are larger than a given threshold  $d_c$  (Colberg 2007). For the detailed description of the MST-based filament identification procedures applied to the void regions, see Park & Lee (2009a) and Park & Lee (2009b).

As done in Colberg (2007) and Park & Lee (2009b), the best pruning level  $p$  is determined as the value at which the size distribution of the void filaments becomes stabilized in the large size section, where the size  $S$  of a filament is defined as the spatial extent of the three dimensional positions of its member galaxies. The size distribution of the void filaments,  $dN/d \log S$ , is calculated as the number of the void filaments whose sizes  $S$  belong to the differential interval  $[\log S, \log S + d \log S]$  (Park & Lee 2009a).

Varying the pruning level  $p$  from 2 to 7, we repeatedly apply the MST-based filament finder to the 831 giant voids and determine  $dN/d \log S$ . Figure 6.1 plots the size

distributions of the void filaments from our void sample,  $dN/d \log S$ , for six different cases of the pruning level  $p$ . For the case of  $p \leq 4$ , the functional form of  $dN/d \log S$  fluctuates with the change of  $p$  in the large size section ( $S \geq 10 h^{-1} \text{Mpc}$ ). However, note that it becomes stabilized against the change of  $p$  if  $p$  reaches and exceeds 5, which leads us to determine the best pruning level to be  $p = 5$ . It is interesting to recall that in the numerical experiment of Park & Lee (2009b) the size distribution of the void filaments from the Millennium semi-analytic galaxy catalog was shown to become stabilized at the same pruning level  $p = 5$ .

Since the best value of  $p$  depends on the number of the sample galaxies, we investigate how the best value of  $p$  changes if the minimum number of the void galaxies, say  $N_{g,\min}$ , differs from the threshold value of 30 adopted by Park & Lee (2009b). Varying the value of  $N_{g,\min}$  from 20 to 50, we repeat the whole process to evaluate  $dN/d \log S$ , which is shown in Figure 6.2. Although the number density of the void filaments with large sizes ( $S \geq 5 h^{-1} \text{Mpc}$ ) decreases substantially as the value of  $N_{g,\min}$  increases, it is found that the four different cases of  $N_{g,\min}$  yield the same pruning level  $p = 5$ . Furthermore, the correlation strength between the luminosity and the straightness of the void filaments quantified by the Pearson product moment correlation coefficient  $r$  turns out to be robust against the change of  $N_{g,\min}$  (see section 6.3). Throughout this paper, we set  $N_{g,\min}$  at 30 to be consistent with Park & Lee (2009b).

To determine the value of  $d_c$ , Park & Lee (2009b) sought for the value which maximizes the number of the void filaments consisting of four and more member galaxies. They excluded the filaments with less than four member galaxies since those filaments should always have high degree of straightness. Park & Lee (2009b) noted that the number of the void filaments with four and more member galaxies varies strongly with  $d_c$  and reached the highest value when  $d_c$  is equal to  $\bar{d} + \sigma_d$  where  $\bar{d}$  and  $\sigma_d$  are the mean and the standard deviation of the separation distances of the member galaxies belonging to the unpruned MSTs, respectively. Following Park & Lee (2009b), we calculate the values of  $\bar{d}$  and  $\sigma$  from the unpruned MSTs of the void galaxies found in the Sloan void catalog of Pan et al. (2012), we determine the critical separation distance

$d_c$  as  $d + \sigma_d$ .

Among a total of 3172 void filaments found in the redshift range of  $0 \leq z \leq 0.107$  from the Sloan void catalog of Pan et al. (2012), the richest one turns out to have 38 nodes where the node is a jargon of the MST algorithm referring to a member galaxy of a filament (Colberg 2007). Figure 6.3 shows the number of the void filaments  $N_{\text{fil}}$  as a function of the number of their nodes,  $N_{\text{node}}$ , in our sample. For the right-most bin, we plot the accumulated numbers of the void filaments which have 13 or more nodes. As can be seen, the number of the void filaments  $N_{\text{fil}}$  decreases sharply with the number of the nodes  $N_{\text{node}}$ , indicating that the filaments are relatively short in the voids compared with the wall counterparts.

### 6.3 Correlations between the Galaxy Luminosity and the Specific Sizes of Void Filaments

In the original work of Park & Lee (2009b) based on a N-body simulation, the linearity,  $R_L$ , of each filament, defined as the ratio of its end-to-end separation to its total length was used as an indicator of the straightness where the total length of a void filament was defined as the sum of the separation distances between the adjacent nodes (see also Colberg 2007; Park & Lee 2009a). However, in our current work dealing with the void filaments from real observations identified in redshift space, the linearity  $R_L$  may not be a good indicator of the degree of the straightness of a void filament since the total length of a void filament that enters in the definition of  $R_L$  depends sensitively on how accurately the positions of the void galaxies are measured.

The systematic errors associated with the redshift-space measurement of  $R_L$  may severely contaminate the measurement of the correlations between the luminosity of the void galaxies and the degree of the straightness of the hosting void filaments. Therefore, instead of  $R_L$ , we use the specific size of each void filament,  $\tilde{S}$ , defined as the size per node as an indicator of the straightness. The concept of the specific size of a filamentary structure was first introduced by Shim & Lee (2013) who showed that the filamentary

structures having larger specific sizes tend to have more straight shapes (see Figure 6 in Shim & Lee 2013).

For each void filament in our sample, we also determine the mean absolute value,  $|\bar{M}_r|$ , of the absolute  $r$ -band magnitudes of the member galaxies. Since the absolute magnitude  $M_r$  of a galaxy has a negative value and what matters in the current analysis is not the sign but the magnitude of  $M_r$ , we take the absolute value of  $|\bar{M}_r|$  to investigate the correlation with the specific size of the hosting void filament. From there on,  $|\bar{M}_r|$  denotes the mean absolute value of  $M_r$  averaged over the member galaxies of each void filament in the sample.

Figure 6.4 plots how the void filaments in our sample are scattered in the plane spanned by  $|\bar{M}_r|$  and  $\tilde{S}$ , showing an obvious trend that the averaged luminosity of the void galaxies increases with the degree of the straightness of their host filament. Before interpreting this trend as an observational evidence for the bridge effect of the void filaments, it should be critical to examine the possibility that the trend might be just a consequence of the Malmquist bias (Malmquist 1936). Given that the Sloan void catalog of Pan et al. (2012) is a magnitude-limited sample, the high- $z$  void filaments must be biased being composed only of very luminous galaxies. Moreover, as the voids identified via the HV02 algorithm are likely to have larger (effective) radii, the void filaments identified via the MST-based filament-finder in the high- $z$  voids may have on average larger spatial extents. Therefore, it is reasonable to suspect that the Malmquist bias would produce spurious signal of correlation between  $|\bar{M}_r|$  and  $\tilde{S}$ .

To avoid any false signal caused by the Malmquist bias, we consider only the lowest redshift range of  $0 \leq z \leq 0.02$  at which are found a total of 148 void filaments whose relation between  $\tilde{S}$  and  $|\bar{M}_r|$  is shown in Figure 6.5. As can be seen, even at this low redshift bin  $0 \leq z \leq 0.02$ , the absolute mean values,  $|\bar{M}_r|$ , of the void filaments still appear to be correlated with their specific sizes  $\tilde{S}$ . To quantify the correlation between  $|\bar{M}_r|$  and  $\tilde{S}$  of the 148 void filaments, we calculate the Pearson product moment

coefficient,  $r$ , as (Wall & Jenkins 2012):

$$r = \frac{\langle \Delta |\bar{M}_r| \Delta \tilde{S} \rangle}{\left[ \langle (\Delta |\bar{M}_r|)^2 \rangle \langle (\Delta \tilde{S})^2 \rangle \right]^{1/2}}, \quad (6.1)$$

where  $\Delta |\bar{M}_r| \equiv |\bar{M}_r| - \langle |\bar{M}_r| \rangle$  and  $\Delta \tilde{S} \equiv \tilde{S} - \langle \tilde{S} \rangle$ . Here  $\langle |\bar{M}_r| \rangle$  and  $\langle \tilde{S} \rangle$  are the ensemble averages of the mean absolute  $r$ -band magnitudes and the specific sizes over the 148 void filaments, respectively, and  $\langle (\Delta |\bar{M}_r|)^2 \rangle$  and  $\langle (\Delta \tilde{S})^2 \rangle$  are the corresponding rms fluctuations, respectively.

From the 148 void filaments with four or more member galaxies located at  $0 \leq z \leq 0.02$ , we find  $r = 0.37 \pm 0.07$  where the errors associated with the estimate of  $r$  is also calculated as (Wall & Jenkins 2012)

$$\sigma_r = \frac{1 - r^2}{(N_{\text{fil}} - 1)^{1/2}}, \quad (6.2)$$

where  $N_{\text{fil}}$  is the number of the void filaments. To see at what confidence level the null hypothesis of no correlation between  $|\bar{M}_r|$  and  $\tilde{S}$  is rejected, we perform the student- $t$  statistics as (Wall & Jenkins 2012)

$$t = \frac{r(N_{\text{fil}} - 2)^{1/2}}{(1 - r^2)^{1/2}}, \quad (6.3)$$

where  $N_{\text{fil}} - 2$  is the degree of freedom of the  $t$ -variable. Plugging  $r = 0.37$  and  $N_{\text{fil}} = 148$  into Equation (6.3), we find that the null hypothesis is rejected at 99.999% confidence level.

Now that we find an observational evidence for the correlation between  $\tilde{S}$  and  $|\bar{M}_r|$ , we would like to investigate if the strength of correlation depends on the richness of the void filaments (i.e., the number of nodes,  $N_{\text{node}}$ ). Dividing the void filaments at  $0 \leq z \leq 0.02$  into three  $N_{\text{node}}$ -bins, we calculate  $r$  separately by using only those void filaments belonging to each  $N_{\text{node}}$ -bin. Figure 6.6 shows the  $\tilde{S}$ - $|\bar{M}_r|$  scatter plots for three different bins of  $N_{\text{node}}$ . Table 6.1 also lists the mean redshifts, the numbers of the void filaments and the estimated values of the Pearson product moment correlation coefficient  $r$  between  $\tilde{S}$  and  $|\bar{M}_r|$  (the fourth column) for three  $N_{\text{node}}$ -bins. As can be read, the richer filaments exhibit stronger correlations between  $|\bar{M}_r|$  and  $\tilde{S}$ . The value

of  $r$  reaches as high as 0.6 for the richest case of  $11 \leq N_{\text{node}} \leq 27$ . It is also worth noting that the increase of  $r$  with  $N_{\text{node}}$  is not caused by the redshift-difference among the three  $N_{\text{node}}$ -bins.

We have so far followed the frequentist's approach to quantify the correlations between  $|\bar{M}_r|$  and  $\tilde{S}$ . However, the reliability of the frequentist's approach depends on the sample size. Given that the numbers of the low- $z$  void filaments at each  $N_{\text{node}}$ -bin are not large enough to guarantee the success of the frequentist's approach, we also take the Bayesian approach by computing the posterior probability density distribution of the true correlation coefficient,  $\rho$  as (Wall & Jenkins 2012)

$$p(\rho|r, \text{data}) \propto \frac{(1 - \rho^2)^{\frac{N_{\text{fil}}-1}{2}}}{(1 - r\rho)^{N_{\text{fil}}-\frac{3}{2}}} \left[ 1 + \frac{1}{N_{\text{fil}} - \frac{1}{2}} \frac{1 + r\rho}{8} + \dots \right], \quad (6.4)$$

where  $p(\rho|r, \text{data})$  represents the conditional probability of  $\rho$  provided that the Pearson product moment correlation coefficient has the value of  $r$  at each  $N_{\text{node}}$ -bin. Here, we assume a flat prior for  $p(r)$  and normalized  $p(\rho|r, \text{data})$  to satisfy  $\int p(\rho|r, \text{data}) = 1$ . The left, middle and right panels of Figure 6.7 show  $p(\rho|r, \text{data})$ , for the cases of  $4 \leq N_{\text{node}} \leq 6$ ,  $7 \leq N_{\text{node}} \leq 10$  and  $11 \leq N_{\text{node}} \leq 27$ , respectively. As can be seen, the maximum probability is achieved when the true correlation coefficient exceeds 0.6 for the case of the richest filaments, supporting the results obtained from the frequentist's approach.

The observed trend that the correlation between  $|\bar{M}_r|$  and  $\tilde{S}$  becomes stronger with the richness of the void filament can be understood as follows. The richer void filaments correspond to deeper gravitational potential well which can accommodate larger amounts of cold gas, which in turn can be transported even to the central regions of the voids from the surroundings if the void filaments are more spatially extended. In consequence, the mean luminosity of the void galaxies located in the richer filaments would develop more sensitive dependence on the spatial extents of the filamentary networking.

It may be worth examining the dependence of the final result on how to quantify the degree of the straightness of the void filaments. As in the original work of Park

& Lee (2009b), we measure the linearity  $R_L$  of the 148 void filaments and investigate the correlations between  $R_L$  and  $|\bar{M}_r|$  at three  $N_{\text{node}}$ -bins, which are shown in Figure 6.8. The Pearson product moment correlation coefficients between  $R_L$  and  $|\bar{M}_r|$  for the three different  $N_{\text{node}}$ -bin are listed in the fifth column of Table 6.1. As can be seen, no correlation is found between  $R_L$  and  $|\bar{M}_r|$ , which is inconsistent with the result of Park & Lee (2009b) whose numerical analysis found the existence of a strong correlation  $r = 0.67$  between them. To understand where this inconsistency stems from, we examine how strongly  $R_L$  and  $\tilde{S}$  are correlated with each other for the three  $N_{\text{node}}$ -bins, the results of which are shown in Figure 6.9 and listed in the sixth column of Table 6.1. As can be seen, a signal of mild correlation is found for the case of  $7 \leq N_{\text{node}} \leq 11$  but no signal at all for the other two cases.

Note that for the case of  $4 \leq N_{\text{node}} \leq 6$ , the linearity tends to be biased toward high values of  $0.4 \leq R_L \leq 1$ . As explained in Park & Lee (2009b), for the case that the filaments have small number of nodes, the linearity  $R_L$  is prone to high values, failing to represent well the degree of filament straightness. For the case of the rich filaments with large number of nodes, the linearity  $R_L$  is a good indicator of the filament straightness only provided that the positions of the nodes are measured with high accuracy. When the measurements are done in the redshift space, however, the redshift-space errors would contaminate the measurement of each of the positions of the nodes, which would propagate into the errors in the measurements of the total lengths of the filaments. The larger numbers of the nodes a filament has, the larger amount of propagated error would contaminate the measurement of its total length which would in turn cause large uncertainties in the estimate of its linearity.

## 6.4 Summary and Discussion

The aim of this work was to observationally test the scenario suggested by Park & Lee (2009b) that the void galaxies located in the more straight filaments would be more luminous since the efficacy of the gas accretion along the void filaments into the void galaxies increases with the degree of the straightness of the void filaments. The catalog

of the giant galaxy voids constructed by Pan et al. (2012) from the SDSS DR7 datasets with the help of the HV02 void finding algorithm (Hoyle & Vogeley 2002) has been used as the parent sample and the MST-based filament finder was employed to identify the filamentary structures in the galaxy voids.

Determining the specific size (size per node,  $\tilde{S}$ ) of each void filament as a measure of its straightness and the mean absolute value of the absolute  $r$ -band magnitude  $|\bar{M}_r|$  of the member galaxies, we investigated if and how  $|\bar{M}_r|$  is correlated with  $\tilde{S}$  on average by measuring the Pearson product moment correlation coefficient,  $r$ , between the two quantities. To avoid false signals of correlation between  $\tilde{S}$  and  $|\bar{M}_r|$  caused by the Malmquist bias, we have focused only on the lowest redshift for the detection of the bridge effect. From a total of 148 void filaments consisting of four or more member galaxies (nodes) in the redshift range of  $0 \leq z \leq 0.02$ , it is found to be  $r = 0.37 \pm 0.07$ . Although this observational signal is not quantitatively consistent with the numerical estimate,  $r = 0.67$ , by Park & Lee (2009b) based on the Millennium run semi-analytic galaxy catalog (Springel et al. 2005), it is a five sigma signal and thus may be regarded as the observational evidence for the existence of the bridge effect of the void filaments.

We have also inspected if and how the strength of correlation between  $|\bar{M}_r|$  and  $\tilde{S}$  changes with the node number  $N_{\text{node}}$  of the void filaments (i.e., the *richness* of the void filaments) and noted a trend that the value  $r$  gradually increases with the richness of the void filament. Our explanation for this trend is as follows. A richer filament must correspond to a deeper well of the gravitational potential that could accommodate larger amounts of gas inflow from the surroundings. In consequence the void galaxies located in a richer filament would develop more sensitive dependence on the degree of the straightness of void filament.

The straightness of the void filaments reflects how anisotropic the spatial distributions of the void galaxies are. As the voids evolve and their densities decrease, they would become more susceptible to the external tidal forces, which in turn augment the degree of the anisotropy of the spatial distributions of the void galaxies. In other words, the capacity of the void filaments as a transportation channel would increase

in the nonlinear stage of the void evolution where the tidal shear field develop nonlinear correlations. In consequence, the star formation activity in the void galaxies would become stimulated by the efficient supply of the cold gases along the straight void filaments. The presence of the bridge effect of void filaments that has been confirmed by our observational analysis may provide an important clue to the mechanism through which the void galaxies become gas richer, bluer colored, and have higher specific star formation rates than their wall counterparts (e.g., Rojas et al. 2004; Kreckel et al. 2011; Beygu et al. 2013; Ricciardelli et al. 2014).

It should be worth noting here that since only very luminous galaxies can be observed at high redshifts (Malmquist 1936), the void filaments identified at high redshifts via the MST technique would not reflect well enough the degree of the anisotropy tidal shear field. The very luminous galaxies are believed to be embedded in the massive dark matter halos that are strongly biased tracers of the matter density field (e.g., Bardeen et al. 1986). As the very luminous galaxies are expected to have formed at the high peaks of the matter density field whose gravitational collapse proceeds quite isotropically (Bernardeau 1994), the high- $z$  void filaments would fail to capture the unbiased features of the nonlinear matter density field, no matter how straight they are. In other words, to represent the anisotropic nature of the tidal shear field and its effect on the evolution of the filament halos and galaxies in void regions, the filaments must be identified from the unbiased tracers including the dim galaxies (or low-mass halos). This logic can also explain why we have restricted our analysis to the low- $z$  void filaments with  $0 \leq z \leq 0.02$  from a magnitude-limited sample instead of the volume-limited high- $z$  sample, even though the latter is free from the Malmquist bias.

However, we have yet to answer the fundamental question of what caused the bridge effect of void filaments. A more comprehensive study based on cosmological hydrodynamic simulations will be desirable to quantitatively understand why and how the accretion of cold gas occur more efficiently along the straight filaments that emerge during the nonlinear stage of the void evolutions. Also, in the original work of Park & Lee (2009b), not only the mean luminosity but also the mean mass of the central

blackholes of the void galaxies were found to be higher in the more straight void filaments. In fact, it was the mean mass of the central blackholes that yielded the strongest correlation with the degree of the straightness of the void filaments. Although it is very hard to measure directly the masses of the central blackholes, the X-ray luminosities of the void galaxies with active galactic nuclei (AGN), if any, could be used to quantify how massive their central blackholes are. Our future work will focus on searching for the AGN galaxies in the void regions and exploring observationally if and how their AGN activities are correlated with the degree of the straightness of the void filaments.

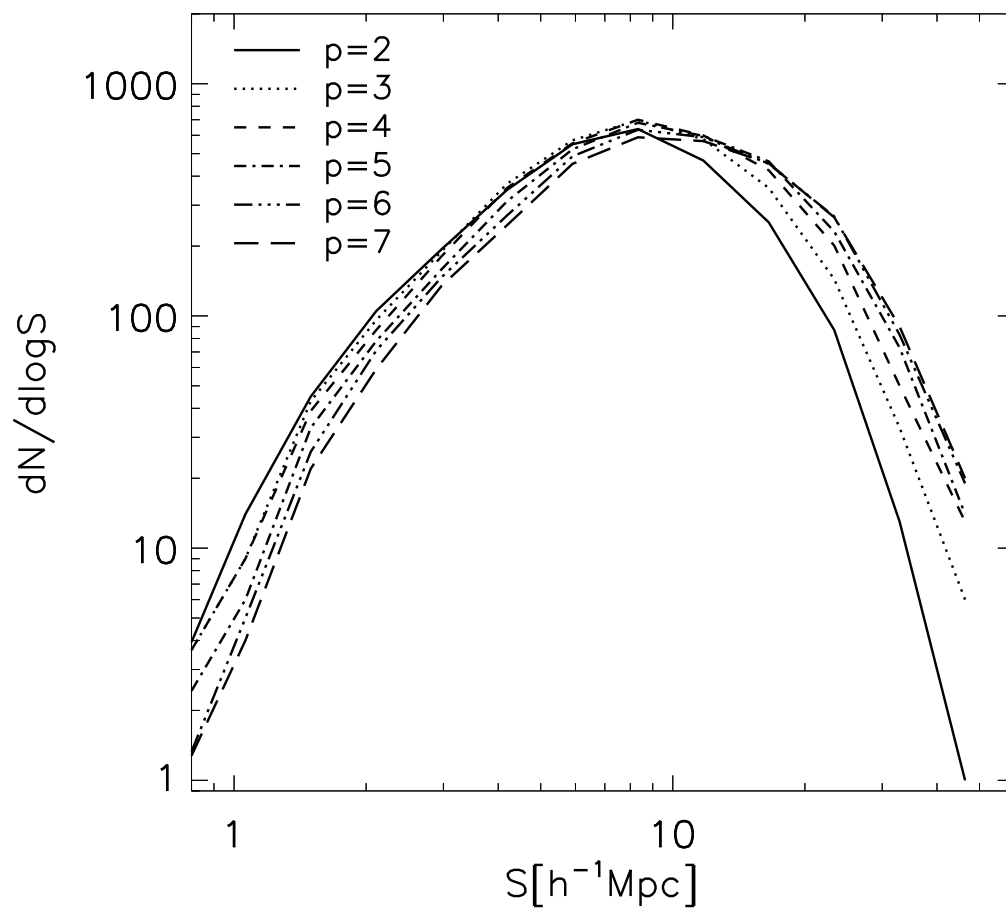


**Figure 6.1.** Size distribution of the void mini-filaments for six different cases of the pruning level  $p$ . Here, a void filament represents the primary structure of a MST from which the minor twigs having less than  $p$  nodes are removed and its size  $S$  is define as its spatial extent. It is clear that the convergence of  $dN/d\log S$  in the large  $S$ -section appears at  $p \geq 5$ .

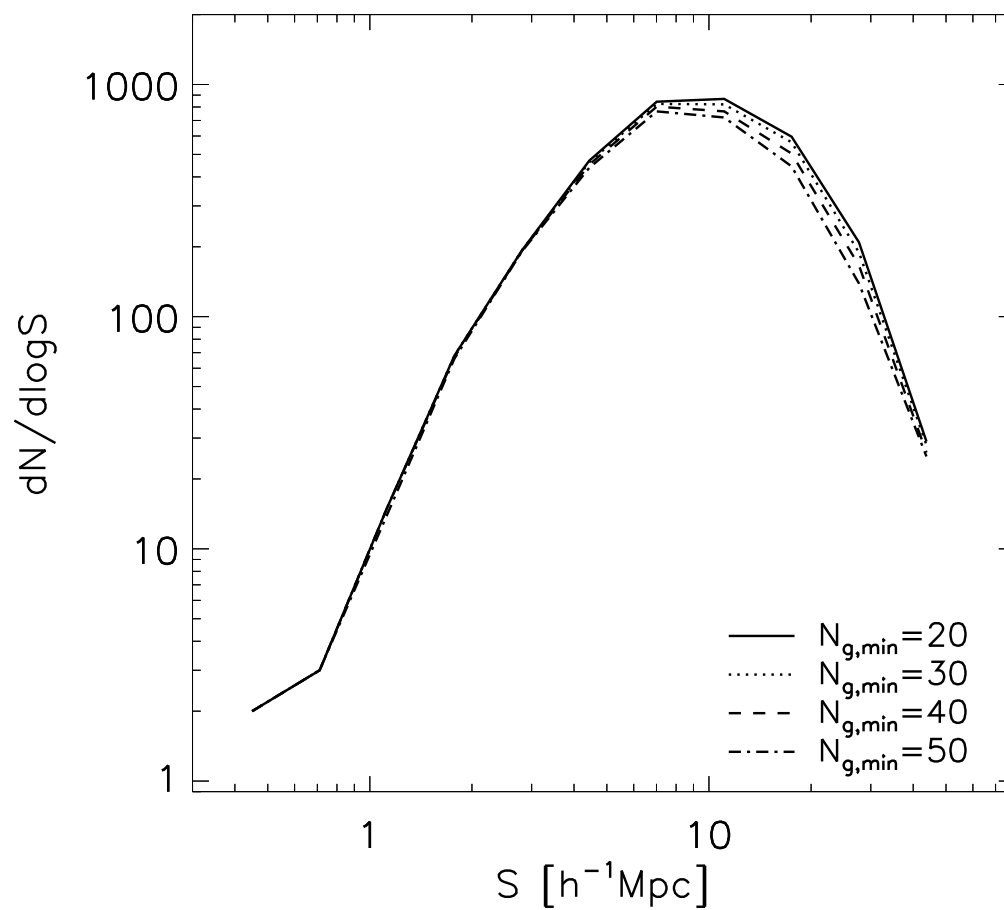


**Figure 6.2.** Number distribution of the sizes of void filaments in interval  $[\log S, \log S + d\log S]$  for four various minimum number of galaxies in a void  $N_{g,\min}$  applied for the giant void selection.

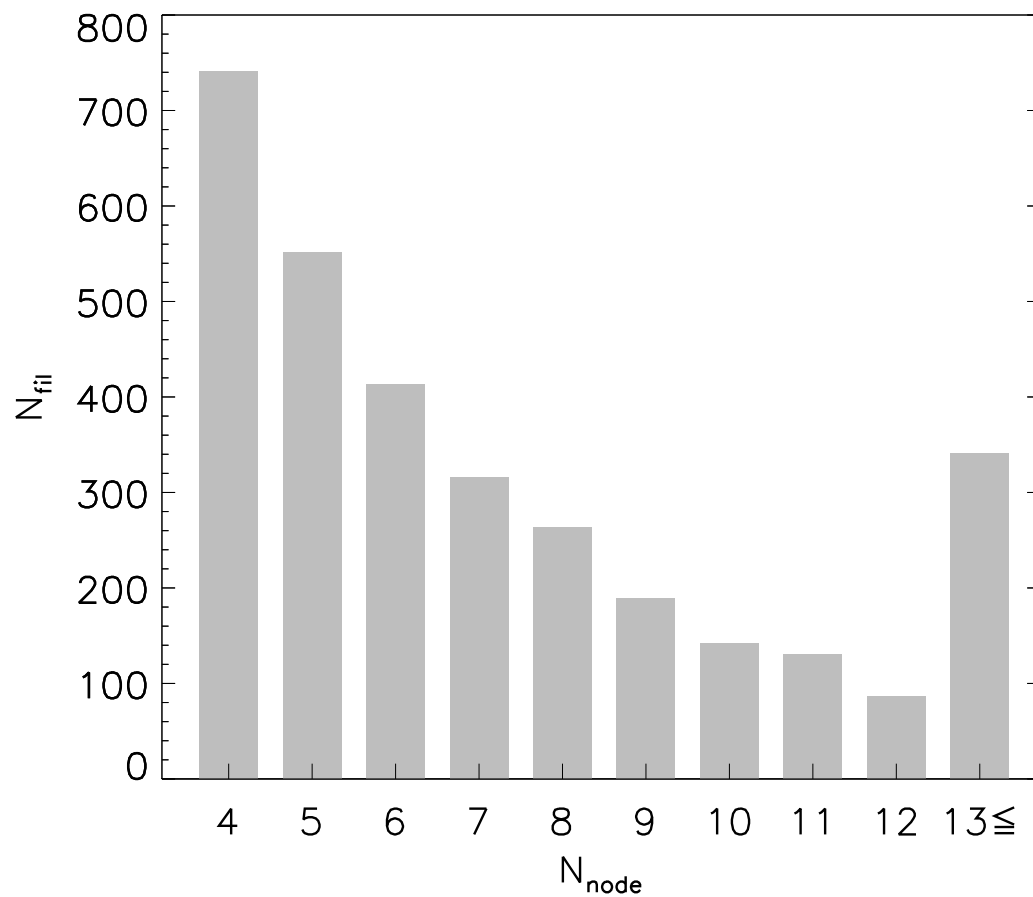


**Figure 6.3.** Number counts of the void filaments having four or more nodes from the Sloan void catalog by Pan et al. (2012) as a function of the node number,  $N_{\text{node}}$ .

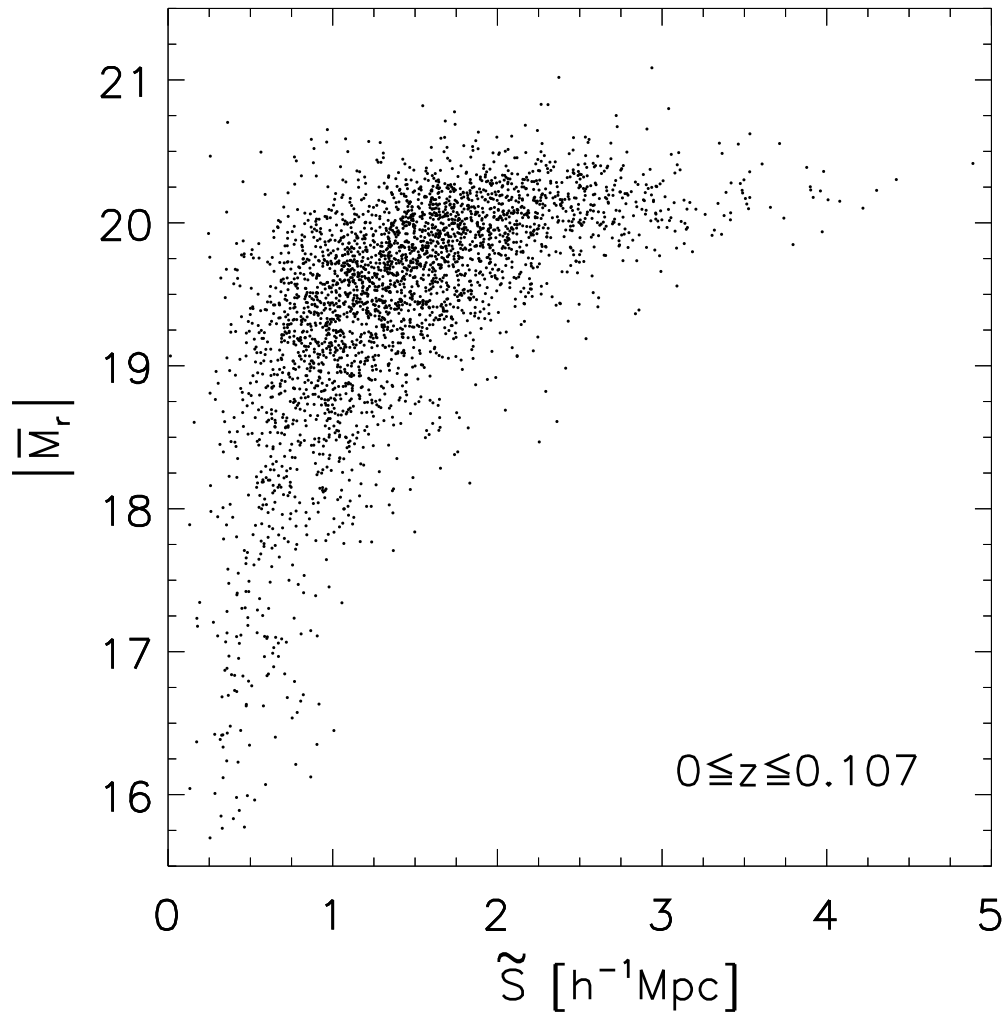


**Figure 6.4.** Specific sizes of the 3172 void filament  $\tilde{S} \equiv S/N_{\text{node}}$  (size per node) versus the mean absolute  $r$ -band magnitude of its member galaxies  $|\bar{M}_r|$  from our sample.

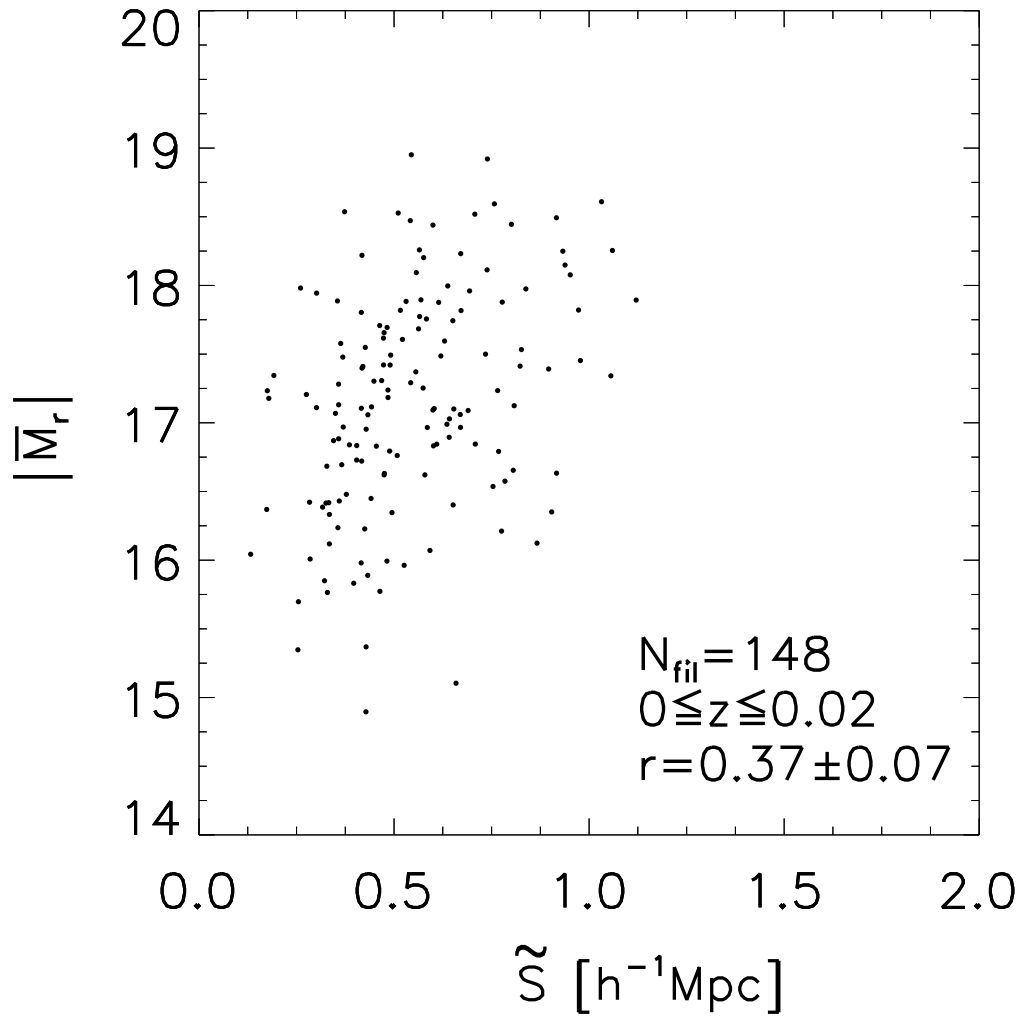


**Figure 6.5.** A total of 148 void filaments with four or more member galaxies at  $0 \leq z \leq 0.02$  from the Sloan void catalog of Pan et al. (2012) in the  $\tilde{S} - |\bar{M}_r|$  plane.

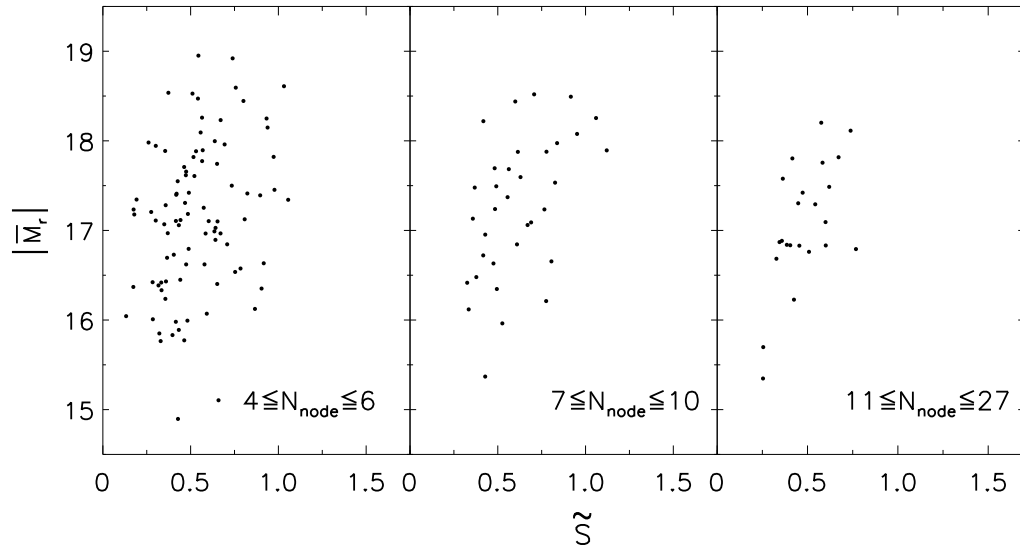


**Figure 6.6.** Same as Figure 6.5 but for three different bins of the number of node  $N_{\text{node}}$ .

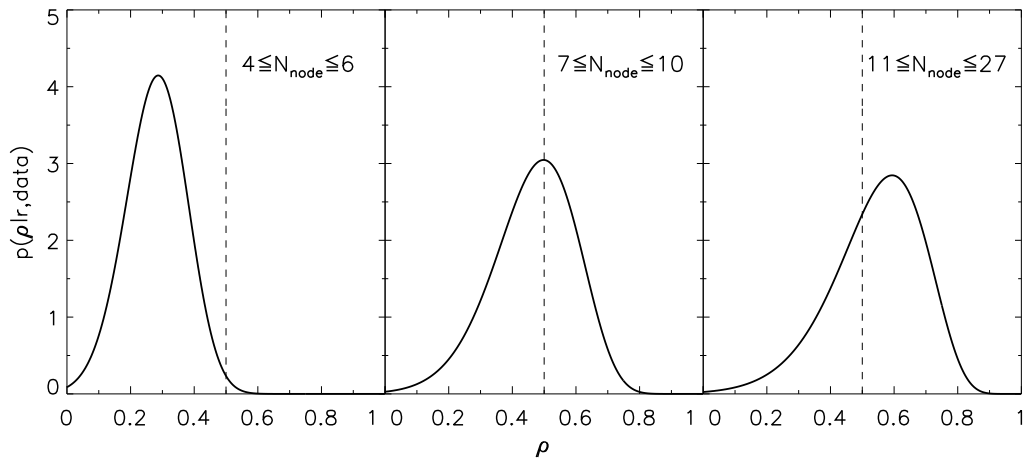


**Figure 6.7.** Posterior probability density distribution of the real correlation coefficient  $\rho$  provided that the Pearson product moment correlation coefficient  $r$  has the resulting value from our sample at  $0 \leq z \leq 0.02$  for three different cases of  $N_{\text{node}}$  (solid line). In each panel the dashed line corresponds to the case of a mild correlation ( $\rho = 0.5$ ).

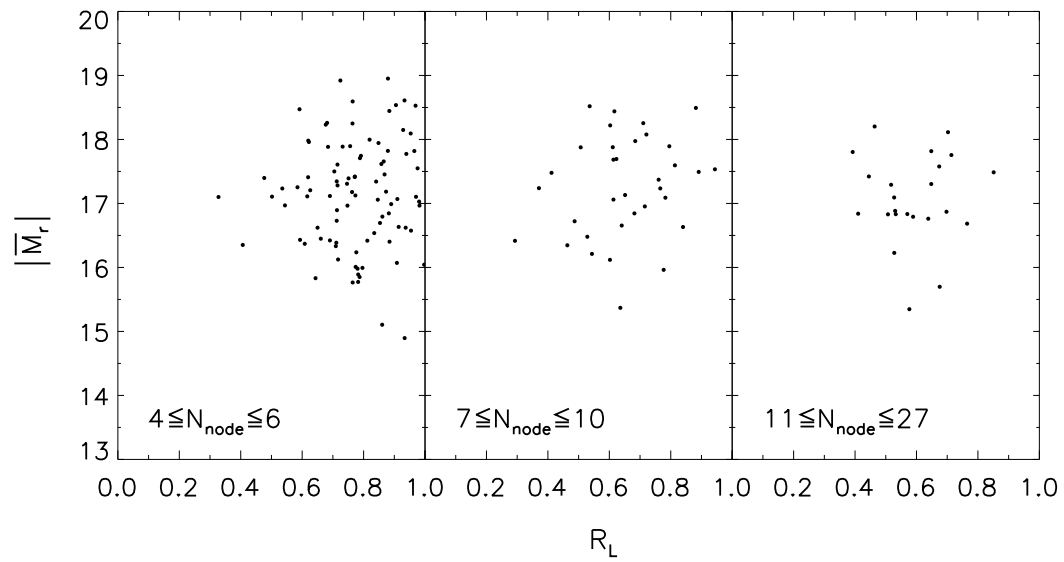


**Figure 6.8.** Same as Figure 6.6 but replacing the specific size  $\tilde{S}$  by the linearity  $R_L$  to represent the degree of the straightness of the void filaments.

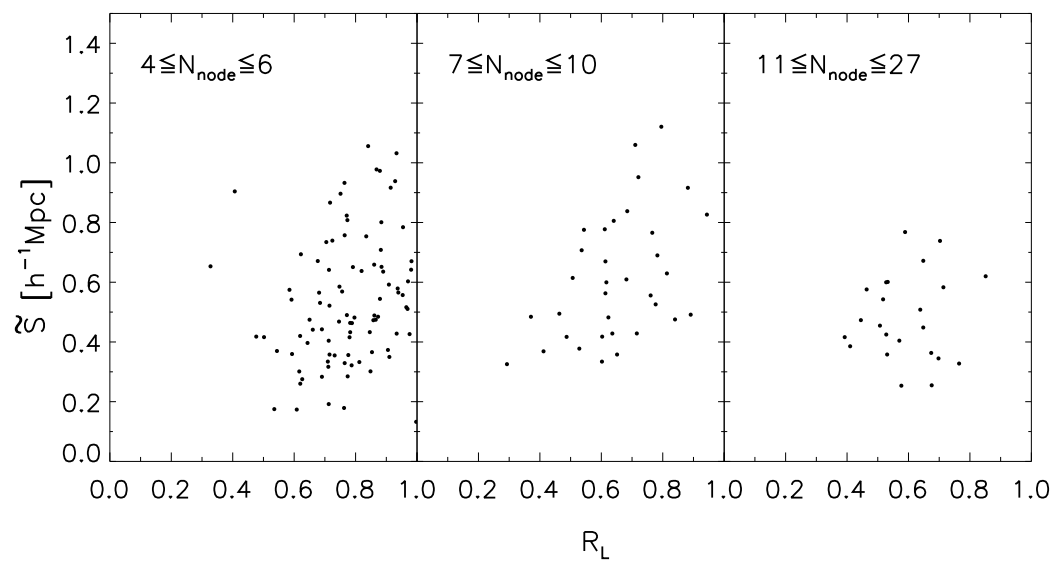


**Figure 6.9.** Specific sizes  $\tilde{S}$  of 148 void filaments versus their linearities  $R_L$ .

Table 6.1. Richness ( $N_{\text{node}}$ ), mean redshift ( $\bar{z}$ ), number of the void filaments ( $N_{\text{fil}}$ ) and Pearson product moment correlation coefficients ( $r$ ).

$N_{\text{node}}$	$\bar{z}$	$N_{\text{fil}}$	$r(\tilde{S},  \bar{M}_r )$	$r(R_L,  \bar{M}_r )$	$r(R_L, \tilde{S})$
[4, 6]	$0.012 \pm 0.005$	91	$0.29 \pm 0.10$	$0.04 \pm 0.10$	$0.21 \pm 0.10$
[7, 10]	$0.014 \pm 0.003$	34	$0.50 \pm 0.13$	$0.21 \pm 0.16$	$0.46 \pm 0.14$
[11, 27]	$0.013 \pm 0.004$	23	$0.60 \pm 0.13$	$0.00 \pm 0.21$	$0.10 \pm 0.21$



# Bibliography

- Abazajian, K. N., Adelman-McCarthy, J. K., Agüeros, M. A., et al. 2009, *ApJS*, 182, 543
- Alpaslan, M., Robotham, A. S. G., Obreschkow, D., et al. 2014, *MNRAS*, 440, L106
- Aragon-Calvo, M. A., & Szalay, A. S. 2013, *MNRAS*, 428, 3409
- Bardeen, J. M., Bond, J. R., Kaiser, N., & Szalay, A. S. 1986, *ApJ*, 304, 15
- Barrow, J. D., Bhavsar, S. P., & Sonoda, D. H. 1985, *MNRAS*, 216, 17
- Bernardeau, F. 1994, *ApJ*, 427, 51
- Beygu, B., Kreckel, K., van de Weygaert, R., van der Hulst, J. M., & van Gorkom, J. H. 2013, *AJ*, 145, 120
- Bond, J. R., Kofman, L., & Pogosyan, D. 1996, *Nature*, 380, 603
- Colberg, J. M. 2007, *MNRAS*, 375, 337
- El-Ad, H., & Piran, T. 1997, *ApJ*, 491, 421
- Gottlöber, S., Lokas, E. L., Klypin, A., & Hoffman, Y. 2003, *MNRAS*, 344, 715
- Hoyle, F., & Vogeley, M. S. 2002, *ApJ*, 566, 641
- Kreckel, K., Platen, E., Aragón-Calvo, M. A., et al. 2011, *AJ*, 141, 4
- Kreckel, K., Croxall, K., Groves, B., van de Weygaert, R., & Pogge, R. W. 2015, *ApJ*, 798, LL15

- Malmquist, K. G. 1936, *Stockholms Observatoriums Annaler*, 12, 7
- Pan, D. C., Vogele, M. S., Hoyle, F., Choi, Y.-Y., & Park, C. 2012, *MNRAS*, 421, 926
- Park, D., & Lee, J. 2009a, *MNRAS*, 397, 2163
- Park, D., & Lee, J. 2009b, *MNRAS*, 400, 1105
- Patiri, S. G., Prada, F., Holtzman, J., Klypin, A., & Betancort-Rijo, J. 2006, *MNRAS*, 372, 1710
- Rieder, S., van de Weygaert, R., Cautun, M., Beygu, B., & Portegies Zwart, S. 2013, *MNRAS*, 435, 222
- Ricciardelli, E., Cava, A., Varela, J., & Quilis, V. 2014, *MNRAS*, 445, 4045
- Rojas, R. R., Vogele, M. S., Hoyle, F., & Brinkmann, J. 2004, *ApJ*, 617, 50
- Sahni, V., Sathyaprakash, B. S., & Shandarin, S. F. 1994, *ApJ*, 431, 20
- Shim, J., & Lee, J. 2013, *ApJ*, 777, 74
- Springel, V., White, S. D. M., Jenkins, A., et al. 2005, *Nature*, 435, 629
- van de Weygaert, R., & van Kampen, E. 1993, *MNRAS*, 263, 481
- van de Weygaert, R., & Bond, J. R. 2008, *A Pan-Chromatic View of Clusters of Galaxies and the Large-Scale Structure*, 740, 335
- Wall, J. V., & Jenkins, C. R. 2012, *Practical Statistics for Astronomers*, (Cambridge, UK: Cambridge University Press)

## Chapter 7

# Concluding Remark

Cosmological applications of filamentary structures in the Universe are presented in this thesis. The applications are divided in two contexts, one for filament as a probe to constrain cosmological models and the other for studying the effects of filament on its constituent halos and galaxies. Summary as well as the physical implications and prospects of both subjects are described in the following.

In the first part, we presented the applications of filament as a complimentary cosmological probe. We identified filaments by applying friend-of-friend (FOF) and minimal spanning tree (MST) to the massive halos ( $M_h \geq 10^{13} M_\odot h^{-1}$ ) of simulations of various cosmological models including the  $\Lambda$ CDM, coupled dark energy (cDE) and  $f(R)$  gravity with and without massive neutrinos, and compared the straightness of those filaments. In the cDE universe where the dark energy is not inert  $\Lambda$  but a scalar field that interacts with dark matter, the filaments are statistically rounder than those in the  $\Lambda$ CDM models. The filaments with rounder configuration in the cDE models can be understood as a consequence of an additional attractive force, which is induced by the coupling between the scalar field dark energy and dark matter, acting on bending the filaments. The redshift evolution of filament straightness showed that more statistically significant discrimination between the  $\Lambda$ CDM and cDE is possible at higher redshift.

Similar results are also found in the  $f(R)$  gravity model which substitutes Ricci scalar  $R$  to function of  $R$  to change gravitational law at cosmological scale. The filaments

in the  $f(R)$  gravity models are rounder than those in the  $\Lambda$ CDM universe due to an additional attractive force generated in  $f(R)$  gravity models which contributes to bending the filaments. The straightness difference between the  $\Lambda$ CDM and  $f(R)$  model becomes smaller at higher redshift in contrary to the case of the cDE and  $\Lambda$ CDM, which means  $f(R)$  gravity can be distinguished not only from the concordance cosmology but also from the cDE models. We also found that the massive neutrinos counter act to the effect of  $f(R)$  gravity on filament straightness by studying filaments in  $f(R)$  gravity universe with massive neutrinos. As the total neutrino mass increases, the strength of the effect of the massive neutrinos straightening the filaments becomes stronger. Although at certain mass, the effect of  $f(R)$  gravity and that of massive neutrino on filament straightness cancel out, it is possible to distinguish  $\Lambda$ CDM from  $f(R)$  gravity with massive neutrinos with redshift evolution of filament straightness.

Finally, we conducted a feasibility study by applying the previous approach to galaxy distributions of observation and simulation to test if the  $\Lambda$ CDM is consistent with the observed Universe in terms of filament straightness. It is shown that the observed distribution of filament straightness falls in the range spanned by those of mock distributions of simulation. It will be more valuable to detect deviation from the  $\Lambda$ CDM (if any) with galaxy surveys covering higher redshifts, since the deviation in higher redshift will provide additional constraints on the underlying cosmological model.

In the second part, we studied the effect of filaments on the galaxy (halo) formation and evolution. First, we examined the substructure abundance of cluster halos as a function of host filament straightness by analyzing the halos of cosmological simulation. Large-scale filaments are identified by applying the FOF and MST to cluster halos ( $M_h \geq 10^{14} M_\odot h^{-1}$ ). It is found that the clusters in straighter filaments tend to have fewer substructures and vice versa. This negative correlation persists, even if the number of member clusters of the filaments is fixed, or the formation redshift of clusters is constrained to a narrow range. To explain the phenomena, we claimed that subhalo infalling and matter accretion in straighter filaments are more severely obstructed by

the development of stronger flows perpendicular to the filaments. The results open a possibility that the alignment of minor axis of the tidal field generated by cluster halos also non-negligibly controls the substructure abundance in clusters.

We also represented an observational detection of the correlation between the luminosity of galaxies and straightness of their host filaments in voids. By identifying void filaments from galaxies in voids, we found that the mean luminosity of void galaxies is brighter in straighter void filaments. Furthermore, the strength of the correlation becomes stronger as the number of member galaxies in void filament increases. These correlations imply that straighter void filament transports matter and gas more efficiently and that the void filament with more galaxies develops deeper potential well resulting in tighter correlation. The correlation found between the galaxy luminosity and filament straightness is an observational evidence that supports the bridge effect of void filaments which states that void filaments transport matter and gas from outside into void galaxies. This observational findings can provide a hint to void galaxies being bluer, gas-richer, and showing more active star formation activities than wall counterparts.

Throughout the thesis, we showed that filamentary structures of the universe are particularly important in the context of cosmology and galaxy (halo) formation and evolution. Since the characteristics of filaments depend on the underlying cosmology, we suggested the straightness of filaments as a complimentary cosmological test. We also studied the roles of filaments in galaxy (halo) formation and evolution and demonstrated that filaments influence on their galaxies (halos) by controlling infall and accretion onto galaxies (halos). Upcoming large galaxy redshift surveys including Euclid, eBOSS, and DESI will observe much larger number of galaxies even at higher redshifts. These will reduce statistical uncertainties in measurement of filament straightness and provide an observational constraints on the redshift evolution of filament straightness. At the same time, it is possible to study the evolution of galaxies in filaments which will elaborate on the process of filaments affecting galaxies. On the other hand, cosmological simulations with higher resolutions and improved prescriptions of detailed physics will provide

better predictions to be compared with observation for the cosmological studies dealt in this thesis. Thus, the cosmological application of filamentary structures will become more important and interesting subject in near future.

## 요 약

필라멘트 구조의 형성과 진화는 암흑 물질, 암흑 에너지, 중력의 작용을 모두 수반한다. 또한 필라멘트는 가스, 물질, 작은 헤일로들을 운반하는 통로로써 은하(헤일로) 형성에 중요한 환경이다. 이러한 사실을 바탕으로 본 학위 논문은 두 갈래의 필라멘트 연구를 제시하였다. 첫째는 필라멘트를 우주론 모형을 제한하는 검증수단으로써 사용하는 것이고, 둘째는 필라멘트가 은하(헤일로) 형성에 미치는 영향을 조사하는 것이다. 첫 파트에서는 필라멘트의 모양이 우주론에 따라 어떻게 변하는지를 다루었다. 이를 위해  $\Lambda$ CDM, 암흑 에너지, 수정 중력 이론 등의 다양한 우주론을 가정하여 수행된 구조 형성 시뮬레이션 결과인 암흑 물질 헤일로의 분포로부터 거대 필라멘트 구조를 찾았다. 그 결과  $\Lambda$ CDM 우주의 필라멘트가 다른 우주에서보다 더 곧은 것을 발견하였다. 또한 곧은 정도가 진화하는 양상을 통해  $\Lambda$ CDM과 대안 모형들을 구별할 수 있다는 것을 확인하였다. 본 연구에서는 필라멘트의 곧은 정도가 우주론에 의존하는 것을 확인함으로써 필라멘트의 곧은 정도를 보완적인 우주론 검증 수단으로 제안하였다. 두 번째 파트에서는 필라멘트가 은하(헤일로)의 형성과 진화에 미치는 영향을 조사하였다. 그 중 첫 번째로는 필라멘트의 곧은 정도와 은하단의 하위 구조물 수의 관계를 연구하였다. 그 결과 더 곧은 필라멘트에 위치한 은하단이 더 적은 수의 하위 구조물을 가지는 것을 확인하였다. 이 결과는 헤일로의 질량, 형성 시기와 필라멘트를 구성하는 헤일로의 수를 고정해도 유사한 경향성을 보였다. 두 번째 연구에서는 우주 공동 안에 존재하는 필라멘트의 곧은 정도와 은하의 밝기의 상관관계를 다루었다. 그 결과 더 곧은 공동 필라멘트의 은하들이 더 밝은 것을 확인하였다. 상기의 발견들을 바탕으로 본 연구에서는 필라멘트가 헤일로와 은하로의 질량 강착과 하위 구조물 유입을 조절함으로써 은하(헤일로) 형성과 진화에 영향을 미치는 것을 확인하였다. 본 학위 논문에는 상기의 결과들이 시사하는 우주론적 의미와 물리적인 해석을 다루었다.

**주요어:** 우주론: 이론 – 우주 거대구조

**학 번:** 2011-23285

# Acknowledgement

Foremost, I would like to express my sincere gratitude to my advisor Prof. Jounghun Lee for the continuous support of my Ph.D. study and research, for her patience, motivation, enthusiasm, and immense knowledge. Her guidance helped me in all the time of research and writing of this thesis.

Besides my advisor, I would like to thank the rest of my thesis committee: Prof. Myung Gyoon Lee, Prof. Myungshin Im, Prof. Sascha Trippe, and Prof. Ho Seong Hwang for their encouragement, insightful comments, and hard questions.

My sincere thanks also go to Prof. Marco Baldi, Dr. Baojiu Li, and Prof. Fiona Hoyle, for permission to include our publications in this thesis and for providing me valuable data. Without the CoDECS data by Prof. Marco Baldi, simulation data with ECOSMOG by Dr. Baojiu Li, and SDSS void catalog by Prof. Fiona Hoyle, this thesis would not have been materialized. Also, I acknowledge the public simulation database CosmoSim for the analysis in the thesis.

I received support from the National Junior Research Fellowship (2014H1A8A1022479) and Basic Science Research Program (No. 2013004372) through the National Research Foundation of Korea (NRF) funded by the Ministry of Education and partially from the research grant from the NRF to the Center for Galaxy Evolution Research (No. 2010-0027910).

Last but not the least, I would like to thank my family who sincerely supported me spiritually and physically throughout my life.